7-25-2016 12:00 AM

Digging Deeper with Diffuse Correlation Spectroscopy

Kyle J. Verdecchia
The University of Western Ontario

Supervisor
Dr. Keith St. Lawrence
The University of Western Ontario

Graduate Program in Medical Biophysics
A thesis submitted in partial fulfillment of the requirements for the degree in Doctor of Philosophy

Abstract

Patients with neurological diseases are vulnerable to cerebral ischemia, which can lead to brain injury. In the intensive care unit (ICU), neuromonitoring techniques that can detect flow reductions would enable timely administration of therapies aimed at restoring adequate cerebral perfusion, thereby avoiding damage to the brain. However, suitable bedside neuromonitoring methods sensitive to changes of blood flow and/or oxygen metabolism have yet to be established.

Near-infrared spectroscopy (NIRS) is a promising technique capable of non-invasively monitoring flow and oxygenation. Specifically, diffuse correlation spectroscopy (DCS) and time-resolved (TR) NIRS can be used to monitor blood flow and tissue oxygenation, respectively, and combined to measuring oxidative metabolism. The work presented in this thesis focused on advancing a DCS/TR-NIRS hybrid system for acquiring these physiological measurements at the bedside.

The application of NIRS for neuromonitoring is favourable in the neonatal ICU since the relatively thin scalp and skull of infants has minimal effect on the detected optical signal. Considering this application, the validation of a combined DCS/NIRS method for measuring the cerebral metabolic rate of oxygen ($CMRO_2$) was investigated in Chapter 2. Although perfusion changes measured by DCS have been confirmed by various flow modalities, characterization of photon scattering in the brain is not clearly understood. Chapter 3 presents the first DCS study conducted directly on exposed cortex to confirm that the Brownian motion model is the best flow model for characterizing the DCS signal. Furthermore, a primary limitation of DCS is signal contamination from extracerebral tissues in the adult head, causing CBF to be underestimated. In Chapter 4, a multi-layered model was implemented to separate signal contributions from scalp and brain; derived CBF changes were compared to computed tomography perfusion.

Overall, this thesis advances DCS techniques by (i) quantifying cerebral oxygen metabolism, (ii) confirming the more appropriate flow model for analyzing DCS data and (iii) demonstrating the ability of DCS to measure CBF accurately despite the presence of a thick (1-cm) extracerebral layer. Ultimately, the work completed in this thesis should help

with the development of a hybrid DCS/NIRS system suitable for monitoring cerebral hemodynamics and energy metabolism in critical-ill patients.

Keywords

Near-Infrared Spectroscopy, Diffuse Correlation Spectroscopy, Delayed Cerebral Ischemia, Cerebral Blood Flow, Cerebral Oxidative Metabolism.

Co-Authorship Statement

Except Chapters 1 and 5, all chapters in this thesis are adapted from published articles, or a manuscript recently submitted for publication. Although, the author of this thesis was the primary author of each publication, individual contributions from the collaborative team of scientists, technicians and clinicians to complete the published work will be highlighted.

Chapter 2 has been adapted from the paper entitled "Quantifying the cerebral metabolic rate of oxygen by combining diffuse correlation spectroscopy and time-resolved near-infrared spectroscopy", published in the *Journal of Biomedical Optics* 18(2):27007 (2013) by Kyle Verdecchia, Mamadou Diop, Ting-Yim Lee, Keith St. Lawrence. Keith St. Lawrence assisted with the study design, provided supervision throughout the project, and reviewed and edited the manuscript. Mamadou Diop designed the hybrid optical system, provided technical insight, and reviewed the manuscript. Ting-Yim Lee supplied the nonparametric analytical program, and reviewed the manuscript. Kyle Verdecchia was responsible for designing and conducting the animal experiments, collecting and analyzing the data, and writing the manuscript.

Chapter 3 has been adapted from the paper entitled "Assessment of the best flow model to characterize diffuse correlation spectroscopy data acquired directly on the brain", published in *Biomedical Optics Express* 6(11):4288 (2015) by Kyle Verdecchia, Mamadou Diop, Laura Morrison, Ting-Yim Lee, Keith St. Lawrence. Keith St. Lawrence assisted with the study design, provided supervision throughout the project, and reviewed and edited the manuscript. Mamadou Diop provided technical insight, and reviewed and edited the manuscript. Laura Morrison conducted surgical procedures, maintained the animal during experiments, assisted with computed tomography data acquisition, and reviewed the manuscript. Ting-Yim Lee suggested the protocol for computed tomography data acquisition, provided software for analysis of computed tomography perfusion data, and reviewed the manuscript. Kyle Verdecchia was responsible for constructing and characterizing the hybrid optical system, designing and conducting animal experiments, collecting and analyzing the data, and writing the manuscript.

Chapter 4 has been adapted from the paper entitled "Assessment of a multi-layered diffuse correlation spectroscopy method for monitoring cerebral blood flow in adults", published in *Biomedical Optics Express,* 7(9) (2016) by Kyle Verdecchia, Mamadou Diop, Albert Lee, Laura Morrison, Ting-Yim Lee, Keith St. Lawrence. Keith St. Lawrence assisted with the study design, provided supervision throughout the project, and reviewed and edited the manuscript. Mamadou Diop provided technical insight, and reviewed and edited the manuscript. Albert Lee assisted in design and construction of the multi-layered phantom, aided in data collection for the phantom experiments, and reviewed the manuscript. Laura Morrison conducted surgical procedures, maintained the animal during conducted experiments, assisted with computed tomography data acquisition, and reviewed the manuscript. Ting-Yim Lee suggested the protocol for computed tomography data acquisition, provided software for analysis of computed tomography perfusion data, and reviewed the manuscript. Kyle Verdecchia was responsible for constructing and optimizing the hybrid optical system, designing and conducting animal experiments, collecting and analyzing the data, implementing the multi-layered model, and writing the manuscript.

Dedication

First, this dissertation is dedicated to my late Nonno, Lino Verdecchia, who devoted much of his life towards education. In particular, his encouragement and motivation to continue pursuing higher education was supplmented by financial aid. With the financial aid he provided, I was fortunate to pursue my passion without hesitation, and for this I am greatly appreciative.

To my mother, a cancer survivor, who gives me the inspiration to study Medical Physics, in hopes that one day I may develop a new device or technique to improve detection and/or treatment of diseases, such as cancer. When facing challenges in school/work or in my personal life, the strength and resilience you exhibit daily empower me with fortitude and courage never to give up.

During my personal growth along this post-graduate journey, I was fortunate to meet my best friend, who I currently call my Fiancée and future life-long partner. Thank you for always giving me a shoulder to lean on when times were tough, and being the first person to celebrate milestones and achievements along this course. As a fellow PhD candidate, thank you for being understanding of the late working nights and helping me out any way you can when life got busy. Your tenacity has taught me valuable lessons by helping me appreciate the smaller things in life and not to take anything for granted.

To my family, for teaching me to value honesty, loyalty, and hard work regardless of the task at hand. To Cosmo, who would make me smile instantaneously with his excitement as I walk in the door, regardless how long it may be between visitations. Finally, I would like to thank all of my friends, new and old, for being a constant source of support.

Acknowledgments

Throughout my graduate career at Western University, the work completed in this thesis was achieved with help from many individuals, both past and present. First, I am eternally grateful to Dr. Keith St. Lawrence for his exemplary supervision that allowed me to grow as a scientist. I shall forever be indebted my graduate career to Keith. His mentoring abilities and leadership have made this up-and-down journey (i.e. post-graduate career) quite rewarding and enjoyable. I am especially appreciative of Keith's understanding and respect of my own career aspirations, which required me to take on extra burden albeit sacrificing time dedicated towards research. For this, I am truly grateful.

My co-supervisor, Dr. Mamadou Diop, took me under his wing when I first arrived in the optics laboratory, which provided me with first-hand experience with technical instrumentation and taught me many invaluable research skills, at the expense of his valuable time. Regardless how busy Mamadou was with advancing his own career, his office door was always open for me to ask questions. Thank you for teaching me the true meaning of being a scientist.

My advisory committee Drs. Ting-Yim Lee and Jeff Carson for aiding me with computed tomography data acquisition and analysis, and construction of a portable optical system, respectively. Also, thank you for providing a secondary source of support and encouragement, and by insightful discussions during our meetings that expanded my way of thinking.

The invaluable help from the laboratory technicians, Jennifer Hadway, Laura Morrison, and Lise Desjardins, does not go unnoticed and is vastly acknowledged. Completion of work in this thesis would not be possible without their expertise and assistance in designing protocols and conducting animal experiments. More importantly, I value the friendships we have developed throughout my post-graduate career.

I am thankful for the many laboratory colleagues that I have had the pleasure knowing personally, which made working at the Lawson Health Research Institute cordial. In particular, I appreciate the friendly welcome during my early post-graduate years from

laboratory alumni (Dr. Jonathan Elliott, Mustafa Ridha and Harini Pandithasekera), and cherish the friendships from current workmates (Dr. Udunna Anazodo, Dr. Daniel Milej, Jessica Kishimoto, Androu, Abdalmalak, Tracy Ssali, Ajay Rajaram, Peter McLachlan, and Mahro Khalid). Last but not least, I would like to thank Albert Lee for being an exceptional undergraduate student I had the pleasure to collaborate with on the phantom design.

This acknowledgment section would not be complete without mentioning a few other colleagues at the Lawson Health Research Institute that eased my post-graduate career in their own way. First, I would like to thank Lynn Keenliside, who spent time teaching me how to manufacture components required for construction of the optical system and phantom. Also, I would like to thank Dr. Yves Bureau for his advice on statistical analysis in Chapter 2. Last, but not least, I would like to thank Wendy Hough and Michele Avon for assistance with all administrative matters. To say the least, each one of you has made my post-graduate career less painful; thank you.

Also, I extend my thanks to the Lawson Association of Fellows and Students (LAFS) softball team, both current and alumni members, with many of you I have made great friendships. Whether it was out on the diamond, eating wings, or during one of our non-softball excursions, we have shared many laughs that were a good break from research, which continually rejuvenated my passion for research.

Finally, I could not forget to achknowledge the following financial support: Canadian Institutes of Health Research, Natural Sciences and Engineering Research Council, Heart and Stroke Foundation (Ontario Provincial Office), Canada Foundation for Innovation (CFI), Ontario Graduate Scholarship (OGS), and Queen Elisabeth II Graduate Scholarship in Science and Technology (QEII-GSST) as the work completed in this thesis would not be possible without the support of these funding groups. Thank you.

Table of Contents

List of Tables

List of Figures

List of Appendices

List of Acronyms and Abbreviations

ANOVA	analysis of variance
APD	avalanche photodiode
ASL	arterial spin labelling
β	coherence factor
B_{DM}	Brownian diffusion model
BFI	blood flow index
BFI_B	blood flow index from Brownian diffusion model
BFI_H	blood flow index from hydrodynamic diffusion model
BFI_R	blood flow index from random flow model
BG	blood glucose
CA	cerebral autoregulation
$C_a(t)$	concentration of dye in arterial blood
CBF	cerebral blood flow
CBV	cerebral blood volume
CCAC	Canadian Council of Animal Care
CDE	correlation diffusion equation
cGlu	concentration of blood glucose
CHD	congenital heart defect
$CI_{95\%}$	95 % confidence interval

$CMRO_2$	cerebral metabolic rate of oxygen
CPP	cerebral perfusion pressure
CT	computed tomography
ctHb	total blood hemoglobin concentration
$C_t(t)$	concentration of dye in tissue
CTP	computed tomography perfusion
CVR	cerebral vascular reactivity
CW	continuous-wave
DA	diffusion approximation
D_B	diffusion coefficient in the bottom layer
DCE	dynamic contrast-enhanced
DCS	diffuse correlation spectroscopy
DCI	delayed cerebral ischemia
DDG	dye densitometer
D_T	diffusion coefficient in the top layer
DTOF	distribution of times of flight of photons
DWS	diffusing-wave spectroscopy
F_B	blood flow index in brain tissue
FD	frequency domain
F_{HM}	blood flow index assuming a homogeneous medium

FOV	field-of-view
F_S	blood flow index in scalp tissue
f_v	venous volume fraction
$g_1(\rho,\tau)$	normalized electric field autocorrelation function
$G_1(\rho,\tau)$	unnormalized electric field autocorrelation function
$g_2(\rho,\tau)$	normalized intensity autocorrelation function
GE	General Electric
Hb	deoxyhemoglobin
HbO_2	oxyhemoglobin
H_{DM}	hydrodynamic diffusion model
HM	homogeneous model
HOB	head-of-bed
HR	heart rate
HSD	honest significant difference
ICG	indocyanine green
ICP	intracranial pressure
ICU	intensive care unit
IRF	instrument response function
JV	jugular vein
LDF	laser Doppler flowmetry

LED	light emitting diodes
LPR	lactate/pyruvate ratio
MAP	mean arterial pressure
MCA	middle cerebral artery
ML	multi-layered
MRI	magnetic resonance imaging
MVA	missing value analysis
N/A	not applicable
N.A.	numerical aperture
NIR	near-infrared
NIRS	near-infrared spectroscopy
N_2O	nitrous oxide
OEF	oxygen extraction fraction
ρ	source-detector distance
$paCO_2$	arterial partial pressure of carbon dioxide
paO_2	arterial partial pressure of oxygen
$PbtO_2$	tissue oxygen tension
PC	phase contrast
PDE	photon diffusion equation
PDT	photodynamic therapy

PET	positron emission tomography
PMT	photomultiplier tube
SAH	subarachnoid hemorrhage
SaO_2	oxygen saturation of arterial blood
ScO_2	oxygen saturation of cerebral tissue
SEM	standard error of the mean
SMF	single-mode fiber
SNR	signal-to-noise ratio
SPAD	single photon avalanche photodiode
SPCM	single photon counting module
SS	sum of squares
StO_2	oxygen saturation of tissue
SVC	superior vena cava
SvO_2	oxygen saturation of venous blood
R	correlation coefficient
RBC	red blood cell
R_{FM}	random flow model
ROI	region-of-interest
R(t)	impulse residue function
RTE	radiative transport equation

SBF	scalp blood flow
SDD	source-detector distance
τ	correlation time
τ_c	displacement time constant
TBI	traumatic brain injury
TCD	transcranial Doppler ultrasound
TCSPC	time-correlated single-photon counting
TDF	thermal diffusion flowmetry
tHb	total hemoglobin concentration
TPSF	temporal point spread function
TR	time-resolved
μ_a	absorption coefficient
μ_s	scattering coefficient
μ_s'	reduced scattering coefficient

Chapter 1

1 Introduction

The intention of this introductory chapter is to give a rationale for the experiments that comprise this thesis entitled: "*Digging Deeper with Diffuse Correlation Spectroscopy*". First, the clinical rationale for developing a non-invasive device to monitor cerebral hemodynamics in patients in the intensive care unit (ICU) is presented. A description of current clinical methodologies and their limitations are outlined. This is followed by a description of a promising optical technique that may overcome some of the caveats of current methods. The theoretical basis of this optical technique, known as diffuse correlation spectroscopy (DCS), is provided, and followed by an extensive review of current applications and limitations of this technology.

1.1 Clinical Rationale

1.1.1 Intensive Care Patients

In 1953, during the polio epidemic, hundreds of patients developed respiratory failure, requiring emergency tracheotomies. However, typical hospitals at that time had inadequate resources to accommodate the patient overload. As a result, the first ICU was established to perform tracheotomies quickly, ultimately reducing mortality (Kelly, Fong, C, & D, 2014). Generally, an ICU describes a location where critically ill patients obtain proper care from specialists. Over the past twenty years, the ICU has evolved into multiple sub-specialty treatment centers, such as the neonatal and neurological ICUs, that cater towards a particular disease or complication, with the aims of improving patient outcome and reducing mortality.

Common to both neonatal and neurological ICUs is the concern for maintaining adequate cerebral blood flow (CBF). Preterm infants make-up a large portion of patients in the neonatal ICU and their immature cerebral vasculature makes them susceptible to impaired autoregulation of CBF (Peeples, Mehic, Mourad, & Juul, 2015). Within the neurological ICU, patients who have experienced a neurological emergency, such as a stroke (Aries, Elting, De Keyser, Kremer, & Vroomen, 2010), a subarachnoid

hemorrhage (SAH) (Otite et al., 2014; Washington & Zipfel, 2011), or a traumatic brain injury (TBI) (Bouma & Muizelaar, 1992; White & Venkatesh, 2008), are vulnerable to further complications, including cerebral edema, cerebral vasospasm, and impaired cerebral autoregulation.

1.1.2 Neurological Complications

In patients requiring intensive care due to one of the various neurological emergencies mentioned earlier, further complications often cause elevated intracranial pressure (ICP) and a corresponding decrease in CBF. Therefore, the goal of current interventions that target ICP is ultimately to increase CBF.

A primary concern with ICU patients is cerebral edema, which refers to the accumulation of excessive fluid in the brain. For instance, mortality for patients with large hemispheric strokes who have evidence of cerebral edema is up to 80% (Hacke et al., 1996; Ropper, 1984). Cerebral edema leads to elevated ICP due to volume constraints within the cranium. In turn, elevated ICP can impair CBF by reducing cerebral perfusion pressure (CPP), making patients susceptible to secondary ischemic brain injury. Management techniques to reduce ICP include the administration of hyperosmolar agents, such as mannitol or hypertonic saline, to promote osmotic flow outward from brain parenchyma (Singh & Edwards, 2013). Should a poor response be observed, more aggressive approaches, such as spinal taps and external ventricular drain (EVD) or decompressive craniectomy, are performed to drain excessive fluid or increase the volume capacity of the brain, respectively, both of which reduce ICP in order to restore cerebral perfusion.

Another cause of delayed cerebral ischemia (DCI), which occurs in approximately 60% of SAH patients, is cerebral vasospasm, which is caused by involuntary constriction of arteries in the brain (Weir, Grace, Hansen, & Rothberg, 1978). Between 20-50% of SAH patients develop secondary cerebral ischemia (Schmidt et al., 2008), which may progress into infarcted cerebral tissue. Symptoms of clinical deterioration and newly formed infarcts trigger the use of interventional strategies, such as administrating the

vasodilator nimodipine (Macdonald, 2014); however, about one-third develop infarction due to vasospasm asymptomatically (Schmidt et al., 2008).

The maintenance of CBF over a wide range of systemic blood pressure is described by cerebral autoregulation (CA). During variations in blood pressure (Figure 1-1), normal CBF is maintained (~50 mL/100g/min) by adjustments to cerebrovascular resistance (Steiner & Andrews, 2006). However, impairment to CA occurs in about one-third of patients with TBI (Bouma, Muizelaar, Bandoh, & Marmarou, 1992; Muizelaar, Ward, Marmarou, Newlon, & Wachi, 1989), leaving patients susceptible to CBF fluctuations during spontaneous changes in systemic blood pressure (Robertson et al., 1999), and ultimately, these patients are vulnerable to DCI. Similar therapeutic interventions to those mentioned earlier (i.e. surgical intervention, or administering hyperosmolar and/or vasodilating drugs) are employed to increase CBF.

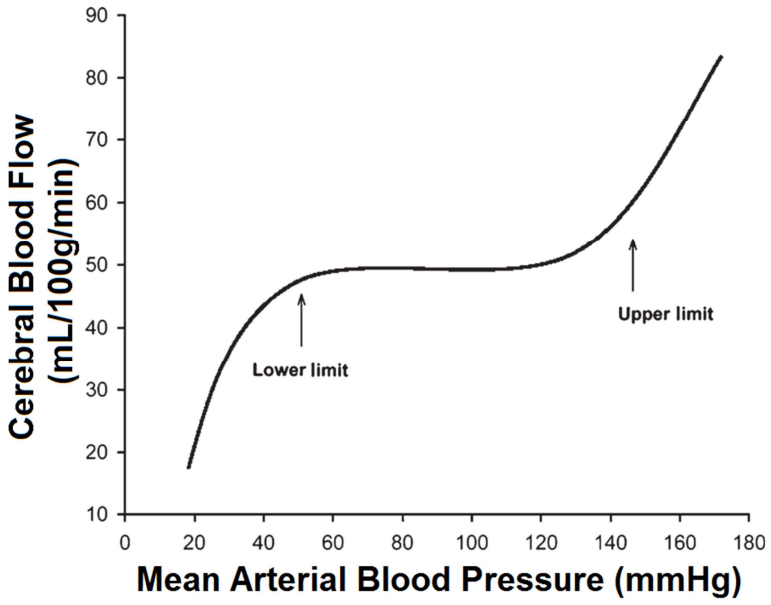

Figure 1-1: Cerebral Autoregulation Plateau; adapted from (White & Venkatesh, 2008)

1.1.3 Clinical Management

Currently, there is no standard method of diagnosing DCI (Sanelli et al., 2014). The best predictor of negative outcome for ICU patients depends on neurological examinations of

their physical characteristics (Alonso et al., 2015; De Oliveira Manoel et al., 2015; English et al., 2013; Kirkman, Citerio, & Smith, 2014), such as level of consciousness as assessed by the Glasgow Coma Scale (Picciolini et al., 2015; Tyson, Parikh, Langer, Green, & Higgins, 2008). Clinical classification scales can help identify patients who are vulnerable to DCI, but they lack specificity and sensitivity (Vergouwen et al., 2010). Patient management would be strengthened by monitoring tools that could detect early, subtle, functional changes, such as impaired CA (De Oliveira Manoel et al., 2015). Furthermore, management of stroke patients has been shown to improve outcome and decrease mortality (Alonso et al., 2015; P. Langhorne et al., 2005) and is especially important during the early-onset of cerebral edema, which peaks a few days after infarction (Shaw, Alvord, & Berry, 1959). However, to diagnose the susceptibility of DCI in patients that are heavily sedated or comatose is not appropriate (Vergouwen et al., 2010). A continuous bedside assessment of the neurological deterioration would improve sensitivity for early detection and prevention of DCI.

In general, an ICU with specialized neurointensivists results in better efficiency and earlier discharge due to improved patient outcome (Bershad, Feen, Hernandez, Suri, & Suarez, 2008; Diringer & Edwards, 2001; Unit & Collaboration, 2013). Providing the specialized neurointensivists with proper tools for monitoring neurological deterioration can further improve patient outcome by aiding in early detection of DCI (Sarrafzadeh, Vajkoczy, Bijlenga, & Schaller, 2014). One approach for detecting DCI is by measuring CPP, which is defined as the difference between the mean arterial pressure (MAP) and ICP. When possible, current clinical management techniques detect low perfusion by monitoring a surrogate physiological parameter of perfusion, ICP, since common neurological complications result from elevated ICP. In adults, ICP is normally between 7-15 mmHg, with pressures greater than 20 mmHg considered neurologically significant (Bratton et al., 2007). This would enable the intensivist team to determine if CBF falls to ischemic levels, which is typically defined as values below 15 mL/100g/min (Symon, Branston, Strong, & Hope, 1977). However, specific pressure thresholds presented in the literature have been inconsistent (Steiner & Andrews, 2006), suggesting that a method of directly measuring CBF would assist in the management of neurological emergencies. Early detection of low blood flow would provide the opportunity to administer

therapeutic treatments to restore CBF in order to prevent secondary brain injury (Coles et al., 2002; Surgeons., 2007).

In addition to monitoring CBF, measuring the cerebral metabolic rate of oxygen ($CMRO_2$) could help identify clinically significant blood flow reductions, i.e. decreases that exceed the compensatory increase in oxygen extraction. This is demonstrated in Figure 1-2, which shows the reduction in $CMRO_2$ that occurs when the increase in the oxygen extraction fraction (OEF) is not sufficient to match the drop in CBF (Dhar et al., 2012; Powers, Grubb, Darriet, & Raichle, 1985; Vespa et al., 2005). For example, in SAH patients, DCI is directly related to poor outcome (Vergouwen, Ilodigwe, & MacDonald, 2011); however, cerebral infarction can occur without any observable symptoms during normal pressure levels (Chen et al., 2011; Schmidt et al., 2008). Insufficient oxygen delivery to brain tissue results in failing ion pumps and deficiencies of energy required for cell survival (Boas & Franceschini, 2011; Powers et al., 1985). However, there is no ideal monitoring device of perfusion/metabolism at the bedside (Le Roux, 2013).

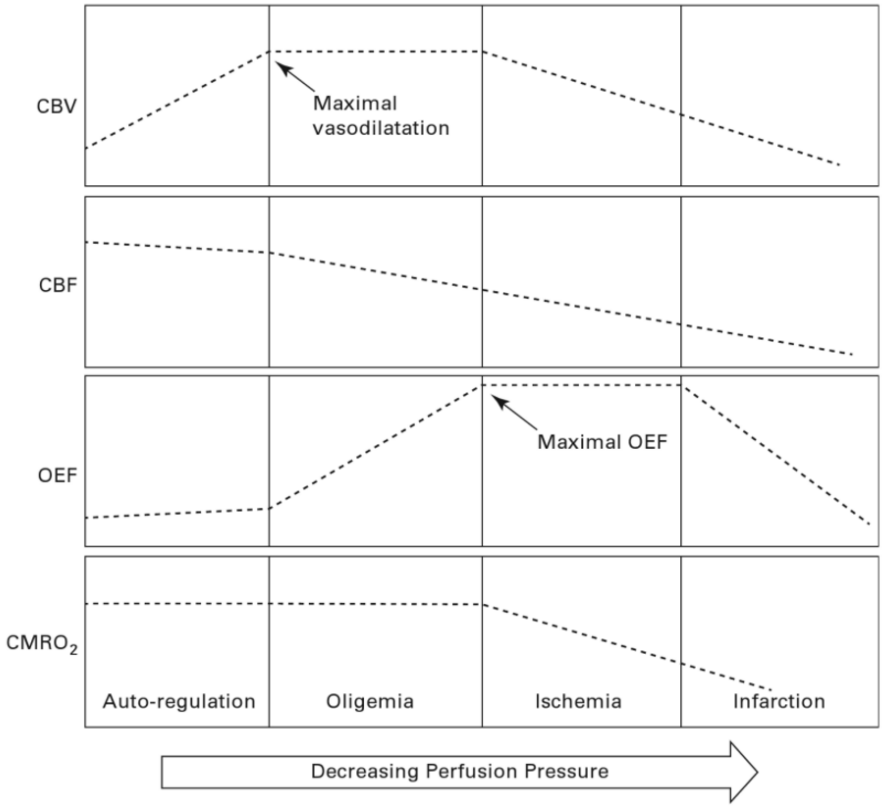

Figure 1-2: Stages of hemodynamic impairment as cerebral tissue perfusion fails; adapted from (Dhar & Diringer, 2016)

1.2 Neuromonitoring Methods

1.2.1 Invasive Techniques

An important aspect of intensive care practice is monitoring ICP, which requires inserting an invasive fiberoptic probe into the brain parenchyma or a catheter into the intraventricular space. Elevated ICP is associated with the incidence of secondary ischemic brain injury as well as worse clinical outcome (Andrews et al., 2002; Juul, Morris, Marshall, & Marshall, 2000). Therefore, increased ICP indicates to a neurointensivist to administer therapeutics designed to improve CBF; however, observational studies question the benefits of monitoring ICP (Cremer et al., 2005; Shafi, Diaz-Arrastia, Madden, & Gentilello, 2008). It could be argued that this is not unexpected since ICP is only a surrogate marker of perfusion and that variations in cerebral vascular resistance could alter the relationship between the two.

Rather than monitoring ICP, cerebral perfusion can be measured by inserting laser Doppler flowmetry (LDF) or thermal diffusion flowmetry (TDF) probes directly into brain parenchyma. The former is a well established technique for real-time flow monitoring; however, it only measures relative flow changes. Although technically challenging, TDF provides quantitative measurements of local cerebral perfusion and has been shown to detect CBF changes associated with vasospasm (Vajkoczy, Horn, Thome, Munch, & Schmiedek, 2003).

In addition to flow monitoring, cerebral microdialysis (CMD) probes provide the capability to measure the biochemistry of tissue (Tisdall & Smith, 2006). In particular, an increase in the lactate/pyruvate ratio (LPR) has proven to be a reliable biomarker of tissue ischemia (Ståhl, Mellergård, Hallström, Ungerstedt, & Nordström, 2001). Also, brain tissue oxygen tension ($PbtO_2$) can be measured by a Clark electrode. In TBI and SAH patients, $PbtO_2$ monitoring has been shown to improve outcome compared to management based on ICP monitoring (Narotam, Morrison, & Nathoo, 2009; Ramakrishna et al., 2008). However, in an ischemic stroke population, approximately half of the patients who were treated for elevated ICP showed changes in the jugular venous oxygen saturation that did not reflect concurrent CBF measurements (i.e. oxygenation remained unchanged when CBF was altered, and vice versa), despite finding reductions of both parameters in non-survivors (Keller, Steiner, Fandino, Schwab, & Hacke, 2002). This suggests that monitoring jugular bulb oximetry alone should be interpreted with caution and highlights the importance of supplementing oxygenation values with a direct measurement of CBF to determine the efficacy of therapeutic treatments.

Despite the ability of each technique to monitor a key physiological parameter at the bedside, all such devices are highly invasive since they require inserting a probe directly into the tissue. Invasive probes/catheters increase the risk of hemorrhage and ventriculitis (Narayan et al., 1982; Pfausler et al., 2004); the latter is susceptible to higher risk from repetitive catheter insertions (Arabi et al., 2005). Furthermore, these invasive techniques are limited to assessing a small tissue volume (~1 mm^3) near the location of the probe. Due to their invasive nature, the use of these methods is typically restricted to

severe brain-injured patients. Nevertheless, the sensitivity of these methods to impaired CBF and energy metabolism highlights the potential value that non-invasive monitoring methods could provide to neuro-intensive care.

1.2.2 Transcranial Doppler Sonography

A non-invasive technique, known as transcranial Doppler (TCD), has proven to be valuable for diagnosing and monitoring cerebral vasospasm (Sekhar, Wechsler, Yonas, Luyckx, & Obrist, 1988), a known precursor to secondary brain injury in SAH patients (Connolly et al., 2012; Staalsø, Edsen, Romner, & Olsen, 2013). Principally, TCD is used to measure flow velocities in the middle cerebral artery (MCA) (Sloan et al., 2004; Washington & Zipfel, 2011), which supplies ~80% of hemispheric blood flow (Moore, David, Chase, Arnold, & Fink, 2006). In the MCA, vasospasms are identified by TCD with a high specificity (94-100%) but moderate sensitivity (38-91%), and its application to other cerebral arteries has proven less accurate (Lee et al., 2006; Washington & Zipfel, 2011). Arterial blood flow velocities are related to perfusion in the macro-vasculature, and therefore, TCD velocity measurements do not reflect micro-vascular perfusion. This suggests a means to directly measure CBF would be beneficial, especially for detecting and monitoring secondary cerebral ischemia, since presence of vasospasms does not solely contribute to cerebral infarction and neurological worsening (Vergouwen et al., 2011).

1.3 Near-Infrared Spectroscopy

The work completed in this dissertation is driven by the current lack of a means of measuring CBF in the clinic that is both non-invasive and direct; one promising technique is near-infrared spectroscopy (NIRS). Because of its low absorption in tissue, electromagnetic radiation within the near-infrared wavelength spectrum (700-1000 nm) can travel farther than visible light. Consequently, this wavelength range is often referred to as an “optical window” (Jöbsis, 1977). The interaction of electromagnetic radiation with tissue is governed by two fundamental interactions: absorption and scattering, which are described in the following sections.

1.3.1 Electromagnetic Radiation

Electromagnetic radiation can be classified as either ionizing or non-ionizing depending on how energy is transferred to the surrounding medium. The former carries sufficient energy per quantum to liberate an electron from an atom or molecule, e.g. x-rays. Near-infrared light is classified as the latter since it does not have sufficient energy to liberate an electron. Instead, energy is transferred non-destructively to an absorbing molecule in tissue by excitation of a vibrational state through a quantum event (i.e. all or nothing). If the frequency of a photon equals the energy required for a molecule to transition to an excited state, then the photon is absorbed, otherwise, a photon is re-emitted (i.e. scattered).

The interactions incurred by a photon as it propagates through a medium is characterized by the scattering (μ_s) and absorption (μ_a) coefficients, which represent the reciprocal of typical distances traveled before a photon is either scattered or absorbed. These interactions may alter one or more of a photon's characteristics: energy, phase, polarization, and direction, as described in the following sections.

1.3.2 Photon Absorption

In the 1700s, the mathematician Pierre Bouguer was the first to arithmetically describe light absorption in a non-scattering medium. He discovered that the intensity of transmitted light (I) is related exponentially to μ_a and the distance between source and detector (ρ) in a homogeneous medium:

$$I = I_0 e^{-\mu_a \rho} \tag{1.3.1}$$

where I_0 represents the source light intensity. In 1852, August Beer observed that light absorption was proportional to the concentration (c_i) of a light-absorbing molecule in the medium, which is referred to as chromophore. In the presence of multiple chromophores, the absorption coefficient can be written as:

$$\mu_a(\lambda) = \ln(10) \sum_i \varepsilon_i(\lambda) c_i \tag{1.3.2}$$

where ε is the wavelength-dependent extinction coefficient of chromophore i. In tissue, the main absorbing chromophores of near-infrared (NIR) light are oxyhemoglobin, deoxyhemoglobin, water, and lipid. The wavelength-dependency of absorption characteristics are illustrated in Figure 1-3.

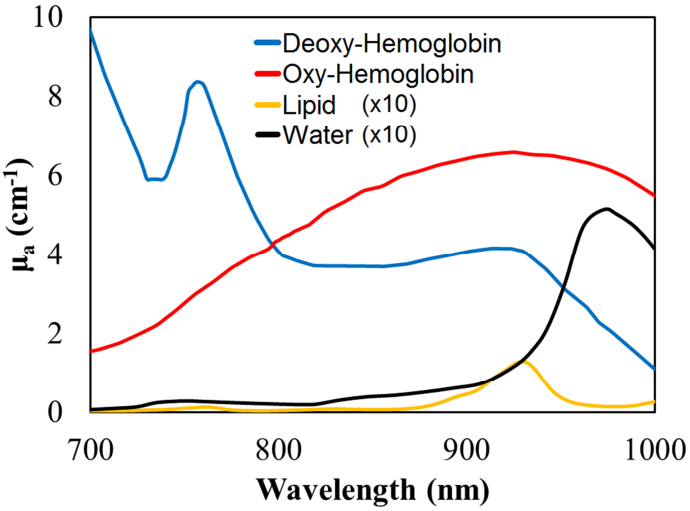

Figure 1-3: Absorption coefficients of the main chromophores in tissue plotted as a function of wavelength; data adapted from Oregon Medical Laser Clinic 2013

Figure 1-3 highlights that the dominant tissue chromophore in the NIR region is hemoglobin. It is important to realize that light absorption in the optical window is relatively weak compared to shorter wavelengths, due to the much greater absorption of hemoglobin, and longer wavelengths due to the increased absorption of water. In principle, the concentration of the main chromophores can be determined by applying Equation 1.3.2 to measured absorption coefficients obtained at different wavelengths. However, the challenge to applying this approach to tissue is the much larger effect of light scattering.

1.3.3 Photon Scattering

Light scattering may be thought of as a direction-altering event experienced by photons. Mie theory models scattering events by assuming that photons interact with particles that can be represented as homogeneous spheres with a refractive index different from the surrounding medium (Hergert & Wriedt, 2012). The result of the interaction is an elastic

scattering event, meaning the kinetic energy of the redirected photon remains the same before and after the interaction.

Photons emitted into a media are directionally oriented, meaning they most likely travel in the forward direction following a scattering event since there is a higher probability for small-angle scattering events to occur due to the orientation of the scattering cross-section. However, forward directionality diminishes with each consecutive scattering event because with each interaction the probability of the scattering angle becomes more homogeneous. In a highly scattering medium, the photon direction quickly becomes isotropic or diffuse (i.e. the direction is random). The average distance traveled by a photon before its path becomes random is given by the inverse of the reduced scattering coefficient (μ_s'):

$$\mu_s' \equiv (1 - g) \cdot \mu_s \tag{1.3.3}$$

where g is the anisotropy factor defined as the average cosine of the scattering angle. It is a measure of the directionality of elastic scattering (i.e. scattering efficiency) and varies between 0 and 1.

Tissue is a highly scattering medium due to the many scattering particles (~10^8), such as cell membranes, nuclei and organelles, and changes in refractive indices within a small volume (1 mm^3). Therefore, the number of photon scattering events greatly outnumbers absorption interactions ($\mu_s' >> \mu_a$). The main three scattering constituents of a NIR photon, listed in order of scattering frequency, are lipoprotein membranes, mitochondria, red blood cells (RBCs), and other cellular components (Cope, 1991). These tissue scattering particles can be categorized into two types: static and dynamic; the difference is the variation in phase of the interacting photon over time. Although scattering events occur more often with static tissue constituents, such as lipoprotein membranes and mitochondria, the phase change is time invariant, and the major contribution to the temporal phase fluctuations of a NIR photon is due to moving RBCs (Bonner & Nossal, 1981; Durduran, Choe, Baker, & Yodh, 2010; Ninck, Untenberger, & Gisler, 2010). The variation in phase due to motion is an important phenomenon that can

be exploited to measure flow using NIR light and is explained in Section 1.5, but first, the mathematical description of light propagation in tissue will be outlined.

1.3.4 Light Propagation in Tissue

Maxwell's equations describe the propagation of electromagnetic radiation in media. In tissue, as the electromagnetic radiation travels long distances many scattering events occur making solutions to Maxwell's equations intractable. Simplifications and assumptions are required to solve light propagation in a highly scattering media. In this section, a brief theoretical derivation of photon diffusion in tissue is presented, highlighting important relationships.

1.3.4.1 Radiative Transfer Equation

Maxwell's equations can be approximated by describing light propagation as a stream of photons. In particular, the complexities of light travel in tissue can be simplified by characterizing individual photon pathlengths with radiative transport theory (Ishimaru, 1989; Profio, 1989). Radiance is defined as the power of light emitted in a direction per unit solid angle [W/cm^2/sr]. As radiance travels within tissue, the radiative transport equation (RTE) mathematically models energy conservation by describing the interactions between particles and radiation:

$$\frac{1}{v}\frac{\partial}{\partial t}L(r,t,\Omega) + \hat{s}\,\nabla\, L(r,t,\Omega) + (\mu_a + \mu_s)L(r,t,\Omega) = \mu_s \int_{4\pi} L(r,t,\Omega)P(\Omega,\Omega')d\Omega' + S(r,t,\Omega) \quad (1.3.4)$$

where L(r,t,Ω) is the radiance in a medium at position r, traveling in direction Ω, at time t. The scattering phase function, P(Ω,Ω′), represents the probability of scattering into a direction Ω′ from direction Ω. The speed of light in the medium is *v*, the source term is S(r,t,Ω), and dΩ′ is the solid angle around Ω.

In an infinitesimal volume, Equation 1.3.4 accounts for energy gains due to the light source and photon scattering into the volume. Also, Equation 1.3.4 accounts for energy losses due to absorption and scattering out of the volume. Although the RTE simplifies Maxwell's equations, it remains complex with no analytical solution. Further approximations are required to solve the RTE.

1.3.4.2 Diffusion Approximation

The diffusion approximation (DA) is the most common solution applied to radiative transfer theory for light propagation in tissue, which is assumed to be a highly diffusive process. Within the DA, a standard method, known as the P_1 approximation, expands all angular dependent quantities (i.e. radiance, phase function, and light source) in a spherical Legendre series truncated at the first moment. To simplify the RTE, the P_1 approximation assumes the following:

- A highly scattering medium (i.e. $\mu_s' >> \mu_a$).
- The scattering phase function, $P(\Omega,\Omega')$, is isotropic.
- For the normalized phase function, the scattering amplitude depends on the change in direction of the photon only.
- The source-detector separation is much larger than the typical distance traveled by a photon before its direction becomes isotropic (i.e. $\rho >> \mu_s'$).
- Slow temporal variations in photon flux (i.e. changes in photon flux occur quicker than a photon traveling in a single transport length).
- Light is unpolarized.

Linearly combining the total power of photons incident on a sphere of cross-sectional area [W/cm^2], the photon fluence rate, $\Phi(r,t)$, is given by:

$$\Phi(r,t) \equiv \int L(r,t,\Omega)d\Omega \tag{1.3.5}$$

and the vector sum of the radiance emerging from an infinitesimal volume [W/cm^2] defined as the photon flux, J(r,t):

$$J(r,t) \equiv \int \Omega \cdot L(r,t,\Omega)d\Omega \tag{1.3.6}$$

Derived in detail elsewhere (L. V. Wang & Wu, 2009), the P_1 approximation gives radiance independent of direction as:

$$L(r,t,\Omega) = \frac{1}{4\pi}\Phi(r,t) + \frac{3}{4\pi}J(r,t)\Omega \tag{1.3.7}$$

Inserting Equation 1.3.5 into the RTE (Equation 1.3.4) and integrating over all solid angles, a relationship that is known as the continuity equation for the fluence rate is obtained:

$$\frac{1}{v}\frac{\partial}{\partial t}\Phi(r,t) + \nabla J(r,t) + \mu_a(r,t)\Phi(r,t) = S(r,t) \tag{1.3.8}$$

Fick's law describes the diffusion of photons in a scattering medium and provides the relationship between fluence rate and flux of a photon by:

$$J(r,t) = -\frac{D(r,t)}{v}\nabla\,\Phi(r,t) \tag{1.3.9}$$

Where the photon diffusion coefficient is defined as:

$$D(r,t) \equiv \frac{v}{3(\mu_s' + \mu_a)} \tag{1.3.10}$$

To describe the radiance of the RTE (Equation 1.3.4) by the photon fluence rate alone, Fick's law (Equation 1.3.9) is substituted into Equation 1.3.8 to obtain the photon diffusion equation (PDE).

1.3.4.3 Photon Diffusion Equation

In a low absorbing, high scattering medium, such as tissue, the photon fluence rate, Φ(r,t), can be described by the PDE:

$$\left(D(r,t)\nabla^2 - v\mu_a(r,t) - \frac{\partial}{\partial t}\right)\Phi(r,t) = -vS(r,t) \tag{1.3.11}$$

In tissue, the path taken by many individual photons that scatter isotropically and travel with a constant velocity between scattering events can be characterized by Equation 1.3.11.

1.4 Quantitative Near-Infrared Spectroscopy Techniques

Accurate modeling of photon propagation through tissue has enabled the development of various NIRS methods for quantifying physiological parameters, such as blood flow and tissue oxygenation, by use of the DA to estimate the absorption and scattering

coefficients (Boas & Yodh, 1997; Maret & Wolf, 1987; D. J. Pine, Weitz, Chaikin, & Herbolzheimer, 1988; A. Yodh & Chance, 1995). One method of categorizing the different NIRS methods is by the type of light source used, which leads to different analytical solutions to the PDE.

1.4.1 Near-Infrared Techniques

Near-infrared spectroscopy techniques typically couple the output of a light source to an optical fiber placed on the surface of a medium in order to deliver photons into the medium. A second optical fiber (or fiber bundle) placed on the same medium will collect photons that have escaped, either by reflection or transmission. These detected photons carry information about the interactions experienced with scattering particles as they travel through the medium. For a thick medium, such as the human head, collecting transmitted photons is not feasible due to light absorption and, therefore, reflection methods are used commonly. Utilizing this general approach, various NIR methods have been developed that are described below.

1.4.1.1 Continuous-Wave NIRS

Continuous-wave (CW), which is the simplest NIR method, uses a steady-state light source. The change in reflected light intensity measured a few centimeters from the source can be characterized by a modified Beer-Lambert Law or the steady-state solution to the PDE (Delpy et al., 1988; Wray, Cope, Delpy, Wyatt, & Reynolds, 1988). CW light sources can be either broadband (i.e. emits over a wide spectral range) or at multiple discrete wavelengths using light emitting diodes (LEDs). Although the equipment is inexpensive, measuring only light intensity at a few wavelengths does not provide sufficient information to separate the effects of absorption and scatter (Siegel, Marota, & Boas, 1999). Consequently, most CW NIRS methods are limited to measuring relative changes in the concentrations of chromophores. Estimations of the photon path length can be derived separately from Monte Carlo simulations or physical models (Delpy et al., 1988), but quantification typically relies on more complex NIRS approaches to directly measure the effects of scattering (Matcher & Cooper, 1994; Matcher, Cope, & Delpy, 1993; Nicklin, Hassan, Wickramasinghe, & Spencer, 2003).

1.4.1.2 Frequency-Domain NIRS

This technique modulates the source intensity at a known frequency and uses detectors capable of detecting the amplitude and phase change of the modulated light (Fantini et al., 1995). Since the phase shift is linearly related to the mean photon pathlength (Arridge, Cope, & Delpy, 1992; Patterson, Chance, & Wilson, 1989), FD NIRS provides a means of quantifying both μ_a and μ_s'. Knowledge of phase enables direct conversion of the detected changes in light attenuation into changes in chromophore concentration. The optical properties can be determined by applying a solution to PDE to the measured phase shift and modulation amplitude in the frequency domain (Delpy et al., 1988; Madsen et al., 1994). Although quantitative information is provided by FD NIRS, it is more technically complex than CW NIRS, requiring a frequency generator to modulate the emission light and a detector that detects both the changes in phase and amplitude of the reflected light.

1.4.1.3 Time-Resolved NIRS

Similar to FD NIRS, another method capable of determining the tissue optical properties is time-resolved (TR) NIRS. With this approach, pulsed light is emitted into a medium and the arrival times of photons, which vary depending on their pathlength, are measured (Delpy et al., 1988; Montcel, Chabrier, & Poulet, 2005; Patterson et al., 1989). Millions of detected photons are binned based on their arrival time to generate a histogram (Figure 1-4), which is referred to as the temporal point spread function (TPSF). The dispersion of the time-of-flight of the detected photons is due to the difference of paths through the medium caused by photon scattering; however, some of the broadening of the TPSF is also a result of temporal dispersion within the instrumentation. Therefore, deconvolution of the measured TPSF and the measured instrument response function (IRF) isolates the true distribution of time-of-flights (DTOF) of the photons in the medium alone (Diop & St. Lawrence, 2012). The tissue optical properties can be determined using an analytical solution to the PDE (Equation 1.3.11) to characterize the DTOF (Patterson et al., 1989). Since late arriving photons have the highest probability of traveling deeper into the medium, TR NIRS provides improved depth sensitivity (Diop & St. Lawrence, 2013;

Kienle, Glanzmann, Wagnières, & Bergh, 1998; Selb, Stott, Franceschini, Sorensen, & Boas, 2005).

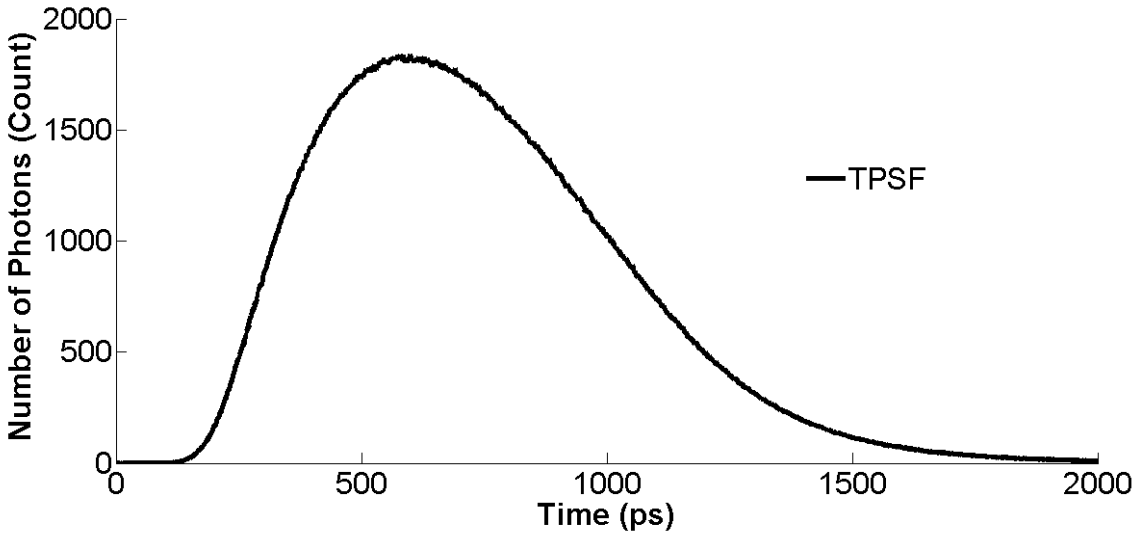

Figure 1-4: Measured dispersion of photon arrival times due light interrogating the optical instrument components and medium (TPSF)

1.4.2 Measuring Tissue Oxygen Saturation by NIRS

As discussed above, the optical properties of tissue can be determined by the combination of different NIRS methods and the PDE (Delpy & Cope, 1997). Since absorption depends on wavelength (Equation 1.3.2), the concentration of deoxy- and oxy- hemoglobin (i.e. [Hb] and [HbO_2], respectively) can be determined by measuring light absorption at two or more wavelengths (Figure 1-3). NIRS provides a means for assessing oxygen metabolism, which is the dominant source of tissue energy. The balance between oxygen supply and metabolic energy demands is reflected by tissue oxygen saturation (StO_2) and is related to hemoglobin concentrations by the definition:

$$StO_2 \equiv \frac{[HbO_2]}{[HbO_2]+[Hb]} \tag{1.4.1}$$

where StO_2 represents the local average blood oxygenation of tissue and is related to the tissue constituents of arterial (SaO_2) and venous (SvO_2) hemoglobin by:

$$StO_2 = a \cdot SaO_2 + b \cdot SvO_2 \quad (1.4.2)$$

where a and b are fractional constants of the arterial and venous saturation in tissue that sum to 1 (Watzman et al., 2000).

Reductions in StO_2 have been shown previously in muscle during occlusion of the forearm and during muscle contractions (De Blasi, Fantini, Franceschini, Ferrari, & Gratton, 1995; Ferrari, Binzoni, & Quaresima, 1997). Also, in the neonatal ICU, expected reductions in StO_2 during apnoea were detected (Brazy, Lewis, Mitnick, & Jobsis, 1985), and asphyxiated newborns that show an increase in cerebral StO_2, relative to healthy controls, correlate with abnormal outcome (Zaramella et al., 2007). Tissue oxygen saturation is an indicator of metabolism in muscle and brain; however, this measurement may be confounded by the delivery of oxygen by blood flow (Boas & Franceschini, 2011). Therefore, oxygen consumption is better assessed by measuring both StO_2 and blood flow.

1.4.3 Measuring Tissue Perfusion by Dynamic Contrast-Enhanced NIRS

NIRS can quantify tissue perfusion by utilizing oxy-hemoglobin as an endogenous flow tracer (Edwards et al., 1988; Elwell et al., 1994) or with the aid of an exogenous contrast agent (Diop et al., 2010; Elliott et al., 2014). The latter provides superior signal-to-noise (SNR) since the absorption change related to perfusion is much greater. Perfusion is quantified by dynamic contrast-enhanced (DCE) NIRS using a tracer kinetic model to relate the concentration of dye in the tissue to the amount being delivered by arterial blood (Brown et al., 2002; Elliott, Diop, Tichauer, Lee, & St. Lawrence, 2010; St. Lawrence et al., 2013):

$$C_t(t) = CBF \cdot \int_0^\infty C_a(t-u) \cdot R(u)\, du \quad (1.4.3)$$

where $C_t(t)$ is the dye concentration in tissue as a function of time (t) measured by NIRS, and $C_a(t)$ is the arterial blood concentration measured by a dye oximeter (Brown et al., 2002). R(t) is defined as the impulse residue function and it represents the fraction of tracer in the tissue at time t following an idealized bolus injection at t = 0 (i.e. the injected

tracer can be represented by a delta function with unit area). The flow-scaled impulse residue function, CBF·R(t), can be extracted by deconvolution, and its initial height equals CBF since by definition R(0) ≡ 1. This method can be used to quantify cerebral perfusion, but it does not provide a means for monitoring CBF since each measurement requires an injection of the contrast agent (Diop et al., 2010).

1.4.4 Cerebral Metabolic Rate of Oxygen

The ability of NIRS to quantify both cerebral oxygenation and CBF makes it possible to assess the $CMRO_2$ (Elwell et al., 2005), which is considered a better indicator of tissue viability than CBF alone (Powers et al., 1985). The $CMRO_2$ is related to CBF by the Fick principle (i.e. conservation of mass):

$$\mathrm{CMRO_2} = \mathrm{CBF} \cdot ([\mathrm{O_2}]_\mathrm{a} - [\mathrm{O_2}]_\mathrm{v}) \tag{1.4.4}$$

where $[O_2]_a$ and $[O_2]_v$ are the oxygen concentration in the incoming arteries and outgoing veins, respectively. The former can be determined by pulse oximetry while the latter can be estimated from StO_2 (Section 1.4.2). Quantification of $CMRO_2$ can be obtained by combining StO_2 with absolute CBF measurements from DCE NIRS (Section 1.4.3) (Tichauer, Brown, Hadway, Lee, & St. Lawrence, 2006; Tichauer, Hadway, Lee, & St. Lawrence, 2006; Tichauer et al., 2010). However, real-time $CMRO_2$ monitoring requires a perfusion technique capable of measuring CBF continuously.

1.5 Diffuse Correlation Spectroscopy

The recent emergence of an optical technique, known as DCS, provides a means of monitoring CBF that does not require the injection of an exogenous contrast agent (Boas, Campbell, & Yodh, 1995; Buckley, Parthasarathy, Grant, Yodh, & Franceschini, 2014). DCS is a variation of another technique, known as dynamic light scattering, which was developed in the 1960s to analyze speckle intensity fluctuations (Cummins & Swinney, 1970; Pecora, 1972). The theory was investigated in dilute "single-scattering" experiments to characterize the size of particles (Berne & Pecora, 1976; Riva, Ross, & Benedek, 1972; Stern, 1975). Shortly after, "single-scattering" experiments evolved into "multiple-scattering" experiments in soft condensed matter by diffusing-wave

spectroscopy (DWS) (Bonner & Nossal, 1981; D. Pine, Weitz, Chaikin, & Herbolzheimer, 1988). Since DCS is an optical technique that uses NIR light, it has the same promising principles as NIRS (i.e. safe, non-invasive, fast temporal resolution, probes deep tissue, and is portable). However, it also provides the ability to monitor the motion of scatterers, which is dominated by the movement of RBCs in tissue. This following section provides the theory of DCS to measure blood flow changes.

1.5.1 Measuring the Intensity Autocorrelation Function

As described in Section 1.3, NIR photons propagating into tissue encounter many scattering interactions, including from dynamic erythrocytes (Figure 1-5A). At the location of a detector on the surface of the interrogated medium, the light electric fields constructively/destructively interfere to produce a speckle intensity (i.e. bright and dark spots). Due to the motion of RBCs, the phase of interacting photons is altered, which in turn, modulate the interference at the detector, causing transient intensity fluctuations (Figure 1-5B). Faster moving RBCs cause the speckle intensity fluctuations to occur more rapidly, inducing earlier decreases in the temporal coherence, which is a measure of the degree of phase correlation (Figure 1-5C).

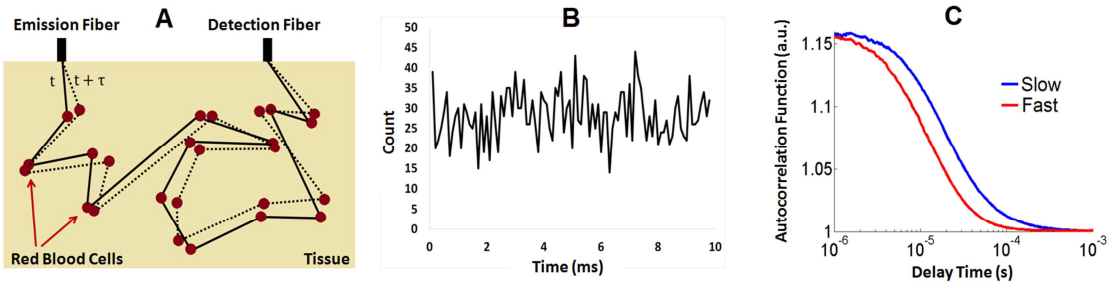

Figure 1-5: Illustration of diffuse correlation spectroscopy; adapted from (Wesley B Baker et al., 2014; Zhou, 2007)

(A) Single photons are emitted into a homogeneous tissue where they propagate and experience multiple scattering events predominantly from moving RBCs. The solid and dotted lines represent the pathlengths of two photons measured at time t and at a later time delayed by τ (i.e. t + τ), respectively. (B) At the detection site, temporal intensity fluctuations are measured. (C) Normalized intensity autocorrelation function is computed by a correlator board; red and blue decay curves represent fast and slow blood flow, respectively.

To assess tissue perfusion, a normalized intensity autocorrelation function is computed from the measured speckle light intensity fluctuations:

$$g_2(\rho,\tau) \equiv \frac{\langle I(\rho,t)I(\rho,t+\tau)\rangle}{\langle I(\rho,t)\rangle^2} \quad (1.5.1)$$

where, τ is the correlation time and $<I(\rho,t)>$ is the light intensity detected at the tissue surface at a distance ρ from the source at time t. Equation 1.5.1 is related to the normalized electric field autocorrelation function, $g_1(\rho,\tau)$, by the Siegert relationship (Lemieux & Durian, 1999):

$$g_2(\rho,\tau) = 1 + \beta|g_1(\rho,\tau)|^2 \quad (1.5.2)$$

where β is the coherence factor of the detection system.

For a high scattering, low-absorbing medium, the electric field autocorrelation function, $g_1(\rho,\tau)$, satisfies the PDE (Section 1.3.4.3) for a continuous light source (Boas et al., 1995; Cheung, Culver, Takahashi, Greenberg, & Yodh, 2001):

$$g_1(\rho,\tau) = \frac{G_1(\rho,\tau)}{\langle I(\rho,\tau)\rangle} = \frac{\langle E(\rho,\tau)\cdot E^*(\rho,t+\tau)\rangle}{\langle |E(\rho,t)|^2\rangle} \quad (1.5.3)$$

where the unnormalized electric field autocorrelation function, $G_1(\rho,\tau)$, can be modeled by the correlation diffusion equation (CDE) (Boas et al., 1995; Skipetrov & Maynard, 1996).

1.5.2 Correlation Diffusion Equation

In 1990's, an equivalency between correlation transport and photon transport was introduced, which treats the transport of correlation through turbid medium similar to radiative transport theory (Ackerson, Dougherty, Reguigui, & Nobbmann, 1992). The difference between radiative and correlation transport is that the former maintains energy conservation whereas the latter accumulates correlation decay from each scattering event with dynamic particles resulting in a loss of coherence. This difference is described theoretically by scattering. Radiative transport assumes energy is conserved as a photon scatters in and out of an infinitesimal volume, whereas correlation transport similarly describes a transfer of correlation, except that a photon scattering into the infinitesimal volume has accumulated a loss of coherence (i.e. correlation decay). By mathematically applying this difference between radiative and correlation transport theory to Equation

1.3.4, similarly for a high scattering, low-absorbing medium, the PDE (Equation 1.3.11) can be modeled by the CDE (Boas et al., 1995; Skipetrov & Maynard, 1996):

$$\left(\mathrm{D}(\mathrm{r},\mathrm{t})\nabla^2 - v\mu_\mathrm{a}(\mathrm{r},\mathrm{t}) - \mu_\mathrm{D}^2(\tau)\right)\mathrm{G}_1(\mathrm{r},\tau) = -v\mathrm{S}(\mathrm{r},\tau) \tag{1.5.4}$$

where μ_D accounts for the loss of correlation due to dynamical processes (i.e. the motion of scatterers) and is given by:

$$\mu_\mathrm{D}^2(\tau) = \frac{3\nu}{\mathrm{D}}\left(\mu_\mathrm{a} + \alpha\mu_\mathrm{s}^{'}\mathrm{k}_0^2\langle\mathrm{r}(\tau)\rangle\right) \tag{1.5.5}$$

where, $k_0 = 2\pi n/\lambda$ is the wavenumber of light (λ is wavelength and n is the refractive index), α is the proportion of moving scatters, which is predominantly RBCs in tissue (Bonner & Nossal, 1981; Ninck et al., 2010), to all scatterers and is related to the blood volume, and $<\Delta r^2(\tau)>$ is the mean-square displacement of the moving scatterers during a correlation time τ.

To relate $g_2(\rho,\tau)$ to blood flow, the CDE is solved by an appropriate analytical model that characterizes the motion of RBCs and the interrogated geometry. This can be challenging as the motion of RBCs is not well understood and the geometry, such as the adult head, can be complex due to tissue heterogeneities.

In tissue, the loss of coherence is predominately affected by the movement of erythrocytes in the microvasculature (Ninck et al., 2010). Originally, a photon is thought to have sequentially scattered off of moving RBCs within different vessels due to the torturous nature of microvasculature. Therefore, the direction of moving RBCs relative to the multiply-scattered photon is assumed to be random (i.e. $<\Delta r^2(\tau)> = V^2\tau^2$, where V is the velocity of the moving scatterers). However, autocorrelation functions are best fit by assuming the motion of dynamic scatterers as Brownian diffusion (i.e. $<\Delta r^2(\tau)> = 6D_B\tau$, where D_B is the effective diffusion coefficient). The loss of coherence of the photon may be best explained by within-vessel scattering due to tissue shearing, tumbling, and rolling experienced by an erythrocyte as it moves within a vessel; however, characterizing the motion of dynamic scatterers requires further investigation. The Brownian diffusion flow model has been successfully applied to a wide range of tissue types to fit for the αD_B term (Durduran, Choe, et al., 2010), which is commonly refferred to as a blood flow index

(BFI) in tissue. Most applications of DCS, such as the head of neonatal infants, assume a semi-infinite homogeneous medium, which is acceptable if the thickness of the extracerebral layers is relatively thin (Buckley et al., 2014; Durduran & Yodh, 2014).

1.5.3 Analytical Solution for a Homogeneous Medium

Currently, the most common analytical solution applied to analyze DCS data assumes light propagates in a semi-infinite (i.e. no light transmission) homogeneous medium. The solution for $G_1(\rho,\tau)$ is given by:

$$G_1(\rho,\tau) = \frac{3\mu_s'}{4\pi}\left[\frac{\exp(-\mu_D r_1)}{r_1} - \frac{\exp(-\mu_D r_1)}{r_2}\right] \quad (1.5.6)$$

where, $r_1 = [\rho^2 + z_0^2]^{1/2}$ and $r_2 = [\rho^2 + (z_0 + 2z_b)^2]^{1/2}$. z_0 is the effective depth of the source and is defined as $1/\mu_s'$, z_b is the extrapolated boundary and is defined as $2D(1+R_{eff})(1-R_{eff})^{-1}$ (Kienle & Glanzmann, 1999). D is the diffusion coefficient (Equation 1.3.7) and R_{eff} is the effective reflection coefficient given by 0.493 for the refraction indices of tissue and air (Haskell et al., 1994). This solution has been verified against many flow modalities to demonstrate quantitative flow changes in various tissues (Buckley et al., 2014; Mesquita et al., 2011). When applied to adults, cerebral perfusion can be underestimated due to partial volume errors from thick extracerebral layers (Durduran et al., 2004; Gagnon, Selb, & Boas, 2008).

A few approaches have emerged to account for tissue heterogeneity in the adult head including the application of a correction factor based on partial volume estimates (Durduran et al., 2004). Another approach is to weight the fit of the semi-infinite homogeneous model towards shorter correlation times since these are most sensitive to longer photon pathlengths (i.e. photons that have most likely propagated in deep tissue) (Selb et al., 2014). However, these methods only enhance sensitivity to CBF from the measured DCS signal and do not completely separate the effects of light propagation in the various tissues.

An analytical solution to the CDE (Equation 1.5.4) that separates flow in multiple tissue layers by accounting for extracerebral tissue thickness have been shown to improve the sensitivity to CBF (Gagnon, Desjardins, Jehanne-Lacasse, Bherer, & Lesage, 2008), and to detect CBF increases in the motor cortex during a functional task (Jun Li et al.,

2005). To-date, only a few studies have employed a multi-layer model, and there have been no validations of this approach (Jaillon, Li, Dietsche, Elbert, & Gisler, 2007; J Li et al., 2008; Jun Li et al., 2005).

1.5.4 DCS Instrumentation

To measure $g_2(\rho,\tau)$, some of the main components include: a continuous-wave, long-coherent (>5 m) light source, a single-mode detection fiber, and a fast counting board and fast detection system (i.e. avalanche photodiode capable of detecting single photons on the order of μs). Regarding the source, a long coherence length (typically >5 m) is required to ensure the light emitted by the source are spatially in-phase for distances much greater than typical photon pathlengths through tissue (<1 m; estimated from Figure 1-4). Therefore, the decay of correlation is a result from multiple scattering interactions with RBCs in tissue and not due to the laser. A single-mode detection fiber has a very small core radius (~2 μm) comparable to the wavelength of light, which enables selection of a single scattered electric field component (i.e. receiver mode) to maximize speckle contrast. However, the small core diameter and low numerical aperture limit SNR, making it difficult to acquire DCS data at larger source-detector distances (>3 cm), which is often used to improve depth sensitivity. Strategic use of a few-mode detection fiber can enhance SNR by increasing the photon count rate, but sacrifices speckle contrast (Dietsche et al., 2007; Gisler et al., 1995; He, Lin, Shang, Shelton, & Yu, 2013).

A fast detection system, such as a single-photon avalanche photodiode (SPAD), and a fast counting board are required for high temporal resolution and high SNR. Temporal resolution may be traded in to enhance SNR, but this is not ideal for real-time monitoring of tissue blood flow. A multi-tau correlator board bins the photons from a time range scale of μs to seconds and computes the autocorrelation function. Recent innovative techniques that efficiently select only relevant correlation times have shown to improve the speed of data acquisition and reduce noise (Baker et al., 2014; D. Wang et al., 2016). Ultimately, this may enhance the depth sensitivity of DCS techniques since long photon pathlengths are most likely to travel deep in the tissue and are best

representative of the autocorrelation function at early correlation times (Selb et al., 2014), which are most susceptible to noise.

1.6 A Review of Current Applications and Limitations of DCS

Over the past 10 years, the applications of DCS have grown rapidly due to its clinical promise (i.e. safe, non-invasive, inexpensive, good depth sensitivity, real-time data acquisitions, portability) as a bedside monitor of cerebral perfusion. The clinical applications have been supplemented by a plethora of validation studies, which have been summarized in a number of recent review articles (Buckley et al., 2014; Durduran, Choe, et al., 2010; Durduran & Yodh, 2014; Mesquita et al., 2011; Yodh, 2009).

Table 1-1: A list of DCS validation studies; modified from (Mesquita et al., 2011)

Sample	Perturbation	Comparison Modality	R^2	Slope	Reference
Mouse tumour	PDT	Power Doppler ultrasound	N/A	0.97	(Menon et al., 2003)
Rat	Hypocapnia	Laser Doppler	0.94	1.3	(Durduran, 2004)
Mouse tumour	PDT	Doppler ultrasound	N/A	Agreement	(Yu, Durduran, Zhou, et al., 2005)
Mouse tumour	Antivascular therapy	DCE ultrasound	N/A	Agreement	(Sunar et al., 2007)
Human calf muscle	Cuff inflation/deflation	ASL MRI	>0.77	1.5-1.7	(Yu et al., 2007)
Piglet	TBI	Fluorescent microspheres	0.63	0.4	(Zhou et al., 2009)
Premature neonates	Absolute baseline	TCD	0.91	0.9	(Buckley, Cook, Durduran, & Kim, 2009)
Premature neonates	Absolute baseline	TCD	0.53	N/A	(Roche-Labarbe et al., 2010)
Term neonates	Hypercapnia	ASL MRI	0.7	0.85	(Durduran, Zhou, et al., 2010)
Mouse	Femoral artery occlusion	Laser Doppler	>0.8	0.96-1.07	(Mesquita et al., 2010)
Rat	Hypercapnia	ASL MRI	~0.84	0.75	(Carp, Dai, Boas, Franceschini, & Kim, 2010)
Adult human	Pressors and hyperventilation	Xenon CT	0.73	1.1	(Kim et al., 2010)
Adult human	Acetazolamide	TCD	N/A	Agreement	(Zirak, Delgado-Mederos, Martí-Fàbregas, & Durduran, 2010)
Piglet	Hypo-/hyper-capnia	DCE NIRS	0.93	1.05	(Diop, Verdecchia, Lee, & St Lawrence, 2011)
Children (JV)	Hypercapnia	PC MRI	0.77	0.91	(Buckley et al., 2012)
Children (SVC)	Hypercapnia	PC MRI	0.59	0.99	(Buckley et al., 2012)
Neonates CHD	Absolute Hypercapnia	PC MRI	0.67	0.40	(Jain et al., 2014)
Neonates CHD	Hypercapnia	PC MRI	0.62	1.01	(Jain et al., 2014)
Neonates PDA	Indomethacin Infusion	DCE NIRS	0.68	0.43	(Diop, Kishimoto, Toronov, Lee, & Lawrence, 2015)

A list of the abbreviations in Table 1-1: A list of DCS validation studies; modified from (Mesquita et al., 2011): Dynamic contrast enhanced (DCE) NIRS; Arterial spin labeling (ASL) MRI; Phase-contrast (PC) MRI; Photodynamic therapy (PDT); Transcranial Doppler ultrasound (TCD); Congenital heart defect (CHD); Patent ductus arteriosus (PDA); Superior vena cava (SVC); Jugular vein (JV).

Overall, the majority of validation studies listed in Table 1-1 have concluded that DCS can accurately track relative changes in blood flow in various tissues. Generally, DCS is used to measure relative flow since quantification requires accurate estimation of the tissue optical properties (Diop et al., 2011; Irwin et al., 2011; Z. Li et al., 2015). However, some validation studies (included in Table 1-1) have correlated BFIs measured by DCS with perfusion (i.e. transcranial Doppler ultrasound, ASL-MRI, DCE NIRS, and phase-contrast MRI) suggesting that the BFIs measured by DCS represent true perfusion, despite its diffusion units [cm^2/s] (Buckley et al., 2009; Diop et al., 2011; Jain et al., 2014; Roche-Labarbe et al., 2010; Yu et al., 2007). The conversion of a BFI obtained by DCS into perfusion units (mL/100g/min) can be achieved by calibrating DCS from an independent perfusion measurement, such as by DCE NIRS (Section 1.4.3) (Diop et al., 2011; Gurley, Shang, & Yu, 2012; Z. Li et al., 2015). This combination of DCS and TR NIRS also provides a means of quantifying $CMRO_2$ by combining StO_2 (Section 1.4.2) and CBF measurements.

1.6.1 Applications of DCS in Various Tissue Types

Tissue hemodynamics are important for providing sufficient oxygen to meet metabolic demands. In particular, highly vascularized tissues, such as brain and tumour, are attractive applications to monitor changes in blood flow by DCS.

Monitoring hemodynamics of skeletal muscle is another growing clinical application of DCS, particularly for peripheral artery disease. Following calf muscle ischemia, which was induced by ligating a femoral artery in mice, reperfusion was established by DCS in 90 % of healthy mice (Mesquita et al., 2010). Another study acquired optical data in healthy human arm and leg flexor muscles during arterial cuff occlusion detecting rapid drops in blood flow, but only gradual decreases of oxygen saturation were found (Yu, Durduran, Lech, et al., 2005). Recently, the BFI measured by DCS at baseline has been calibrated by a venous-occlusion technique, in which, the increase rate of blood volume following the release of an occluding artery is converted to perfusion units by assuming an average hemoglobin concentration and accounting for hemoglobin molecular weight (Gurley et al., 2012). Later this calibration technique was further investigated to confirm the total hemoglabin increase rate due to venous-occlusion

agrees well with BFIs measured by DCS (Z. Li et al., 2015). However, exercise protocols are susceptible to motion artifacts that can distort the DCS signal. Co-registration techniques are required to separate true blood flow response from motion artifacts (Gurley et al., 2012; Shang, Symons, Durduran, Yodh, & Yu, 2010).

In oncology, DCS has been used to characterize tumour hemodynamics with the goals of detecting highly vascularized tumours and assessing the efficacy of therapeutic treatments in pre-clinical experiments (Becker, Paquette, Keymel, Henderson, & Sunar, 2010; Sunar et al., 2007; Yu, Durduran, Zhou, et al., 2005) and clinical studies (Choe et al., 2014; Durduran et al., 2005; Sunar et al., 2010; Yu et al., 2006). In 2005, Durduran et al. observed increased blood flow in patients with breast tumours, likely due to angiogenesis (Durduran et al., 2005). Since this original study, cancer applications of DCS have extended to monitoring photodynamic therapy (PDT) of prostate cancer and basal cell carcinomas (Becker et al., 2010; Yu et al., 2006). In addition, the effects of chemotherapy on breast cancer, and head and neck tumours have been investigated (Sunar et al., 2010; Zhou et al., 2007). All studies observed significant flow effects early (from minutes to the first week) following cancer therapy treatment, highlighting the potential of DCS as a tool for monitoring cancer hemodynamic responses; however, all studies had relatively small sample sizes (<8). Recently, a moderate-sized clinical study (32 patients) measured significantly high flow in malignant breast cancer by a hand-held DCS probe (Choe et al., 2014). These studies illustrate the potential for DCS to identify malignant cancer and monitor optically accessible tumours in the clinic.

1.6.2 Applications of DCS in Brain Tissue

The primary application of DCS has been to monitor CBF. Due to the appeal that signal contamination from extracerebral tissue is minimal and photons predominantly interrogate cortical tissue, many animal studies have been conducted in rats, mice and piglets (Buckley et al., 2014; Durduran & Yodh, 2014). Animal models that mimic neurocritical conditions have been used to demonstrate the capability of DCS to track real-time flow changes. For example, in the rat brain, relative CBF during cortical spreading depression observed an initially strong increase followed by a sustained decrease (Zhou et al., 2006). Shang et al. showed that DCS could detect large reductions

in CBF (> 75%) during bilateral occlusion of the common carotid arteries in mice, as well as reperfusion following unclipping (Shang, Chen, Toborek, & Yu, 2011). A recent study using a TBI mouse model demonstrated that baseline CBF could be used as a biomarker of cognitive outcome following repetitive concussions (Buckley et al., 2015). DCS has also been used to detect the sizable CBF reduction that occurs following acute TBI in a nonimpact inertial rotational swine model (Zhou et al., 2009).

Due to its good temporal resolution (i.e. order of seconds), DCS has been used to detect the CBF response to functional activation in humans. The first application was by Durduran et al. who measured the CBF increase in the motor cortex during a simple finger tapping task (Durduran et al., 2004). This study paved the way for investigations of functional monitoring of cerebral hemodynamics by DCS. For example, various oral tasks were investigated to better understand speech impediments, such as stuttering (Tellis, Mesquita, & Yodh, 2011). While its adaptation to functional activation tasks illustrated the versatility of DCS, its greatest promise is as a bedside monitor in the ICU.

Clinical studies have investigated patient management techniques, such as administering medication and head-of-bed (HOB) strategies. First, administrated dose of $NaHCO_3$, which is a common medication for acidemia in the ICU, was observed to linearly relate to CBF increases (Buckley et al., 2013). Also, HOB strategies were investigated in patients with acute ischemic stroke to observe the effects of CBF by adjusting the angle of recline of the patient (Durduran et al., 2009; Favilla et al., 2014). Typically, stroke patients resulted in significant increases of CBF by HOB techniques; however, some patients responded paradoxically, highlighting the importance of monitoring neurocritical management techniques to individualize patient care.

1.6.3 Hybrid Optical Modality to Measure $CMRO_2$

As mentioned earlier, the combination of DCS and NIRS provides a safe and non-invasive means to assess $CMRO_2$ at the bedside (Boas & Franceschini, 2011; Buckley et al., 2014; Durduran, Choe, et al., 2010; Durduran & Yodh, 2014). The first study to combine photon diffusion methods by a hybrid DCS/NIRS technology measured regional blood flow, hemoglobin concentration and blood oxygen saturation in rat brain (Cheung

et al., 2001). The appeal for an all-optical hybrid system capable of measuring cerebral hemodynamics and cerebral oxygen metabolism in tissue has prompted extensive research. Next, a hybrid optical system was used to monitor $CMRO_2$ changes during focal cerebral ischemia in rats (Culver et al., 2003), which was adapted to the adult brain (Durduran et al., 2004).

Over the last few years, interest in the use of an all-optical hybrid modality has expanded towards studies measuring relative changes of cerebral metabolism in healthy infants (Buckley et al., 2009; Goff, Buckley, Durduran, Wang, & Licht, 2010; Roche-Labarbe et al., 2010). The idea to measure cerebral metabolism with NIRS is not novel (Franceschini et al., 2007), but computing $CMRO_2$ with the inclusion of DCS reduced intersubject variability (Roche-Labarbe et al., 2010). This combination has been used to map developmental changes in the early stages of life, in which the measured average metabolism increased by 40 % in newborns over their first 6 weeks of life (Roche-Labarbe et al., 2010). Roche-Labarbe et al. later reported lower $CMRO_2$ values at lower gestational ages (Roche-Labarbe et al., 2012). Furthermore, a couple studies observed increases in $CMRO_2$ in the injured neonatal brain compared to healthy infants, and suggest $CMRO_2$ is a better biomarker of brain injury than StO_2 alone (Grant, Roche-Labarbe, & Surova, 2009; Lin et al., 2013). Aside from monitoring brain development, a number of studies investigated effects of therapeutic treatments in sick infants. For example, one study found metabolism to be unaltered during hypercapnia in neonates with congenital heart disease, despite significant increases in CBF and oxyhemoglobin (Durduran, Zhou, et al., 2010). Recently, another study investigated infants with patent ductus arteriosus who underwent treatment by indomethacin, a well-known vasoconstrictor, and found reductions in CBF and StO_2, despite no changes in $CMRO_2$, before and after pharmaceutical ingestion (Diop et al., 2015). Monitoring the neurovascular coupling of a developing brain by DCS/NIRS provides a means for early detection of brain injury and monitoring the efficacy of therapeutic treatment.

1.6.4 Limitations

Despite the employment of DCS in a number of applications, both pre-clinical and clinical, there remain some limitations that prevent the translation of DCS to the ICU.

These include susceptibility to motion, sensitivity to probe pressure, low SNR, separation of blood flow in cerebral and extracerebral tissues, and flow quantification.

Intensity fluctuations measured by DCS are caused primarily by photon interactions with dynamic scatterers in the interrogated medium. However, additional fluctuations are falsely detected from static scatterers due to the motion of probes, which increase the variability of the estimated BFI (Belau et al., 2010). A few possible solutions are suggested, including glueing the fibers with collodion (Yücel, Selb, Boas, Cash, & Cooper, 2014), time gating with a dynamometer (Shang et al., 2010), and analytical approaches that filter artifacts due to motion, similarly to functional NIRS techniques (Cooper et al., 2012). The latter idea is perhaps the most feasible but little work has focused on reducing errors due to motion. Current data acquisition setups require the optical probes to be secured strongly to the interrogated medium in order to limit motion artifacts.

A more prominent source of error than motion is the effects of contact pressure between the skin and the DCS probes. Typical pressure (i.e. 20-55 mmHg) required to hold the optical probes in place on the surface of tissue have been shown to influence the DCS signal in scalp or muscle (Baker et al., 2015; Mesquita et al., 2013). To avoid errors caused by pressure variations, non-contact optical probes have been developed (Cheung et al., 2001; T. Li et al., 2013; Yu, Durduran, Zhou, et al., 2005). Although this technique is an interesting approach, there are limitations, including detection of stray light and loss of depth sensitivity. Recent advancements in non-contact probes show comparable performance to contact probes, (Han et al., 2015; He et al., 2015), but further technological advancements are required before a non-contact probe can be used to assess hemodynamics in deep tissue, such as cortical tissue in adults. Furthermore, applying a non-contact emission probe to the head would be highly susceptible to local inhomogeneities, such as hair, which limit measurements of the prefrontal cortex via the forehead. Advantageously, a contact probe provides optimal optical coupling through hair, especially by designs of the light collection tip, such as a funnel-shaped tip, which displaces hair from the detection field of view (Dietsche et al., 2007).

An unavoidable complication of optical methods is the limited depth penetration of NIR light in a highly scattering medium, such as tissue. The highly scattering medium makes it difficult to achieve excellent SNR at large source-detector distances since less light reflected from the medium is detected. A simple solution to improving the SNR is to increase the laser emission power, but to avoid excessive heating of the skin, the output power of a continuous laser must be below 28.4 mW (Baker, 2015). In addition, less light is collected in DCS compared to other NIRS techniques, due to the requirement of single-mode detection fibers. Dietsche et al. improved SNR by collecting light from multiple fibers, but each fiber must be coupled to its own detector, which can become expensive (Dietsche et al., 2007).

Another approach for improving SNR or depth sensitivity is by developing robust instrumentation or data analysis techniques. Rather than computing an autocorrelation curve at multiple delay times, single correlation times may be used to monitor flow changes, and the early correlation times may be utilized for better depth sensitivity (Baker et al., 2014). Also, combining DCS analysis with a software correlator, rather than the conventional hardware correlator, may provide better fitting results and is less expensive (Dong et al., 2012). Recently, a new software correlator that computes the autocorrelation function at selected correlation times was shown to provide temporal resolutions capable of detecting heart-rate fluctuations in CBF (Wang et al., 2016).

The innovative DCS technologies that improve SNR provide a means to accurately measure flow changes in deep tissue, such as cortical tissue in the adult head. Extracerebral tissues are known to contaminate the optical signal, which underestimates the BFI measured by DCS (Durduran et al., 2004; Gagnon, Desjardins, et al., 2008). Partial volume errors are a complicated problem with NIR techniques due to the poor spatial resolution. Originally, a simple approach of applying a correction factor based on partial volume estimates was suggested (Durduran et al., 2004), but extracerebral tissue thickness differences between subjects vary the sensitivity of brain tissue. Furthermore, techniques that adjust the weight of the fit to early correlation times increase the sensitivity to deeper tissue (Selb et al., 2014); however, they do not separate light propagation in multiple tissue types.

A method to separate flow indices in different tissue layers (scalp, skull, and brain) was used to measure functional activation due to finger tapping (Jun Li et al., 2005), but only a few studies have investigated the feasibility of using layered models to improve the accuracy of CBF monitoring (Gagnon, Desjardins, et al., 2008; Jaillon et al., 2007; Jun Li et al., 2005). The importance of separating scalp and brain is critical since flow in the scalp dominates the DCS signal (Mesquita et al., 2013). A recent algorithm has been proposed to separate scalp blood flow (SBF) and CBF by modulating the pressure between the tissue surface and optical probes (Baker et al., 2015); however, this technique relies on a pressure calibration stage that induces a flow change in the scalp only. The authors present an intriguing technique that would be strengthened by validation with independent flow measures. A model to separate flow estimates in the brain and the scalp without requiring calibration would be ideal.

Another caveat of flow measured by DCS is the inability to assess absolute perfusion. Currently, DCS can only measure relative changes in blood flow due to the arbitrary units [cm^2/s] of a BFI. Diop et al. proposed an all-optical approach to convert the DCS flow index into units of absolute perfusion by measuring CBF by DCE NIRS (Diop et al., 2011). This technique could also be extended to monitor $CMRO_2$, which is one of the motivations of this thesis.

1.7 Research Objectives

The goal of this doctoral work was to develop a non-invasive optical imaging system capable of monitoring blood flow and oxygenation in the cerebral microvasculature of patients at the bedside. Considering the main goal to develop DCS towards the clinic, the following objectives were addressed:

1. Design and construct an optical imaging system capable of measuring flow and oxygenation.

2. Quantify $CMRO_2$ by an all-optical method.

3. Investigate the best model to characterize moving scatterers in the brain.

4. Develop a multi-layered model to improve depth sensitivity.

5. Validate DCS with computed tomography perfusion (CTP).

Each chapter in this dissertation represents an advancement in the field with the ultimate goal of developing a safe, non-invasive neuromonitoring device for patients in the ICU.

1.8 Thesis Outline

The remainder of the thesis is divided into three chapters that outline published studies and a final concluding chapter.

1.8.1 Measurements of Absolute Cerebral Metabolic Rate of Oxygen by a Hybrid Optical Modality that Includes Diffuse Correlation Spectroscopy (Chapter 2)

An all-optical imaging technique was employed to measure changes in absolute $CMRO_2$ in newborn piglets, which were validated against an invasive gold standard method. This chapter is based on the paper entitled "Quantifying the cerebral metabolic rate of oxygen by combining diffuse correlation spectroscopy and time-resolved near-infrared spectroscopy", published in the *Journal of Biomedical Optics* in 2013 by Verdecchia K, Diop M, Lee T-Y, and St. Lawrence K.

1.8.2 Measurements of Cerebral Blood Flow in Pigs by Diffuse Correlation Spectroscopy on the Exposed Cortex (Chapter 3)

Motivation for describing motion of RBCs as Brownian diffusion is not well understood but is applied frequently by DCS studies due to its superior fit than other models. This chapter investigates the best flow model to characterize blood diffusion in cortical tissue by placing the optical probes directly on the exposed brain of adolescent pigs in order to remove any confounding effects of extracerebral tissues. Furthermore, the validity of the CBF changes measured by DCS was compared to CTP. This chapter is based on the paper entitled "Assessment of the best flow model to characterize diffuse correlation spectroscopy data acquired directly on the brain", published in *Biomedical Optics Express* in 2015 by Verdecchia K, Diop M, Morrison LB, Lee T-Y, and St. Lawrence K.

1.8.3 Measurements of Cerebral Blood Flow in Adolescent Pigs by Diffuse Correlation Spectroscopy (Chapter 4)

In the adult head, the extracerebral tissues highly dominate an optical signal resulting in underestimating CBF changes by DCS. A multi-layered model was implemented in adolescent pigs to separate the blood flow in cerebral and extracerebral tissues. Furthermore, the validity of the CBF changes measured by a multi-layered DCS technique was compared to CTP. This chapter is based on the paper entitled "Assessment of a multi-layered diffuse correlation spectroscopy method to monitor cerebral blood flow changes in adults", published in *Biomedical Optics Express* in 2016 by Verdecchia K, Diop M, Lee A, Morrison LB, Lee T-Y, and St. Lawrence K.

1.8.4 Conclusion and Future Work (Chapter 5)

In the final chapter, the main results from the thesis are summarized and a discussion is provided on their experimental and clinical implications. Based on the findings in this thesis, areas of interest for future work are discussed and principle conclusions are presented.

1.9 References

Ackerson, B. J., Dougherty, R. L., Reguigui, N. M., & Nobbmann, U. (1992). Correlation transfer - Application of radiative transfer solution methods to photon correlation problems. *Journal of Thermophysics and Heat Transfer*, *6*(4), 577–588. doi:10.2514/3.11537

Alonso, A., Ebert, A. D., Kern, R., Rapp, S., Hennerici, M. G., & Fatar, M. (2015). Outcome Predictors of Acute Stroke Patients in Need of Intensive Care Treatment. *Cerebrovascular Diseases*, *40*(1-2), 10–17. doi:10.1159/000430871

Andrews, P. J. D., Sleeman, D. H., Statham, P. F. X., McQuatt, A., Corruble, V., Jones, P. a, … Macmillan, C. S. a. (2002). Predicting recovery in patients suffering from traumatic brain injury by using admission variables and physiological data: a comparison between decision tree analysis and logistic regression. *Journal of Neurosurgery*, *97*(2), 326–336. doi:10.3171/jns.2002.97.2.0326

Arabi, Y., Memish, Z. A., Balkhy, H. H., Francis, C., Ferayan, A., Al Shimemeri, A., & Almuneef, M. A. (2005). Ventriculostomy-associated infections: Incidence and risk factors. *American Journal of Infection Control*, *33*(3), 137–143. doi:10.1016/j.ajic.2004.11.008

Aries, M. J. H., Elting, J. W., De Keyser, J., Kremer, B. P. H., & Vroomen, P. C. A. J. (2010). Cerebral autoregulation in stroke: A review of transcranial doppler studies. *Stroke*, *41*(11), 2697–2704. doi:10.1161/STROKEAHA.110.594168

Arridge, S. R., Cope, M., & Delpy, D. T. (1992). The theoretical basis for the determination of optical pathlengths in tissue: temporal and frequency analysis. *Physics in Medicine and Biology*, *37*(7), 1531–60. Retrieved from http://www.ncbi.nlm.nih.gov/pubmed/1631197

Baker, W. B. (2015). OPTICAL CEREBRAL BLOOD FLOW MONITORING OF MICE TO MEN.

Baker, W. B., Parthasarathy, A. B., Busch, D. R., Mesquita, R. C., Greenberg, J. H., & Yodh, a G. (2014). Modified Beer-Lambert law for blood flow. *Biomedical Optics Express*, *5*(11), 4053–75. doi:10.1364/BOE.5.004053

Baker, W. B., Parthasarathy, A. B., Ko, T. S., Busch, D. R., Abramson, K., Tzeng, S.-Y., … Yodh, A. G. (2015). Pressure modulation algorithm to separate cerebral hemodynamic signals from extracerebral artifacts. *Neurophotonics*, *2*(3), 035004. doi:10.1117/1.NPh.2.3.035004

Becker, T. L., Paquette, A. D., Keymel, K. R., Henderson, B. W., & Sunar, U. (2010). Monitoring blood flow responses during topical ALA-PDT. *Biomedical Optics Express*, *2*(1), 123–30. doi:10.1364/BOE.2.000123

Belau, M., Ninck, M., Hering, G., Spinelli, L., Contini, D., Torricelli, A., & Gisler, T. (2010). Noninvasive observation of skeletal muscle contraction using near-infrared time-resolved reflectance and diffusing-wave spectroscopy. *Journal of Biomedical Optics*, *15*(5), 057007. doi:10.1117/1.3503398

Berne, B., & Pecora, R. (1976). *Dynamic light scattering*. Wiley, New York.

Bershad, E. M., Feen, E. S., Hernandez, O. H., Suri, M. F. K., & Suarez, J. I. (2008). Impact of a specialized neurointensive care team on outcomes of critically ill acute ischemic stroke patients. *Neurocritical Care*, *9*(3), 287–292. doi:10.1007/s12028-008-9051-5

Boas, D., Campbell, L., & Yodh, A. G. (1995). Scattering and imaging with diffusing temporal field correlations. *Physical Review Letters*, *75*(9), 1855–1858. Retrieved from http://link.aps.org/doi/10.1103/PhysRevLett.75.1855

Boas, D., & Franceschini, M. A. (2011). Haemoglobin oxygen saturation as a biomarker: the problem and a solution. *Philosophical Transactions. Series A, Mathematical, Physical, and Engineering Sciences*, *369*(1955), 4407–24. doi:10.1098/rsta.2011.0250

Boas, D., & Yodh, A. G. (1997). Spatially varying dynamical properties of turbid media probed with diffusing temporal light correlation. *Journal of the Optical Society of America A*, *14*(1), 192–215. doi:10.1364/JOSAA.14.000192

Bonner, R., & Nossal, R. (1981). Model for laser Doppler measurements of blood flow in tissue. *Analysis*, *20*(12), 2097–2107. Retrieved from http://www.opticsinfobase.org/abstract.cfm?id=24957

Bouma, G. J., & Muizelaar, J. P. (1992). Cerebral blood flow, cerebral blood volume, and cerebrovascular reactivity after severe head injury. *Journal of Neurotrauma*, *9 Suppl 1*(March), S333–48. Retrieved from http://www.ncbi.nlm.nih.gov/pubmed/1588625

Bouma, G. J., Muizelaar, J. P., Bandoh, K., & Marmarou, A. (1992). Blood pressure and intracranial pressure-volume dynamics in severe head injury: relationship with cerebral blood flow. *Journal of Neurosurgery*, *77*(1), 15–19. doi:10.3171/jns.1992.77.1.0015

Bratton, S. L., Chestnut, R. M., Ghajar, J., McConnell Hammond, F. F., Harris, O. a., Hartl, R., … Wright, D. W. (2007). VIII. Intracranial Pressure Thresholds. *Journal of Neurotrauma*, *24*(supplement 1), S–55–S–58. doi:10.1089/neu.2007.9988

Brazy, J. E., Lewis, D. V, Mitnick, M. H., & Jobsis, F. F. (1985). Noninvasive monitoring of cerebral oxygenation in preterm infants: preliminary observations. *Pediatrics*, *75*(2), 217–225.

Brown, D. W., Picot, P. a, Naeini, J. G., Springett, R., Delpy, D. T., & Lee, T.-Y. (2002). Quantitative near infrared spectroscopy measurement of cerebral hemodynamics in newborn piglets. *Pediatric Research*, *51*(5), 564–70. Retrieved from http://www.ncbi.nlm.nih.gov/pubmed/11978878

Buckley, E. M., Cook, N., Durduran, T., & Kim, M. (2009). Cerebral hemodynamics in preterm infants during positional intervention measured with diffuse correlation spectroscopy and transcranial Doppler ultrasound. *Optics Express*, *17*(15), 12571–12581. Retrieved from http://www.opticsinfobase.org/abstract.cfm?URI=oe-17-15-12571

Buckley, E. M., Hance, D., Pawlowski, T., Lynch, J., Wilson, F. B., Mesquita, R. C., … Yodh, A. G. (2012). Validation of diffuse correlation spectroscopic measurement of cerebral blood flow using phase-encoded velocity mapping magnetic resonance imaging. *Journal of Biomedical Optics*, *17*(3), 037007. doi:10.1117/1.JBO.17.3.037007

Buckley, E. M., Miller, B. F., Golinski, J. M., Sadeghian, H., McAllister, L. M., Vangel, M., … Whalen, M. J. (2015). Decreased microvascular cerebral blood flow assessed by diffuse correlation spectroscopy after repetitive concussions in mice. *Journal of Cerebral Blood Flow & Metabolism*, *35*(12), 1995–2000. doi:10.1038/jcbfm.2015.161

Buckley, E. M., Naim, M. Y., Lynch, J. M., Goff, D. a, Schwab, P. J., Diaz, L. K., … Licht, D. J. (2013). Sodium bicarbonate causes dose-dependent increases in cerebral blood flow in infants and children with single-ventricle physiology. *Pediatric Research*, *73*(5), 668–73. doi:10.1038/pr.2013.25

Buckley, E. M., Parthasarathy, A. B., Grant, P. E., Yodh, A. G., & Franceschini, M. A. (2014). Diffuse correlation spectroscopy for measurement of cerebral blood flow: future prospects. *Neurophotonics*, *1*(1), 011009. doi:10.1117/1.NPh.1.1.011009

Carp, S. A., Dai, G. P., Boas, D., Franceschini, M. A., & Kim, Y. R. (2010). Validation of diffuse correlation spectroscopy measurements of rodent cerebral blood flow with simultaneous arterial spin labeling MRI; towards MRI-optical continuous cerebral metabolic monitoring. *Biomedical Optics Express*, *1*(2), 553–565. doi:10.1364/BOE.1.000553

Chen, H. I., Stiefel, M. F., Oddo, M., Milby, A. H., Maloney-Wilensky, E., Frangos, S., … LeRoux, P. D. (2011). Detection of cerebral compromise with multimodality monitoring in patients with subarachnoid hemorrhage. *Neurosurgery*, *69*(1), 53–63. doi:10.1227/NEU.0b013e3182191451

Cheung, C., Culver, J. P., Takahashi, K., Greenberg, J. H., & Yodh, A. G. (2001). In vivo cerebrovascular measurement combining diffuse near-infrared absorption and correlation spectroscopies. *Physics in Medicine and Biology*, *46*(8), 2053–65. Retrieved from http://www.ncbi.nlm.nih.gov/pubmed/11512610

Choe, R., Putt, M. E., Carlile, P. M., Durduran, T., Giammarco, J. M., Busch, D. R., … Yodh, A. G. (2014). Optically measured microvascular blood flow contrast of malignant breast tumors. *PLoS ONE*, *9*(6), 1–10. doi:10.1371/journal.pone.0099683

Coles, J. P., Minhas, P. S., Fryer, T. D., Smielewski, P., Aigbirihio, F., Donovan, T., … Menon, D. K. (2002). Effect of hyperventilation on cerebral blood flow in traumatic head injury: clinical relevance and monitoring correlates. *Critical Care Medicine*, *30*(9), 1950–1959. doi:10.1097/00003246-200209000-00002

Connolly, E. S., Rabinstein, A. A., Carhuapoma, J. R., Derdeyn, C. P., Dion, J., Higashida, R. T., … Vespa, P. (2012). Guidelines for the management of aneurysmal subarachnoid hemorrhage: A guideline for healthcare professionals from the american heart association/american stroke association. *Stroke*, *43*(6), 1711–1737. doi:10.1161/STR.0b013e3182587839

Cooper, R. J., Selb, J., Gagnon, L., Phillip, D., Schytz, H. W., Iversen, H. K., … Boas, D. A. (2012). A systematic comparison of motion artifact correction techniques for functional near-infrared spectroscopy. *Frontiers in Neuroscience*, *6*(OCT), 1–10. doi:10.3389/fnins.2012.00147

Cope, M. (1991). *The Application of Near Infrared Spectroscopy to Non Invasive Monitoring of Cerebral Oxygenation in the Newborn Infant*.

Cremer, O. L., van Dijk, G. W., van Wensen, E., Brekelmans, G. J. F., Moons, K. G. M., Leenen, L. P. H., & Kalkman, C. J. (2005). Effect of intracranial pressure monitoring and targeted intensive care on functional outcome after severe head injury. *Critical Care Medicine*, *33*(10), 2207–2213. doi:10.1097/01.CCM.0000181300.99078.B5

Culver, J. P., Durduran, T., Furuya, D., Cheung, C., Greenberg, J. H., & Yodh, A. G. (2003). Diffuse optical tomography of cerebral blood flow, oxygenation, and metabolism in rat during focal ischemia. *Journal of Cerebral Blood Flow and Metabolism*, *23*(8), 911–24. doi:10.1097/01.WCB.0000076703.71231.BB

Cummins, H. Z., & Swinney, H. L. (1970). III Light Beating Spectroscopy. In *Numerical Computing with MATLAB* (pp. 133–200). doi:10.1016/S0079-6638(08)70188-4

De Blasi, R. a, Fantini, S., Franceschini, M. a, Ferrari, M., & Gratton, E. (1995). Cerebral and muscle oxygen saturation measurement by frequency-domain near-infra-red spectrometer. *Medical & Biological Engineering & Computing*, *33*(2), 228–230. doi:10.1007/BF02523048

De Oliveira Manoel, A. L., Goffi, A., Marotta, T. R., Schweizer, T. A., Abrahamson, S., & Macdonald, R. L. (2015). The critical care management of poor-grade subarachnoid haemorrhage. *Critical Care*, *20*(1), 21. doi:10.1186/s13054-016-1193-9

De Oliveira Manoel, A. L., Jaja, B. N., Germans, M. R., Yan, H., Qian, W., Kouzmina, E., … Macdonald, R. L. (2015). The VASOGRADE: A Simple Grading Scale for Prediction of Delayed Cerebral Ischemia after Subarachnoid Hemorrhage. *Stroke*, *46*(7), 1826–1831. doi:10.1161/STROKEAHA.115.008728

Delpy, D. T., & Cope, M. (1997). Quantification in tissue near-infrared spectroscopy. *Philosophical Transactions of the Royal Society B: Biological Sciences*, *352*(1354), 649–659. doi:10.1098/rstb.1997.0046

Delpy, D. T., Cope, M., van der Zee, P., Arridge, S., Wray, S., & Wyatt, J. (1988). Estimation of optical pathlength through tissue from direct time of flight measurement. *Physics in Medicine and Biology*, *33*(12), 1433–42. doi:10.1088/0031-9155/33/12/008

Dhar, R., & Diringer, M. C. (2016). Cerebral blood flow. In S. Schwab, D. Hanley, & A. D. Mendelow (Eds.), *Critical Care of the Stroke Patient* (pp. 20–36). Cambridge: Cambridge University Press. doi:10.1017/CBO9780511659096.003

Dhar, R., Scalfani, M. T., Blackburn, S., Zazulia, A. R., Videen, T., & Diringer, M. (2012). Relationship between angiographic vasospasm and regional hypoperfusion in aneurysmal subarachnoid hemorrhage. *Stroke*, *43*(7), 1788–1794. doi:10.1161/STROKEAHA.111.646836

Dietsche, G., Ninck, M., Ortolf, C., Li, J., Jaillon, F., & Gisler, T. (2007). Fiber-based multispeckle detection for time-resolved diffusing-wave spectroscopy: characterization and application to blood flow detection in deep tissue. *Applied Optics*, *46*(35), 8506–8514. doi:10.1364/AO.46.008506

Diop, M., Kishimoto, J., Toronov, V., Lee, D. S. C., & Lawrence, K. S. (2015). Development of a combined broadband near-infrared and diffusion correlation system for monitoring cerebral blood flow and oxidative metabolism in preterm infants. *Biomedical Optics Express*, *6*(10), 3907–3918. doi:10.1364/BOE.6.003907

Diop, M., & St Lawrence, K. (2013). Improving the depth sensitivity of time-resolved measurements by extracting the distribution of times-of-flight. *Biomedical Optics Express*, *4*(3), 447–59. doi:10.1364/BOE.4.000447

Diop, M., & St. Lawrence, K. (2012). Deconvolution method for recovering the photon time-of-flight distribution from time-resolved measurements. *Optics Letters*, *37*(12), 2358–60. Retrieved from http://www.ncbi.nlm.nih.gov/pubmed/22739907

Diop, M., Tichauer, K. M., Elliott, J. T., Migueis, M., Lee, T.-Y., & St. Lawrence, K. (2010). Comparison of time-resolved and continuous-wave near-infrared techniques for measuring cerebral blood flow in piglets. *Journal of Biomedical Optics*, *15*(5), 057004. doi:10.1117/1.3488626

Diop, M., Verdecchia, K., Lee, T.-Y., & St Lawrence, K. (2011). Calibration of diffuse correlation spectroscopy with a time-resolved near-infrared technique to yield absolute cerebral blood flow measurements. *Biomedical Optics Express*, *2*(7), 2068. doi:10.1364/BOE.2.002068

Diringer, M. N., & Edwards, D. F. (2001). Admission to a neurologic/neurosurgical intensive care unit is associated with reduced mortality rate after intracerebral hemorrhage. *Critical Care Medicine*, *29*(3), 635–640.

Dong, L., Kudrimoti, M., Cheng, R., Shang, Y., Johnson, E. L., Stevens, S. D., … Yu, G. (2012). Noninvasive diffuse optical monitoring of head and neck tumor blood flow and oxygenation during radiation delivery. *Biomedical Optics Express*, *3*(2), 259–72. doi:10.1364/BOE.3.000259

Durduran, T. (2004). *Non-Invasive Measurements of Tissue Hemodynamics with Hybrid Diffuse Optical Methods*.

Durduran, T., Choe, R., Baker, W. B., & Yodh, A. G. (2010). Diffuse optics for tissue monitoring and tomography. *Reports on Progress in Physics*, *73*(7), 076701. doi:10.1088/0034-4885/73/7/076701

Durduran, T., Choe, R., Yu, G., Zhou, C., Tchou, J. C., Czerniecki, B. J., & Yodh, A. G. (2005). Diffuse optical measurement of blood flow in breast tumors. *Optics Letters*, *30*(21), 2915–7. Retrieved from http://www.ncbi.nlm.nih.gov/pubmed/16279468

Durduran, T., & Yodh, A. G. (2014). Diffuse correlation spectroscopy for non-invasive, micro-vascular cerebral blood flow measurement. *NeuroImage*, *85 Pt 1*, 51–63. doi:10.1016/j.neuroimage.2013.06.017

Durduran, T., Yu, G., Burnett, M. G., Detre, J. a, Greenberg, J. H., Wang, J., … Yodh, A. G. (2004). Diffuse optical measurement of blood flow, blood oxygenation, and metabolism in a human brain during sensorimotor cortex activation. *Optics Letters*, *29*(15), 1766–8. Retrieved from http://www.ncbi.nlm.nih.gov/pubmed/15352363

Durduran, T., Zhou, C., Buckley, E. M., Kim, M. N., Yu, G., Choe, R., … Licht, D. J. (2010). Optical measurement of cerebral hemodynamics and oxygen metabolism in neonates with congenital heart defects. *Journal of Biomedical Optics*, *15*(3), 037004. doi:10.1117/1.3425884

Durduran, T., Zhou, C., Edlow, B. L., Yu, G., Choe, R., Kim, M. N., … Detre, J. a. (2009). Transcranial optical monitoring of cerebrovascular hemodynamics in acute stroke patients. *Optics Express*, *17*(5), 3884–902. Retrieved from

http://www.pubmedcentral.nih.gov/articlerender.fcgi?artid=2724658&tool=pmcentrez&rendertype=abstract

Edwards, A. D., Wyatt, J. S., Richardson, C., Delpy, D. T., Cope, M., & Reynolds, E. O. (1988). Cotside measurement of cerebral blood flow in ill newborn infants by near infrared spectroscopy. *Lancet*, *2*(8614), 770–771. Retrieved from http://www.ncbi.nlm.nih.gov/entrez/query.fcgi?cmd=Retrieve&db=PubMed&dopt=Citation&list_uids=2901613

Elliott, J. T., Diop, M., Morrison, L. B., D'Esterre, C. D., Lee, T.-Y., & St Lawrence, K. (2014). Quantifying cerebral blood flow in an adult pig ischemia model by a depth-resolved dynamic contrast-enhanced optical method. *NeuroImage*, *94C*, 303–311. doi:10.1016/j.neuroimage.2014.03.023

Elliott, J. T., Diop, M., Tichauer, K. M., Lee, T.-Y., & St. Lawrence, K. (2010). Quantitative measurement of cerebral blood flow in a juvenile porcine model by depth-resolved near-infrared spectroscopy. *Journal of Biomedical Optics*, *15*(3), 037014. doi:10.1117/1.3449579

Elwell, C. E., Cope, M., Edwards, a D., Wyatt, J. S., Delpy, D. T., & Reynolds, E. O. (1994). Quantification of adult cerebral hemodynamics by near-infrared spectroscopy. *Journal of Applied Physiology*, *77*(6), 2753–60. Retrieved from http://www.ncbi.nlm.nih.gov/pubmed/7896617

Elwell, C. E., Henty, J. R., Leung, T. S., Austin, T., Meek, J. H., Delpy, D. T., & Wyatt, J. S. (2005). Measurement of CMRO2 in neonates undergoing intensive care using near infrared spectroscopy. *Advances in Experimental Medicine and Biology*, *566*, 263–8. doi:10.1007/0-387-26206-7_35

English, S. W., Turgeon, A. F., Owen, E., Doucette, S., Pagliarello, G., & McIntyre, L. (2013). Protocol management of severe traumatic brain injury in intensive care units: A systematic review. *Neurocritical Care*, *18*(1), 131–142. doi:10.1007/s12028-012-9748-3

Fantini, S., Franceschini, M. A., Maier, J., Walker, S., Barbieri, B., & Gratton, E. (1995). Frequency-domain multichannel optical detector for noninvasive tissue spectroscopy and oximetry. *Optical Engineering*, *34*(1), 32. doi:10.1117/12.183988

Favilla, C. G., Mesquita, R. C., Mullen, M., Durduran, T., Lu, X., Kim, M. N., … Detre, J. A. (2014). Optical Bedside Monitoring of Cerebral Blood Flow in Acute Ischemic Stroke Patients During Head-of-Bed Manipulation. *Stroke*, *45*(5), 1269–1274. doi:10.1161/STROKEAHA.113.004116

Ferrari, M., Binzoni, T., & Quaresima, V. (1997). Oxidative metabolism in muscle. *Philosophical Transactions of the Royal Society B: Biological Sciences*, *352*(1354), 677–683. doi:10.1098/rstb.1997.0049

Franceschini, M. A., Thaker, S., Themelis, G., Krishnamoorthy, K. K., Bortfeld, H., Diamond, S. G., … Grant, P. E. (2007). Assessment of infant brain development with frequency-domain near-infrared spectroscopy. *Pediatric Research*, *61*(5 Pt 1), 546–51. doi:10.1203/pdr.0b013e318045be99

Gagnon, L., Desjardins, M. 'R., Jehanne-Lacasse, J., Bherer, L., & Lesage, F. Ú. Ú. (2008). Investigation of diffuse correlation spectroscopy in multi-layered media including the human head. *Optics Express*, *16*(20), 15514–15530. Retrieved from http://www.opticsinfobase.org/abstract.cfm?id=172103

Gagnon, L., Selb, J., & Boas, D. (2008). Measurements of Hemoglobin Concentrations in the Human Forehead Using Time-Resolved Reflectance. In *Biomedical Optics* (Vol. 1, pp. 5–7). Retrieved from http://www.opticsinfobase.org/abstract.cfm?URI=BIOMED-2008-BSuE73

Gisler, T., Rüger, H., Egelhaaf, S. U., Tschumi, J., Schurtenberger, P., & Rička, J. (1995). Mode-selective dynamic light scattering: theory versus experimental realization. *Applied Optics*, *34*(18), 3546–53. Retrieved from http://www.ncbi.nlm.nih.gov/pubmed/21052170

Goff, D. A., Buckley, E. M., Durduran, T., Wang, J., & Licht, D. J. (2010). Noninvasive Cerebral Perfusion Imaging in High-Risk Neonates. *Seminars in Perinatology*, *34*(1), 46–56. doi:10.1053/j.semperi.2009.10.005

Grant, P., Roche-Labarbe, N., & Surova, A. (2009). Increased cerebral blood volume and oxygen consumption in neonatal brain injury. *Journal of Cerebral Blood Flow and Metabolism*, *29*(10), 1704–1713. doi:10.1038/jcbfm.2009.90.Increased

Gurley, K., Shang, Y., & Yu, G. (2012). Noninvasive optical quantification of absolute blood flow, blood oxygenation, and oxygen consumption rate in exercising skeletal muscle. *Journal of Biomedical Optics*, *17*(7), 075010. doi:10.1117/1.JBO.17.7.075010

Hacke, W., Schwab, S., Horn, M., Spranger, M., De Georgia, M., & von Kummer, R. (1996). "Malignant" middle cerebral artery territory infarction: clinical course and prognostic signs. *Archives of Neurology*, *53*(4), 309–15. Retrieved from http://www.ncbi.nlm.nih.gov/pubmed/8929152

Han, S., Johansson, J., Mireles, M., Proctor, A. R., Hoffman, M. D., Vella, J. B., … Choe, R. (2015). Non-contact scanning diffuse correlation tomography system for three-dimensional blood flow imaging in a murine bone graft model. *Biomedical Optics Express*, *6*(7), 2695–712. doi:10.1364/BOE.6.002695

Haskell, R. C., Svaasand, L. O., Tsay, T. T., Feng, T. C., McAdams, M. S., & Tromberg, B. J. (1994). Boundary conditions for the diffusion equation in radiative transfer. *Journal of the Optical Society of America. A, Optics, Image Science, and Vision*, *11*(10), 2727–2741.

He, L., Lin, Y., Huang, C., Irwin, D., Szabunio, M. M., & Yu, G. (2015). Noncontact diffuse correlation tomography of human breast tumor. *Journal of Biomedical Optics*, *20*(8), 086003. doi:10.1117/1.JBO.20.8.086003

He, L., Lin, Y., Shang, Y., Shelton, B. J., & Yu, G. (2013). Using optical fibers with different modes to improve the signal-to-noise ratio of diffuse correlation spectroscopy flow-oximeter measurements. *Journal of Biomedical Optics*, *18*(3), 037001. doi:10.1117/1.JBO.18.3.037001

Hergert, W., & Wriedt, T. (2012). The Mie Theory. *The Mie Theory: Basics and Applications*, 53–71. doi:10.1007/978-3-642-28738-1

Irwin, D., Dong, L., Shang, Y., Cheng, R., Kudrimoti, M., Stevens, S. D., & Yu, G. (2011). Influences of tissue absorption and scattering on diffuse correlation spectroscopy blood flow measurements. *Biomedical Optics Express*, *2*(7), 1969–85. doi:10.1364/BOE.2.001969

Ishimaru, A. (1989). Diffusion of light in turbid material. *Applied Optics*, *28*(12), 2210–5. doi:10.1364/AO.28.002210

Jaillon, F., Li, J., Dietsche, G., Elbert, T., & Gisler, T. (2007). Activity of the human visual cortex measured non-invasively by diffusing-wave spectroscopy. *Optics Express*, *15*(11), 6643–50. Retrieved from http://www.ncbi.nlm.nih.gov/pubmed/19546974

Jain, V., Buckley, E. M., Licht, D. J., Lynch, J. M., Schwab, P. J., Naim, M. Y., … Wehrli, F. W. (2014). Cerebral oxygen metabolism in neonates with congenital heart disease quantified by MRI and optics. *Journal of Cerebral Blood Flow and Metabolism : Official Journal of the International Society of Cerebral Blood Flow and Metabolism*, *34*(3), 380–8. doi:10.1038/jcbfm.2013.214

Jöbsis, F. F. (1977). Noninvasive, infrared monitoring of cerebral and myocardial oxygen sufficiency and circulatory parameters. *Science (New York, N.Y.)*, *198*, 1264–1267. doi:10.1126/science.929199

Juul, N., Morris, G. F., Marshall, S. B., & Marshall, L. F. (2000). Intracranial hypertension and cerebral perfusion pressure: influence on neurological deterioration and outcome in severe head injury. The Executive Committee of the International Selfotel Trial. *Journal of Neurosurgery*, *92*(1), 1–6. doi:10.3171/jns.2000.92.1.0001

Keller, E., Steiner, T., Fandino, J., Schwab, S., & Hacke, W. (2002). Jugular venous oxygen saturation thresholds in trauma patients may not extrapolate to ischemic stroke patients: lessons from a preliminary study. *Journal of Neurosurgical Anesthesiology*, *14*(2), 130–6. doi:10.1097/00008506-200204000-00007

Kelly, A. F. E., Fong, A. K., C, B. N. H., & D, J. P. N. (2014). Intensive care medicine is 60 years old : the history and future of the intensive care unit, *14*(4), 376–379.

Kienle, A., & Glanzmann, T. (1999). In vivo determination of the optical properties of muscle with time-resolved reflectance using a layered model. *Physics in Medicine and Biology*, *44*(11), 2689–702. Retrieved from http://www.ncbi.nlm.nih.gov/pubmed/10588278

Kienle, A., Glanzmann, T., Wagnières, G., & Bergh, H. (1998). Investigation of two-layered turbid media with time-resolved reflectance. *Applied Optics*. Retrieved from http://www.opticsinfobase.org/abstract.cfm?&id=43824

Kim, M. N., Durduran, T., Frangos, S., Edlow, B. L., Buckley, E. M., Moss, H. E., … Kofke, W. A. (2010). Noninvasive measurement of cerebral blood flow and blood oxygenation using near-infrared and diffuse correlation spectroscopies in

critically brain-injured adults. *Neurocritical Care*, *12*(2), 173–80. doi:10.1007/s12028-009-9305-x

Kirkman, M. A., Citerio, G., & Smith, M. (2014). The intensive care management of acute ischemic stroke: An overview. *Intensive Care Medicine*, *40*(5), 640–653. doi:10.1007/s00134-014-3266-z

Langhorne, P., Dey, P., Woodman, M., Kalra, L., Wood-Dauphinee, S., Patel, N., & Hamrin, E. (2005). Is stroke unit care portable? A systematic review of the clinical trials. *Age and Ageing*, *34*(4), 324–330. doi:10.1093/ageing/afi038

Le Roux, P. (2013). Physiological monitoring of the severe traumatic brain injury patient in the intensive care unit. *Current Neurology and Neuroscience Reports*, *13*(3), 331. doi:10.1007/s11910-012-0331-2

Lee, J.-Y., Lee, M. S., Whang, K., Lee, J. M., Kim, S.-H., & Lee, S. S. (2006). Accuracy of transcranial Doppler sonography for predicting cerebral infarction in aneurysmal subarachnoid hemorrhage. *Journal of Clinical Ultrasound : JCU*, *34*(8), 380–4. doi:10.1002/jcu.20269

Li, J., Dietsche, G., Iftime, D., Skipetrov, S. E., Maret, G., Elbert, T., … Gisler, T. (2005). Noninvasive detection of functional brain activity with near-infrared diffusing-wave spectroscopy. *Journal of Biomedical Optics*, *10*(4), 44002. doi:10.1117/1.2007987

Li, J., Ninck, M., Koban, L., Elbert, T., Kissler, J., & Gisler, T. (2008). Transient functional blood flow change in the human brain measured noninvasively by diffusing-wave spectroscopy. *Optics Letters*, *33*(19), 2233–5. Retrieved from http://www.ncbi.nlm.nih.gov/pubmed/18830362

Li, T., Lin, Y., Shang, Y., He, L., Huang, C., Szabunio, M., & Yu, G. (2013). Simultaneous measurement of deep tissue blood flow and oxygenation using noncontact diffuse correlation spectroscopy flow-oximeter. *Scientific Reports*, *3*, 1358. doi:10.1038/srep01358

Li, Z., Baker, W. B., Parthasarathy, A. B., Ko, T. S., Wang, D., Schenkel, S., … Yodh, A. G. (2015). Calibration of diffuse correlation spectroscopy blood flow index with venous-occlusion diffuse optical spectroscopy in skeletal muscle. *Journal of Biomedical Optics*, *20*(12), 125005. doi:10.1117/1.JBO.20.12.125005

Lin, P.-Y., Roche-Labarbe, N., Dehaes, M., Carp, S., Fenoglio, A., Barbieri, B., … Franceschini, M. A. (2013). Non-invasive optical measurement of cerebral metabolism and hemodynamics in infants. *Journal of Visualized Experiments : JoVE*, (73), e4379. doi:10.3791/4379

Macdonald, R. L. (2014). Delayed neurological deterioration after subarachnoid haemorrhage. *Nature Reviews. Neurology*, *10*(1), 44–58. doi:10.1038/nrneurol.2013.246

Madsen, S. J., Wyss, P., Svaasand, L. O., Haskell, R. C., Tadir, Y., & Tromberg, B. J. (1994). Determination of the optical properties of the human uterus using frequency-domain photon migration and steady-state techniques. *Physics in Medicine and Biology*, *39*(8), 1191–202. doi:10.1088/0031-9155/39/8/001

Maret, G., & Wolf, P. (1987). Multiple light scattering from disordered media. The effect of Brownian motion of scatterers. *Zeitschrift Fur Physik B*, *65*, 409–413. Retrieved from http://www.springerlink.com/index/P0416778VW537K11.pdf

Matcher, S., & Cooper, C. (1994). Absolute quantification of deoxyhaemoglobin concentration in tissue near infrared spectroscopy. *Physics in Medicine and Biology*, *39*(8), 1295–312. Retrieved from http://www.ncbi.nlm.nih.gov/pubmed/15551568

Matcher, S., Cope, M., & Delpy, D. T. (1993). Use of the water absorption spectrum to quantify tissue chromophore concentration changes in near-infrared spectroscopy. *Physics in Medicine and Biology*, *39*(1), 177–96. Retrieved from http://www.ncbi.nlm.nih.gov/pubmed/7651995

Menon, C., Polin, G. M., Prabakaran, I., Hsi, A., Cheung, C., Culver, J. P., … Fraker, D. L. (2003). An Integrated Approach to Measuring Tumor Oxygen Status Using Human Melanoma Xenografts as a Model An Integrated Approach to Measuring Tumor Oxygen Status Using Human Melanoma Xenografts as a Model 1. *Cancer Research*, *63*, 7232–7240.

Mesquita, R. C., Durduran, T., Yu, G., Buckley, E. M., Kim, M. N., Zhou, C., … Yodh, A. G. (2011). Direct measurement of tissue blood flow and metabolism with diffuse optics. *Philosophical Transactions. Series A, Mathematical, Physical, and Engineering Sciences*, *369*, 4390–406. doi:10.1098/rsta.2011.0232

Mesquita, R. C., Schenkel, S. S., Minkoff, D. L., Lu, X., Favilla, C. G., Vora, P. M., … Yodh, a G. (2013). Influence of probe pressure on the diffuse correlation spectroscopy blood flow signal: extra-cerebral contributions. *Biomedical Optics Express*, *4*(7), 978–94. doi:10.1364/BOE.4.000978

Mesquita, R. C., Skuli, N., Kim, M. N., Liang, J., Schenkel, S., Majmundar, A. J., … Yodh, A. G. (2010). Hemodynamic and metabolic diffuse optical monitoring in a mouse model of hindlimb ischemia. *Biomedical Optics Express*, *1*(4), 1173–1187. doi:10.1364/BOE.1.001173

Montcel, B., Chabrier, R., & Poulet, P. (2005). Detection of cortical activation with time-resolved diffuse optical methods. *Applied Optics*, *44*(10), 1942–7. Retrieved from http://www.ncbi.nlm.nih.gov/pubmed/15813530

Moore, S., David, T., Chase, J. G., Arnold, J., & Fink, J. (2006). 3D models of blood flow in the cerebral vasculature. *Journal of Biomechanics*, *39*(8), 1454–1463. doi:10.1016/j.jbiomech.2005.04.005

Muizelaar, J. P., Ward, J. D., Marmarou, A., Newlon, P. G., & Wachi, A. (1989). Cerebral blood flow and metabolism in severely head-injured children. *Journal of Neurosurgery*, *71*, 72–76. doi:10.3171/jns.1989.71.1.0072

Narayan, R. K., Kishore, P. R., Becker, D. P., Ward, J. D., Enas, G. G., Greenberg, R. P., … Young, H. F. (1982). Intracranial pressure: to monitor or not to monitor? A review of our experience with severe head injury. *Journal of Neurosurgery*, *56*(5), 650–659. doi:10.3171/jns.1982.56.5.0650

Narotam, P. K., Morrison, J. F., & Nathoo, N. (2009). Brain tissue oxygen monitoring in traumatic brain injury and major trauma: outcome analysis of a brain tissue oxygen-directed therapy. *Journal of Neurosurgery*, *111*(4), 672–682. doi:10.3171/2009.4.JNS081150

Nicklin, S. E., Hassan, I. a-a, Wickramasinghe, Y. a, & Spencer, S. a. (2003). The light still shines, but not that brightly? The current status of perinatal near infrared spectroscopy. *Archives of Disease in Childhood. Fetal and Neonatal Edition*, *88*(4), F263–F268. doi:10.1136/fn.88.4.F263

Ninck, M., Untenberger, M., & Gisler, T. (2010). Diffusing-wave spectroscopy with dynamic contrast variation: disentangling the effects of blood flow and extravascular tissue shearing on signals from deep tissue. *Biomedical Optics Express*, *1*(5), 1502–1513. doi:10.1364/BOE.1.001502

Otite, F., Mink, S., Tan, C. O., Puri, A., Zamani, A. A., Mehregan, A., … Sorond, F. A. (2014). Impaired Cerebral Autoregulation Is Associated With Vasospasm and Delayed Cerebral Ischemia in Subarachnoid Hemorrhage. *Stroke*, *45*(3), 677–682. doi:10.1161/STROKEAHA.113.002630

Patterson, M. S. M., Chance, B., & Wilson, B. C. (1989). Time resolved reflectance and transmittance for the noninvasive measurement of tissue optical properties. *Applied Optics*, *28*(12), 2331. doi:10.1364/AO.28.002331

Pecora, R. (1972). Quasi-elastic light scattering from macromolecules. *Annual Review of Biophysics and Bioengineering*, *1*, 257–76. doi:10.1146/annurev.bb.01.060172.001353

Peeples, E. S., Mehic, E., Mourad, P. D., & Juul, S. E. (2015). Fast Doppler as a novel bedside measure of cerebral perfusion in preterm infants. *Clinical Investigation*, (August), 1–6. doi:10.1038/pr.2015.227

Pfausler, B., Beer, R., Engelhardt, K., Kemmler, G., Mohsenipour, I., Schmutzhard, E., … Johnston, R. (2004). Cell index - A new parameter for the early diagnosis of ventriculostomy (external ventricular drainage)-related ventriculitis in patients with intraventricular hemorrhage? *Acta Neurochirurgica*, *146*(5), 477–481. doi:10.1007/s00701-004-0258-8

Picciolini, O., Squarza, C., Fontana, C., Giannì, M. L., Cortinovis, I., Gangi, S., … Mosca, F. (2015). Neurodevelopmental outcome of extremely low birth weight infants at 24 months corrected age: a comparison between Griffiths and Bayley Scales. *BMC Pediatrics*, *15*, 139. doi:10.1186/s12887-015-0457-x

Pine, D. J., Weitz, D. a., Chaikin, P. M., & Herbolzheimer, E. (1988). Diffusing wave spectroscopy. *Physical Review Letters*, *60*, 1134–1137. doi:10.1103/PhysRevLett.60.1134

Pine, D., Weitz, a, Chaikin, M., & Herbolzheimer, E. (1988). Diffusing-Wave Spectroscopy. *Physical Review Letters*, *60*(12), 1134–1137. Retrieved from http://link.aps.org/doi/10.1103/PhysRevLett.60.1134

Powers, W., Grubb, R. L., Darriet, D., & Raichle, M. E. (1985). Cerebral blood flow and cerebral metabolic rate of oxygen requirements for cerebral function and viability

in humans. *Journal of Cerebral Blood Flow and Metabolism*, *5*(4), 600–8. doi:10.1038/jcbfm.1985.89

Profio, a E. (1989). Light transport in tissue. *Applied Optics*, *28*(12), 2216–2222. doi:10.1364/AO.28.002216

Ramakrishna, R., Stiefel, M., Udoteuk, J., Spiotta, A., Levine, J. M., Kofke, W. A., … LeRoux, P. (2008). Brain oxygen tension and outcome in patients with aneurysmal subarachnoid hemorrhage. *J Neurosurg*, *109*(December), 1075–1082. doi:10.3171.JNS.2008.109.12.1075

Riva, C., Ross, B., & Benedek, G. B. (1972). Laser Doppler measurements of blood flow in capillary tubes and retinal arteries. *Investigative Ophthalmology*, *11*(11), 936–944. Retrieved from http://www.ncbi.nlm.nih.gov/pubmed/4634958\nhttp://www.iovs.org/cgi/pmidlookup?view=long&pmid=4634958\nAll Papers/R/Riva et al. 1972 - Laser Doppler measurements of blood flow in capillary tubes and retinal arteries.pdf

Robertson, C. S., Valadka, A. B., Hannay, H. J., Contant, C. F., Gopinath, S. P., Cormio, M., … Grossman, R. G. (1999). Prevention of secondary ischemic insults after severe head injury. *Critical Care Medicine*, *27*(10), 2086–2095. doi:10.1097/00008506-200004000-00023

Roche-Labarbe, N., Carp, S. A., Surova, A., Patel, M., Boas, D. A., Grant, P. E., & Franceschini, M. A. (2010). Noninvasive optical measures of CBV, StO2, CBF index, and rCMRO2 in human premature neonates' brains in the first six weeks of life. *Human Brain Mapping*, *31*(3), 341–352. doi:10.1002/hbm.20868

Roche-Labarbe, N., Fenoglio, A., Aggarwal, A., Dehaes, M., Carp, S. A., Franceschini, M. A., & Grant, P. E. (2012). Near-infrared spectroscopy assessment of cerebral oxygen metabolism in the developing premature brain. *Journal of Cerebral Blood Flow & Metabolism*, *32*(3), 481–488. doi:10.1038/jcbfm.2011.145

Ropper, A. H. (1984). Brain Edema After Stroke. *Archives of Neurology*, *41*(1), 26. doi:10.1001/archneur.1984.04050130032017

Sanelli, P. C., Kishore, S., Gupta, A., Mangat, H., Rosengart, A., Kamel, H., & Segal, A. (2014). Delayed Cerebral Ischemia in Aneurysmal Subarachnoid Hemorrhage: Proposal of an Evidence-Based Combined Clinical and Imaging Reference Standard. *American Journal of Neuroradiology*, *35*(12), 2209–2214. doi:10.3174/ajnr.A3782

Sarrafzadeh, A. S., Vajkoczy, P., Bijlenga, P., & Schaller, K. (2014). Monitoring in neurointensive care - The challenge to detect delayed cerebral ischemia in high grade aneurysmal SAH. *Frontiers in Neurology*, *5 JUL*(February). doi:10.3389/fneur.2014.00134

Schmidt, J. M., Wartenberg, K. E., Fernandez, A., Claassen, J., Rincon, F., Ostapkovich, N. D., … Mayer, S. a. (2008). Frequency and clinical impact of asymptomatic cerebral infarction due to vasospasm after subarachnoid hemorrhage. *Journal of Neurosurgery*, *109*(6), 1052–1059. doi:10.3171/JNS.2008.109.12.1052

Sekhar, L., Wechsler, L., Yonas, H., Luyckx, B., & Obrist, W. D. (1988). Value of transcranial Doppler examination in the diagnosis of cerebral vasospasm after subarachnoid hemorrhage. *Neurosurgery*. Retrieved from http://journals.lww.com/neurosurgery/Abstract/1988/05000/Value_of_Transcranial_Doppler_Examination_in_the.2.aspx

Selb, J., Boas, D. a., Chan, S.-T., Evans, K. C., Buckley, E. M., & Carp, S. a. (2014). Sensitivity of near-infrared spectroscopy and diffuse correlation spectroscopy to brain hemodynamics: simulations and experimental findings during hypercapnia. *Neurophotonics*, *1*(1), 015005. doi:10.1117/1.NPh.1.1.015005

Selb, J., Stott, J. J., Franceschini, M. A., Sorensen, a G., & Boas, D. (2005). Improved sensitivity to cerebral hemodynamics during brain activation with a time-gated optical system: analytical model and experimental validation. *Journal of Biomedical Optics*, *10*(1), 11013. doi:10.1117/1.1852553

Shafi, S., Diaz-Arrastia, R., Madden, C., & Gentilello, L. (2008). Intracranial Pressure Monitoring in Brain-Injured Patients is Associated With Worsening of Survival. *The Journal of Trauma: Injury, Infection, and Critical Care*, *64*(2), 335–340. doi:10.1097/TA.0b013e31815dd017

Shang, Y., Chen, L., Toborek, M., & Yu, G. (2011). Diffuse optical monitoring of repeated cerebral ischemia in mice. *Optics Express*, *19*(21), 20301. doi:10.1364/OE.19.020301

Shang, Y., Symons, T. B., Durduran, T., Yodh, a G., & Yu, G. (2010). Effects of muscle fiber motion on diffuse correlation spectroscopy blood flow measurements during exercise. *Biomedical Optics Express*, *1*(2), 500–511. doi:10.1364/BOE.1.000500

Shaw, C.-M., Alvord, E., & Berry, R. (1959). Swelling of the Brain Following Ischemic Infarction with Arterial Occlusion. *Archives of Neurology*, *1*(2), 161–177. doi:10.1001/archneur.1959.03840020035006

Siegel, A., Marota, J. J., & Boas, D. (1999). Design and evaluation of a continuous-wave diffuse optical tomography system. *Optics Express*, *4*(8), 287. doi:10.1364/OE.4.000287

Singh, V., & Edwards, N. J. (2013). Advances in the critical care management of ischemic stroke. *Stroke Research and Treatment*, *2013*, 510481.

Skipetrov, S. E., & Maynard, R. (1996). Dynamic multiple scattering of light in multilayer turbid media. *Physics Letters, Section A: General, Atomic and Solid State Physics*, *217*(2-3), 181–185. doi:10.1016/0375-9601(96)00335-0

Sloan, M. A., Alexandrov, A. V, Tegeler, C. H., Spencer, M. P., Caplan, L. R., Feldmann, E., … Goodin, D. S. (2004). Assessment: transcranial Doppler ultrasonography: report of the Therapeutics and Technology Assessment Subcommittee of the American Academy of Neurology 100. *Neurology*, *62*(1526-632X (Electronic)), 1468–1481. doi:10.1212/WNL.62.9.1468

St Lawrence, K., Verdecchia, K., Elliott, J., Tichauer, K., Diop, M., Hoffman, L., & Lee, T. Y. (2013). Kinetic model optimization for characterizing tumour physiology by

dynamic contrast-enhanced near-infrared spectroscopy. *Physics in Medicine and Biology*, *58*(5), 1591–1604. doi:10.1088/0031-9155/58/5/1591

Staalsø, J. M., Edsen, T., Romner, B., & Olsen, N. V. (2013). Transcranial Doppler velocimetry in aneurysmal subarachnoid haemorrhage: Intra- and interobserver agreement and relation to angiographic vasospasm and mortality. *British Journal of Anaesthesia*, *110*(4), 577–585. doi:10.1093/bja/aes458

Ståhl, N., Mellergård, P., Hallström, A., Ungerstedt, U., & Nordström, C. H. (2001). Intracerebral microdialysis and bedside biochemical analysis in patients with fatal traumatic brain lesions. *Acta Anaesthesiologica Scandinavica*, *45*(8), 977–985. doi:10.1034/j.1399-6576.2001.450810.x

Steiner, L. A., & Andrews, P. J. D. (2006). Monitoring the injured brain: ICP and CBF. *British Journal of Anaesthesia*, *97*(1), 26–38. doi:10.1093/bja/ael110

Stern, M. (1975). In vivo evaluation of microcirculation by coherent light scattering. *Nature*, *254*, 56–58. doi:10.1038/254056a0

Sunar, U., Makonnen, S., Zhou, C., Durduran, T., Yu, G., Wang, H.-W., … Yodh, A. G. (2007). Hemodynamic responses to antivascular therapy and ionizing radiation assessed by diffuse optical spectroscopies. *Optics Express*, *15*(23), 15507–15516. doi:10.1364/OE.15.015507

Sunar, U., Rohrbach, D., Rigual, N., Tracy, E., Keymel, K., Cooper, M. T., … Henderson, B. H. (2010). Monitoring photobleaching and hemodynamic responses to HPPH-mediated photodynamic therapy of head and neck cancer: a case report. *Optics Express*, *18*(14), 14969. doi:10.1364/OE.18.014969

Surgeons., B. T. F. A. A. of N. S. C. of N. (2007). Acknowledgments. *Journal of Neurotrauma*, *24*(supplement 1), i–vi. doi:10.1089/neu.2007.9999

Symon, L., Branston, N. M., Strong, a J., & Hope, T. D. (1977). The concepts of thresholds of ischaemia in relation to brain structure and function. *Journal of Clinical Pathology. Supplement (Royal College of Pathologists)*, *11*, 149–154. doi:10.1136/jcp.s3-11.1.149

Tellis, G. M., Mesquita, R. C., & Yodh, A. G. (2011). Use of Diffuse Correlation Spectroscopy To Measure Brain Blood Flow Differences During Speaking and Nonspeaking Tasks for Fluent Speakers and Persons Who Stutter. *Perspectives on Fluency and Fluency Disorders*, *21*(3), 96–106. doi:10.1044/ffd21.3.96

Tichauer, K. M., Brown, D. W., Hadway, J., Lee, T.-Y., & St. Lawrence, K. (2006). Near-infrared spectroscopy measurements of cerebral blood flow and oxygen consumption following hypoxia-ischemia in newborn piglets. *Journal of Applied Physiology*, *100*(3), 850–7. doi:10.1152/japplphysiol.00830.2005

Tichauer, K. M., Elliott, J. T., Hadway, J., Lee, D. S., Lee, T.-Y., & St. Lawrence, K. (2010). Using near-infrared spectroscopy to measure cerebral metabolic rate of oxygen under multiple levels of arterial oxygenation in piglets. *Journal of Applied Physiology*, *109*(3), 878–85. doi:10.1152/japplphysiol.01432.2009

Tichauer, K. M., Hadway, J., Lee, T.-Y., & St. Lawrence, K. (2006). Measurement of cerebral oxidative metabolism with near-infrared spectroscopy: a validation study. *Journal of Cerebral Blood Flow and Metabolism*, *26*(5), 722–30. doi:10.1038/sj.jcbfm.9600230

Tisdall, M. M., & Smith, M. (2006). Cerebral microdialysis: research technique or clinical tool. *Bja*, *97*(1), 18–25. doi:10.1093/bja/ael109

Tyson, J. E., Parikh, N. A., Langer, J., Green, C., & Higgins, R. D. (2008). Intensive Care for Extreme Prematurity — Moving beyond Gestational Age. *New England Journal of Medicine*, *358*(16), 1672–1681. doi:10.1056/NEJMoa073059

Unit, S., & Collaboration, T. (2013). Organised inpatient (stroke unit) care for stroke. In P. Langhorne (Ed.), *Cochrane Database of Systematic Reviews*. Chichester, UK: John Wiley & Sons, Ltd. doi:10.1002/14651858.CD000197.pub3

Vajkoczy, P., Horn, P., Thome, C., Munch, E., & Schmiedek, P. (2003). Regional cerebral blood flow monitoring in the diagnosis of delayed ischemia following aneurysmal subarachnoid hemorrhage. *Journal of Neurosurgery*, *98*, 1227–1234. doi:10.3171/jns.2003.98.6.1227

Vergouwen, M. D. I., Ilodigwe, D., & MacDonald, R. L. (2011). Cerebral infarction after subarachnoid hemorrhage contributes to poor outcome by vasospasm-dependent and -independent effects. *Stroke*, *42*(4), 924–929. doi:10.1161/STROKEAHA.110.597914

Vergouwen, M. D. I., Vermeulen, M., van Gijn, J., Rinkel, G. J. E., Wijdicks, E. F., Muizelaar, J. P., … Roos, Y. B. W. E. M. (2010). Definition of delayed cerebral ischemia after aneurysmal subarachnoid hemorrhage as an outcome event in clinical trials and observational studies: proposal of a multidisciplinary research group. *Stroke; a Journal of Cerebral Circulation*, *41*(10), 2391–2395. doi:10.1161/STROKEAHA.110.589275

Vespa, P., Bergsneider, M., Hattori, N., Wu, H., Huang, S., Martin, N. A., … Hovda, D. A. (2005). Metabolic crisis without brain ischemia is common after traumatic brain injury: a combined microdialysis and positron emission tomography study. *Journal of Cerebral Blood Flow & Metabolism*, *25*(6), 763–774. doi:10.1038/sj.jcbfm.9600073

Wang, L. V., & Wu, H.-I. (2009). *Biomedical Optics*. Hoboken, NJ, USA: John Wiley & Sons, Inc. doi:10.1002/9780470177013

Wang, D., Parthasarathy, A. B., Baker, W. B., Gannon, K., Kavuri, V., Ko, T., … Yodh, A. G. (2016). Fast blood flow monitoring in deep tissues with real-time software correlators. *Biomedical Optics Express*, *7*(3), 776. doi:10.1364/BOE.7.000776

Washington, C. W., & Zipfel, G. J. (2011). Detection and monitoring of vasospasm and delayed cerebral ischemia: A review and assessment of the literature. *Neurocritical Care*, *15*(2), 312–317. doi:10.1007/s12028-011-9594-8

Watzman, H. H. M., Kurth, C. C. D., Montenegro, L. L. M., Rome, J., Steven, J. M., & Nicolson, S. C. (2000). Arterial and venous contributions to near-infrared cerebral oximetry. *Anesthesiology*, *93*(4), 947. doi:10.1002/star.200590022

Weir, B., Grace, M., Hansen, J., & Rothberg, C. (1978). Time course of vasospasm in man. *Journal of Neurosurgery*, *48*(2), 173–178. doi:10.3171/jns.1978.48.2.0173

White, H., & Venkatesh, B. (2008). Cerebral perfusion pressure in neurotrauma: a review. *Anesthesia and Analgesia*, *107*(3), 979–988. doi:10.1213/ane.0b013e31817e7b1a

Wray, S., Cope, M., Delpy, D. T., Wyatt, J. S., & Reynolds, E. O. (1988). Characterization of the near infrared absorption spectra of cytochrome aa3 and haemoglobin for the non-invasive monitoring of cerebral oxygenation. *Biochimica et Biophysica Acta*, *933*, 184–192. doi:10.1016/0005-2728(88)90069-2

Yodh, A., & Chance, B. (1995). Spectroscopy and Imaging with Diffusing Light. *Physics Today*, *48*(3), 34–40. doi:10.1063/1.881445

Yodh, A. G. (2009). Diffuse optics for monitoring brain hemodynamics. In *2009 Annual International Conference of the IEEE Engineering in Medicine and Biology Society* (pp. 1991–1993). IEEE. doi:10.1109/IEMBS.2009.5333424

Yu, G., Durduran, T., Lech, G., Zhou, C., Chance, B., Mohler, E. R., & Yodh, A. G. (2005). Time-dependent blood flow and oxygenation in human skeletal muscles measured with noninvasive near-infrared diffuse optical spectroscopies. *Journal of Biomedical Optics*, *10*(2), 024027. doi:10.1117/1.1884603

Yu, G., Durduran, T., Zhou, C., Wang, H.-W., Putt, M. E., Saunders, H. M., … Busch, T. M. (2005). Noninvasive monitoring of murine tumor blood flow during and after photodynamic therapy provides early assessment of therapeutic efficacy. *Clinical Cancer Research : An Official Journal of the American Association for Cancer Research*, *11*(9), 3543–3552. doi:10.1158/1078-0432.CCR-04-2582

Yu, G., Durduran, T., Zhou, C., Zhu, T. C., Finlay, J. C., Busch, T. M., … Yodh, A. G. (2006). Real-time in situ monitoring of human prostate photodynamic therapy with diffuse light. *Photochemistry and Photobiology*, *82*(5), 1279–84. doi:10.1562/2005-10-19-RA-721

Yu, G., Floyd, T. F., Durduran, T., Zhou, C., Wang, J., Detre, J. a, & Yodh, A. G. (2007). Validation of diffuse correlation spectroscopy for muscle blood flow with concurrent arterial spin labeled perfusion MRI. *Optics Express*, *15*(3), 1064–75. Retrieved from http://www.ncbi.nlm.nih.gov/pubmed/19532334

Yücel, M. A., Selb, J., Boas, D. A., Cash, S. S., & Cooper, R. J. (2014). Reducing motion artifacts for long-term clinical NIRS monitoring using collodion-fixed prism-based optical fibers. *NeuroImage*, *85*(4), 192–201. doi:10.1016/j.neuroimage.2013.06.054

Zaramella, P., Saraceni, E., Freato, F., Falcon, E., Suppiej, A., Milan, A., … Chiandetti, L. (2007). Can tissue oxygenation index (TOI) and cotside neurophysiological variables predict outcome in depressed/asphyxiated newborn infants? *Early Human Development*, *83*(8), 483–9. doi:10.1016/j.earlhumdev.2006.09.003

Zhou, C. (2007). *In Vivo Optical Imaging and Spectroscopy of Cerebral Hemodynamics*.

Zhou, C., Choe, R., Shah, N., Durduran, T., Yu, G., Durkin, A., … Yodh, A. G. (2007). Diffuse optical monitoring of blood flow and oxygenation in human breast cancer during early stages of neoadjuvant chemotherapy. *Journal of Biomedical Optics*, *12*(5), 051903. doi:10.1117/1.2798595

Zhou, C., Eucker, S. a, Durduran, T., Yu, G., Ralston, J., Friess, S. H., … Yodh, A. G. (2009). Diffuse optical monitoring of hemodynamic changes in piglet brain with closed head injury. *Journal of Biomedical Optics*, *14*(3), 034015. doi:10.1117/1.3146814

Zhou, C., Yu, G., Furuya, D., Greenberg, J., Yodh, A. G., & Durduran, T. (2006). Diffuse optical correlation tomography of cerebral blood flow during cortical spreading depression in rat brain. *Optics Express*, *14*(3), 1125–44. Retrieved from http://www.ncbi.nlm.nih.gov/pubmed/19503435

Zirak, P., Delgado-Mederos, R., Martí-Fàbregas, J., & Durduran, T. (2010). Effects of acetazolamide on the micro- and macro-vascular cerebral hemodynamics: a diffuse optical and transcranial doppler ultrasound study. *Biomedical Optics Express*, *1*(5), 1443–1459. doi:10.1364/BOE.1.001443

Chapter 2

2 Measurements of Absolute Cerebral Metabolic Rate of Oxygen by a Hybrid Optical Modality that Includes Diffuse Correlation Spectroscopy

This chapter is adapted from the paper entitled "Quantifying the cerebral metabolic rate of oxygen by combining diffuse correlation spectroscopy and time-resolved near-infrared spectroscopy" by Verdecchia K, Diop M, Lee T-Y, St. Lawrence K, published in the Journal of Biomedical Optics vol. 18(12) pp. 27007 (2013).

2.1 Introduction

Improvements in neonatal intensive care have reduced the mortality rate associated with preterm birth, but unfortunately these infants remain at a high risk of neurological complications, including learning disabilities and cerebral palsy (Behrman, 2006). Preterm infants are vulnerable to ischemic and hemorrhagic brain injury in part because of an underdeveloped cerebral vasculature, including limited or impaired autoregulation (Volpe, 1990). As a result, unstable arterial blood pressure could lead to dangerous fluctuations in cerebral blood flow (CBF). Recent studies using near-infrared spectroscopy (NIRS) to monitor cerebral blood oxygenation have reported that periods of impaired autoregulation are not uncommon in preterm infants; however, a correlation between the occurrence of impaired autoregulations and brain lesions was not observed (O'Leary et al., 2009; Soul et al., 2007; Wong et al., 2008).

Using cerebral blood oxygenation to identify critical CBF thresholds is potentially confounded by the indirect relationship between cerebral blood oxygenation and CBF, as the former also depends on the cerebral metabolic rate of oxygen ($CMRO_2$), the cerebral blood volume (CBV) and arterial oxygen saturation (J. Cooper et al., 2011). An alternative approach would be to combine NIRS with diffuse correlation spectroscopy (DCS), an emerging optical method sensitive to CBF (Boas & Yodh, 1997; Cheung, Culver, Takahashi, Greenberg, & Yodh, 2001; Durduran et al., 2010). This combination has the advantage of providing a means of monitoring both CBF and $CMRO_2$ (Durduran

et al., 2004; Roche-Labarbe et al., 2010, 2012). The latter can be determined from blood oxygenation and flow measurements and is considered a more sensitive indicator of tissue viability (Boas & Franceschini, 2011; Powers, Grubb, Darriet, & Raichle, 1985). For example, $CMRO_2$ has been shown to be more sensitive to the severity of cerebral hypoxia-ischemia than NIRS oxygenation measurements alone (Tichauer, Brown, Hadway, Lee, & St. Lawrence, 2006; Tichauer, Elliott, Hadway, Lee, & St. Lawrence, 2009). The combination of NIRS and DCS could therefore help identify clinically significant passive-pressure CBF by detecting flow fluctuations large enough to affect cerebral energy metabolism.

The purpose of this study was to demonstrate that changes in absolute $CMRO_2$ could be measured by combining NIRS and DCS. In order to quantify $CMRO_2$, techniques for measuring absolute CBF and cerebral blood oxygenation are required. In this study, relative blood flow changes measured by DCS were converted into units of CBF using a bolus-tracking time-resolved (TR) NIRS technique to measure baseline CBF (Diop, Verdecchia, Lee, & St. Lawrence, 2011). Cerebral blood oxygenation was determined from multi-wavelength TR NIRS measurements. The accuracy of the oxygenation measurements was assessed by directly measuring blood oxygenation in the sagittal sinus. The sensitivity of the hybrid approach to changes in $CMRO_2$ was investigated by manipulating cerebral metabolism in newborn piglets by altering the anesthetics and by injecting sodium cyanide, a mitochondrial inhibitor (C. Cooper et al., 1999; Tichauer, Hadway, Lee, & St. Lawrence, 2006).

2.2 Methods

2.2.1 Animal Model

This study was approved by the Animal Use Subcommittee at Western University. Experiments were carried out on newborn Duroc pigs (<3 days old). All surgical procedures were performed while piglets inhaled 3-4% isoflurane. Piglets were tracheotimized and mechanically ventilated on an oxygen/medical air mixture. Catheters were inserted into an ear vein, the left femoral artery, and superior sagittal sinus through a burr hole drilled into the skull. The ear catheter was used to inject the light absorbing

dye, indocyanine green (ICG) (Sigma-Aldrich, Missouri, US), and the different drugs used in the experiment. The femoral and sagittal sinus catheters were used to acquire blood samples in order to determine the oxygen saturation of arterial blood (SaO_2) and cerebral venous blood (SvO_2), respectively. The superior sagittal sinus primarily drains the cerebral cortex, which is the brain region interrogated by the optical probes (Scremin, Sonnenschein, & Rubinstein, 1982). The femoral line was also used to monitor heart rate (HR), blood pressure, blood gases ($paCO_2$ and paO_2), and blood glucose (BG). A 1-2 ml infusion of a 25% glucose solution was administered intravenously if glucose levels fell below 4.5 mmol/L. A heated water mattress was used to maintain rectal temperature between 37.5 and 38.5°C throughout the experiment. After surgery, the optical probes were positioned on the scalp using a custom-made probe holder with a source-detector separation of 20 mm. A separation of 10 mm between the probes from the two optical systems ensured that they interrogated roughly the same brain region. No data were acquired for at least 30 minutes following surgery to ensure the piglet was physiologically stabile. Baseline conditions were identified by blood samples revealing normal $paCO_2$ and paO_2: 38-42 mmHg and 100-170 mmHg, respectively (Reivich, 1964).

2.2.2 Experimental Procedure

Five different cerebral metabolic states were induced by manipulating the anesthetics and by injecting sodium cyanide. Following a change of condition, data acquisition was delayed by approximately 5 min to allow time for cerebral metabolism to stabilize. Under each condition, DCS was used to measure the blood flow index (BFI) and multi-wavelength TR NIRS was used to measure the oxygen saturation of cerebral tissue (ScO_2) (see instrumentation section). Blood samples (0.3-0.5 ml) were drawn from the femoral artery and the sagittal sinus to determine SaO_2 and SvO_2, by hemoximetry (ABL80 Flex Co-ox, Radiometer, Copenhagen, DK). The DCS and TR NIRS data were acquired in three blocks during each condition (Figure 2-1). In each block, 96 TR NIRS measurements were acquired with an integration time of 1 s and 20 DCS measurements were acquired with an integration time of 30 s. All data sets for each condition were acquired within approximately 45 minutes.

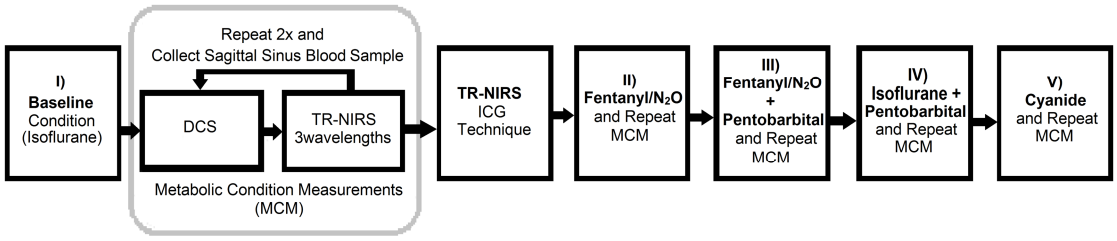

Figure 2-1: Diagram of the experimental protocol

An experimental protocol diagram showing the induced metabolic conditions in chronological order with the sequence of measurements acquired at each condition. The solid boxes are distinctive steps, whereas the dotted box is recurring for each induced condition numbered I-V.

Initial baseline measurements were acquired under 1.75-2% isoflurane mixed with a combination of medical air and oxygen to maintain normal paO_2. In addition to the standard data acquisition protocol, CBF was measured by a dynamic contrast-enhanced TR NIR method using ICG as an intravascular contrast agent (Brown et al., 2002). This method requires injecting an intravenous bolus of ICG (0.01 mg/kg), followed by measuring the time-varying concentration of ICG in arterial blood and the brain. The brain ICG concentration curve was determined by acquiring a series of TR NIR measurements at a sampling rate of 400 ms. The arterial concentration curve was measured using a pulse dye densitometer (DDG 2001, Nihon Kohden, Tokyo, JP) attached to a foot. Three successive sets of ICG data were acquired to improve the precision of the baseline CBF measurement. Successive ICG injections were separated by 10 min to allow time for ICG clearance from the previous injection. The average value of CBF was used to convert subsequent DCS BFI measurements into units of CBF (Diop et al., 2011).

Following the baseline measurements, TR NIRS and DCS were used to measure ScO_2 and the BFI, respectively, under four conditions. First, $CMRO_2$ was increased by discontinuing isoflurane and starting an intravenous infusion of fentanyl (0.02 mg/kg/h) combined with inhalation of 70% nitrous oxide (N_2O). Second, the barbiturate pentobarbital (5 mg/kg) was injected intravenously to decrease $CMRO_2$. Cerebral energy metabolism was further reduced by switching off the fentanyl/N_2O mixture, returning the piglet to isoflurane (1.75-2%), and administering another 5 mg/kg of pentobarbital. For the final condition, sodium cyanide was injected intravenously at a dose of 5 mg/kg. This

non-lethal dosage of cyanide is insufficient to completely inhibit mitochondrial function (Sakamoto et al., 2001); however, it is sufficient to reduce mitochondrial respiration (C. Cooper et al., 1999).

2.2.3 Instrumentation

2.2.3.1 Time-Resolved NIRS System

The TR instrument for the ScO_2 measurements consisted of three picosecond diode lasers emitting at 760, 802 and 830 nm (LDH-P-C-810, PicoQuant, Berlin, DE). The output and pulse repetition rate of each laser were set to 1.4 mW and 29.3 MHz, respectively. A variable neutral density filter (NDC-50-4M, Thorlabs, Newton, New Jersey, US) was placed in front of each laser to adjust the intensity of the beam before the light was coupled into a multimode fiber (emission probe: N.A. = 0.22, core = 400 μm, 4.7 mm outer diameter; Fiberoptics Technology, Pomfret, Connecticut, US). Fibers of different lengths, forming a bundle, were used to provide time multiplexing (Contini et al., 2006). For the ICG bolus-tracking measurements, only the 802 nm laser was used at a repetition rate of 80 MHz to optimize the signal-to-noise ratio (SNR) (Diop, Tichauer, Elliott, Migueis, & Lee, 2010).

Reflected light from the head was collected with a 1.5 m long multimode fiber placed 20 mm from the emission fiber bundle on the piglet's intact head. The collected photons were then sent to a Peltier-cooled photomultiplier tube (PMT) (PMC-100, Becker & Hickl, Berlin, DE), coupled to a time-correlated single photon counting module (SPC-134, Becker & Hickl, Berlin, DE). Temporal point spread functions (TPSFs) were computed by synchronizing the photon detection with the laser pulse trigger provided by the driver (PDL 828, PicoQuant, Berlin, DE). Each TPSF was acquired for one second for the oxygenation measurements and 400 ms for the ICG bolus-tracking method. Temporal dispersion caused by the system was corrected for by measuring the instrument response function (IRF) (Diop, Tichauer, Elliott, Migueis, Lee, et al., 2010). To avoid artifacts such as instrument temporal drift, the TR NIRS system was allowed a 1.5 h warm up delay period prior to the experiment (Diop, Tichauer, Elliott, Migueis, & Lee, 2010; Ntziachristos & Chance, 2001).

2.2.3.2 Diffuse Correlation Spectroscopy

The DCS light source was a continuous-wave laser emitting at 785 nm (DL785-100-S, CrystalLaser, Nevada, US) with a maximum output power of 100 mW and a coherence length greater than 5 m. Similar to the time-resolved setup, the laser beam was first attenuated by a variable neutral density filter (NDC-50-4M, Thorlabs, New Jersey, US) and then coupled into an emission fiber (emission probe: N.A. = 0.22, core = 400 µm, 4.7 mm outer diameter; Fiberoptics Technology, Connecticut, US). Photons scattered from tissue were detected at a distance of 20 mm away from the emission probe using a 4-m single-mode fiber (SMF-28e+, N.A. = 0.14, core = 125 µm, single-mode cutoff wavelength at 1260 nm). Since the detection fiber is a few-mode fiber at the laser emission wavelength, the fiber was wrapped into a 15 cm coil to attenuate the higher-order modes by converting them into non-propagating modes (Dietsche et al., 2007; Diop et al., 2011; Gisler et al., 1995). Photons were detected by a single photon counting module (SPCM-AQR-15-FC, PerkinElmer Canada Inc, Quebec, CA). The output from the detector was sent to a correlator board (DPC-230, Becker & Hickl, Berlin, DE) to compute the normalized intensity autocorrelation function.

2.2.4 Data Analysis

2.2.4.1 Measuring Cerebral Oxygen Saturation by TR NIRS

Brain tissue optical properties (i.e. the absorption and reduced scattering coefficients, μ_a and μ_s', respectively) were quantified using the solution to the diffusion approximation for a semi-infinite turbid medium with extended boundary conditions (Kienle & Patterson, 1997). The three sets of TPSFs collected at each condition were averaged together and were fit by the theoretical model convolved with the measured IRF (Ntziachristos & Chance, 2001). Initial values for μ_a, μ_s', and an amplitude scaling factor were obtained by analyzing the baseline data with a three-parameter non-linear fitting routine (Diop, Tichauer, Elliott, Migueis, Lee, et al., 2010). The amplitude term was included in the fitting to take into account variations in laser power, detection gain and coupling efficiency (Diop, Tichauer, Elliott, Migueis, Lee, et al., 2010; Ntziachristos & Chance, 2001). To improve the stability of the fitting algorithm, the TPSFs were analyzed for each

metabolic condition using only μ_a as a fitting parameter; μ_s' and the amplitude scaling factor were fixed to the values retrieved from the three-parameter fit at baseline. This approach was reasonable since the metabolic changes only affect blood oxygenation and not tissue scattering properties. However, in more extreme conditions that could also alter light scattering, such as large changes in the total hemoglobin concentration (Paunescu et al., 2001), μ_s' could be included as a fitting parameter. The concentrations of oxy- and deoxy-hemoglobin ($[HbO_2]$ and [Hb], respectively) were derived from the measured μ_a values using the known wavelength-dependent extinction coefficients and assuming a cerebral water content of 85% for neonatal pig (Holland, Haas, Norman, Brant-Zawadzki, & Newton, 1986). Cerebral oxygen saturation, ScO_2, was defined as:

$$ScO_2 = \frac{[HbO_2]}{[HbO_2]+[Hb]} \tag{2.1}$$

2.2.4.2 Measuring Absolute CBF by TR NIRS

The methodology underlying the TR NIRS bolus-tracking technique for quantifying CBF, which is used extensively with imaging modalities such as magnetic resonance imaging and computed tomography (Wintermark et al., 2005), assumes that the microvasculature can be modeled as a linear time-invariant system. For this application, linearity means that the contrast agent concentration in brain tissue is linearly proportional to the concentration in arterial blood, and time-invariance implies that the hemodynamic properties must remain constant during the acquisition period. Under these assumptions, the time-varying concentration of ICG in tissue, $C_t(t)$, is related to the arterial blood ICG concentration curve, $C_a(t)$, by the convolution operator:

$$C_t(t) = CBF_{TR} \int_0^\infty C_a(t-u)R(u)\,du \tag{2.2}$$

where CBF_{TR} denotes the CBF measurement obtained by the TR NIRS method and R(t) is the impulse residue function, which represents the fraction of ICG in the tissue at time t following an idealized unit impulse injection at t = 0 (Zierler, 1965). $C_t(t)$ is determined from change in μ_a due to the passage of ICG through the cerebral microvasculature and $C_a(t)$ was measured by the DDG as outlined in Section 2.2 (Diop, Tichauer, Elliott, Migueis, Lee, et al., 2010). The flow-scaled impulse residue function, $CBF_{TR} \bullet R(t)$, was

extracted from $C_a(t)$ and $C_t(t)$ by performing a deconvolution and its initial height equals CBF_{TR}, since by definition R(0) = 1 (Brown et al., 2002).

2.2.4.3 Measuring Changes in CBF and $CMRO_2$ by TR NIRS

The DCS data from each cerebral metabolic condition were analyzed by the solution to the correlation diffusion equation for a semi-infinite homogeneous medium assuming Brownian motion of scatterers (Boas, Campbell, & Yodh, 1995; Boas & Yodh, 1997; Cheung et al., 2001). The model was fit to the normalized intensity autocorrelation function (g_2) using the μ_a and μ_s' values obtained by TR NIRS. The fitting parameters were a scaled diffusion coefficient, which is referred to as the BFI, and a coherence factor (β) (Diop et al., 2011). The change in the BFI at a given condition relative to baseline, denoted rCBF, is given by:

$$\mathrm{rCBF} = \frac{\mathrm{BFI_{condition}} - \mathrm{BFI_{baseline}}}{\mathrm{BFI_{baseline}}} \tag{3.3}$$

The BFI can be converted into units of CBF (ml/100g/min) using the baseline CBF measurement determined by the TR NIRS bolus-tracking method:

$$\mathrm{CBF} = \mathrm{CBF_{TR}} \cdot (1 + \mathrm{rCBF}) \tag{3.4}$$

The $CMRO_2$ (ml O_2/100g/min) for each metabolic state was determined by conservation of mass (i.e. the Fick principle), which assumes that the amount of oxygen consumed in the tissue is equal to the arteriovenous oxygen difference (Siesjo, 1978):

$$\mathrm{CMRO_2} = \mathrm{CBF} \cdot \mathrm{K} \cdot [\mathrm{tHb}] \cdot (\mathrm{SaO_2} - \mathrm{SvO_2}) \tag{3.5}$$

where, SaO_2 and SvO_2 are the arterial and venous oxygen saturations, respectively, K is the oxygen carrying capacity of hemoglobin (1.39 ml of O_2 per g of Hb) (Dominguez de Villota, Ruiz Carmona, Rubio, & de Andrés, 1981), and [tHb] is the total hemoglobin concentration. In these experiments, SaO_2 was measured by pulse oximetry, [tHb] was determined from the average of two baseline arterial blood samples and CBF was determined from the calibrated DCS blood flow measurements. The remaining parameter SvO_2 was determined directly from the sagittal-sinus blood samples and also from the TR

NIRS ScO_2 measurements. Equation 3.5 neglects the contribution of dissolved oxygen in plasma, which is reasonable at normal paO_2 values (Brown, Hadway, & Lee, 2003; Elwell et al., 2005). For TR NIRS, SvO_2 was determined from ScO_2 by assuming the cerebral blood volume is comprised of a known venous volume fraction (f_v) since ScO_2 represents the average cerebral blood oxygenation:

$$SvO_2 = \frac{ScO_2 - (1 - f_v)SaO_2}{f_v} \tag{3.6}$$

For this study f_v was set to 0.75 (Brun, Moen, & Borch, 1997; Ijichi et al., 2005; Mchedlishvili, 1986; Watzman et al., 2000) and using Equation 3.6, the Fick principle for the optical measurements is given by:

$$CMRO_2 = \frac{CBF \cdot K \cdot [tHb]}{f_v} \cdot (SaO_2 - ScO_2) \tag{3.7}$$

2.2.5 Statistical Analysis

Statistical analyses were conducted using SPSS 20.0 (SPSS, Chicago, IL). A repeated measures analysis of variance (ANOVA) was used to identify significant differences in SvO_2 and $CMRO_2$ between metabolic conditions and between the NIRS and blood-sampling methods. Bland-Altman analysis was used to compare corresponding $CMRO_2$ measurements from the two methods (Altman & Bland, 1983). Post-hoc analyses were conducted to identify significant differences at each condition, with respect to baseline values, for all measured parameters. Statistical significance was defined as $p < 0.05$ and all data are presented as mean ± standard error of the mean (SEM) unless otherwise noted. In one animal, measurements were not acquired during the fentanyl/N_2O-pentobarbital condition, which was corrected for by using the Missing Value Analysis (MVA) regression algorithm (Graham, 2009).

2.2.6 Error Analysis

A Monte Carlo type approach was conducted to investigate how errors in the baseline parameters would affect subsequent μ_a measurements from the one-parameter fitting routine. First, a theoretical TPSF was generated using the solution to the diffusion approximation for a semi-infinite homogeneous medium and a set of typical experimental

values of the scaling amplitude, μ_a and μ_s' (8000, 0.255 cm^{-1} and 8.62 cm^{-1}, respectively) (Kienle & Patterson, 1997). The simulated TPSF was convolved with an experimental IRF and Poisson noise added to reflect typical experimental data. The noisy TPSF was analyzed by the same non-linear fitting routine used with the experimental data to generate best-fit estimates of the baseline parameters. Next, another noisy TPSF was generated using the initial input values, and a one-parameter fit performed to extract an estimate μ_a. In this step the values of the amplitude factor and μ_s' were set to the estimates from three-parameter fit. The entire procedure was repeated 5000 times to generate a distribution of best-fit values for each fitting parameter.

To determine the error in $CMRO_2$ due to uncertainties in the two parameters measured under each condition (i.e. BFI and ScO_2), the SEM of each parameter was determined from the series of measurements acquired at baseline (i.e. 60 and 288 measurements for BFI and ScO_2, respectively). A repeated measures ANOVA was used to determine the precision of the baseline CBF values measured by the TR NIRS bolus-tracking method.

2.3 Results

A total of 12 piglets were studied; however, 3 were excluded because the sagittal sinus was inadvertently punctured during the insertion of the catheter. A puncture caused blood to leak into the cerebral spinal fluid, resulting in erroneous NIRS measurements of [HbO_2] and [Hb] (Tichauer, Hadway, et al., 2006). One additional experiment was excluded due to technical errors with the TR NIRS system, which results in incomplete TPSFs. The average physiological parameters at each metabolic condition from the 8 successful experiments (3 male, 5 female, mean weight = 1.62 ± 0.09 kg, mean age = 1.88 ± 0.35 days) are given in Table 2-1.

Table 2-1: Physiological parameters during different cerebral metabolic levels

Physiological Parameter	Baseline	Fentanyl/N_2O	Fentanyl/N_2O + Pentobarbital	Pentobarbital	Cyanide
Temperature (°C)	37.8 ± 0.2	37.9 ± 0.1	37.9 ± 0.2	37.4 ± 0.2	37 ± 0.2*
pH	7.47 ± 0.02	7.46 ± 0.02	7.46 ± 0.01	7.46 ± 0.01	7.35 ± 0.02*
$paCO_2$ (mm Hg)	40.1 ± 0.4	39.6 ± 0.8	38.7 ± 0.7	39.8 ± 0.6	43.3 ± 2.1
paO_2 (mm Hg)	124 ± 8	72 ± 5*	76 ± 5*	97 ± 8	135 ± 22
MAP (mm Hg)	42 ± 2	69 ± 2*	82 ± 4*	35 ± 3	27 ± 2*
HR (min^{-1})	157 ± 9	241 ± 12*	250 ± 14*	165 ± 11	176 ± 7

pH = arterial pH; $paCO_2$ = partial pressure of carbon dioxide in the blood; paO_2 = partial pressure of oxygen in the blood; MAP = mean arterial blood pressure; HR = heart rate
* $p<0.05$ compared to parameter value under baseline conditions.
Average ± SEM

Of all the measured parameters, only $paCO_2$ showed no significant differences between conditions. Blood pH and rectal temperature were significantly different after injecting sodium cyanide due to the systemic effect of the drug on metabolism. Significant differences in paO_2 were found under the two conditions involving fentanyl/N_2O, which can be explained by a reduction in the inhaled oxygen fraction during 70% N_2O inhalation. Both HR and MAP showed general changes with the different anesthetics as expected (Siesjo, 1978). The average [tHb] measured under baseline conditions from the hemoximeter was 8.6 ± 0.8 g/dl. The tissue optical properties measured under baseline conditions at 760, 802 and 830 nm, were 7.99 ± 0.47, 8.63 ± 0.59, and 8.55 ± 0.86 cm^{-1} for μ_s' and 0.251 ± 0.016, 0.240 ± 0.012, and 0.248 ± 0.009 cm^{-1} for μ_a, respectively.

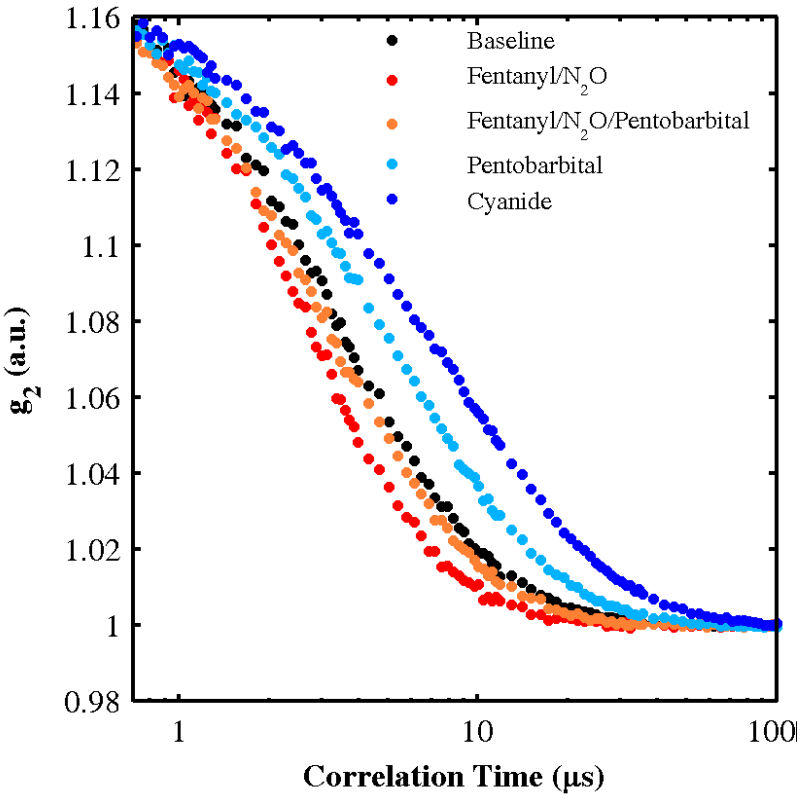

Figure 2-2: Measured DCS decay curves during various levels of cerebral metabolism

A sample of DCS decay curves taken from an experiment collected with a sampling time of 30 seconds and average count rate of 441 ± 17 kHz. Each curve shown was obtained from the same piglet at a different induced metabolic condition. The steeper the decay curve the larger the BFI retrieved and ultimately the faster CBF.

Figure 2-2 shows a sample of DCS intensity autocorrelation curves collected from each induced metabolic condition during a single experiment. A steeper DCS decay curve is represented by a larger BFI value, indicating faster blood flow. Typical arterial and brain ICG concentration curves obtained with the DDG and TR NIRS, respectively, are shown in Figure 2-3. The derived baseline CBF value obtained from the ICG data sets were used to calibrate all subsequent BFI values obtained by DCS. The measured CBF values obtained from the dynamic contrast-enhanced technique ranged from 19 to 50 ml/100g/min with an average of 32 +/- 4 ml/100g/min.

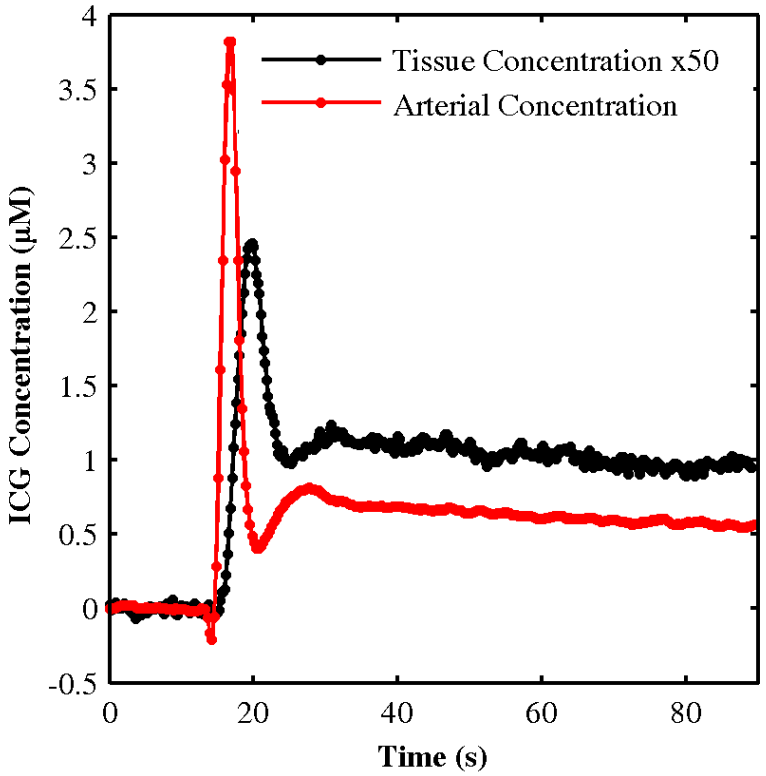

Figure 2-3: Dynamic contrast-enhanced arterial/tissue time-course curves of ICG

A sample of raw data showing a tissue and an arterial curve measured during the ICG bolus tracking experiment. The black curve represents the tissue curve measured with the TR NIRS technique whereas the red curve is the arterial curve obtained from the DDG.

Significant differences were observed in all the BFI values listed in Table 2-2 compared to baseline, except when pentobarbital was injected while under fentanyl/N_2O anesthesia. No statistical significant differences were observed between conditions for the retrieved baseline β value of 0.157 ± 0.001 which was also in agreement with the measured value obtained by Diop et al. (Diop et al., 2011). No significant differences were observed in SaO_2 at any of the conditions. A repeated measures ANOVA showed a significant overall effect by condition for SvO_2 [$F_{3,36} = 8.596$, Power > 0.99, $p<0.01$], but there was no significant effect by technique [$F_{1,14} = 0.007$, $p>0.9$]. Similarly, there was a significant effect by condition for $CMRO_2$ [$F_{3,36} = 59.707$, Power > 0.99, $p<0.01$], but no significant effect by technique [$F_{1,14} = 0.014$, $p>0.9$]. These results indicate that the various conditions altered cerebral energy metabolism, but there were no significant differences in the SvO_2 and $CMRO_2$ measurements between the sagittal sinus blood measurements and the DCS/NIRS method.

Table 2-2: NIRS and blood sample measurements

Parameter	Baseline	Fentanyl/N_2O	Fentanyl/N_2O + Pentobarbital	Pentobarbital	Cyanide
BFI (cm^2/s) x 10^9	61 ± 6	92 ± 10*	62 ± 6	30 ± 5*	28 ± 4*
SaO_2 (%)	99.9 ± 0.1	98.8 ± 0.7	98.7 ± 0.7	99.7 ± 0.6	95.8 ± 2.3
ScO_2 (%)	69 ± 2	65 ± 3	61 ± 2	57 ± 3*	59 ± 4
SvO_2 – Blood (%)	62 ± 5	55 ± 5	41 ± 5**	42 ± 6**	46 ± 8**
SvO_2 – NIRS (%)	58 ± 3	54 ± 4	48 ± 3**	42 ± 4**	46 ± 5**
$CMRO_2$ – Blood (ml O_2/100g/min)	1.31 ± 0.21	2.25 ± 0.25**	2.01 ± 0.22	0.99 ± 0.18	0.76 ± 0.15**
$CMRO_2$ – NIRS (ml O_2/100g/min)	1.45 ± 0.18	2.41 ± 0.32**	1.81 ± 0.21	0.99 ± 0.17	0.80 ± 0.15**

BFI = blood flow index; SaO_2 = saturated arterial oxygen; ScO_2 = saturated cerebral oxygen; SvO_2 = saturated venous oxygen; NIRS = near-infrared spectroscopy; $CMRO_2$ = cerebral metabolic rate of oxygen
* p<0.05 compared to parameter value under baseline conditions.
** p<0.05 compared to parameter value under baseline conditions for both techniques combined.
Average ± SEM

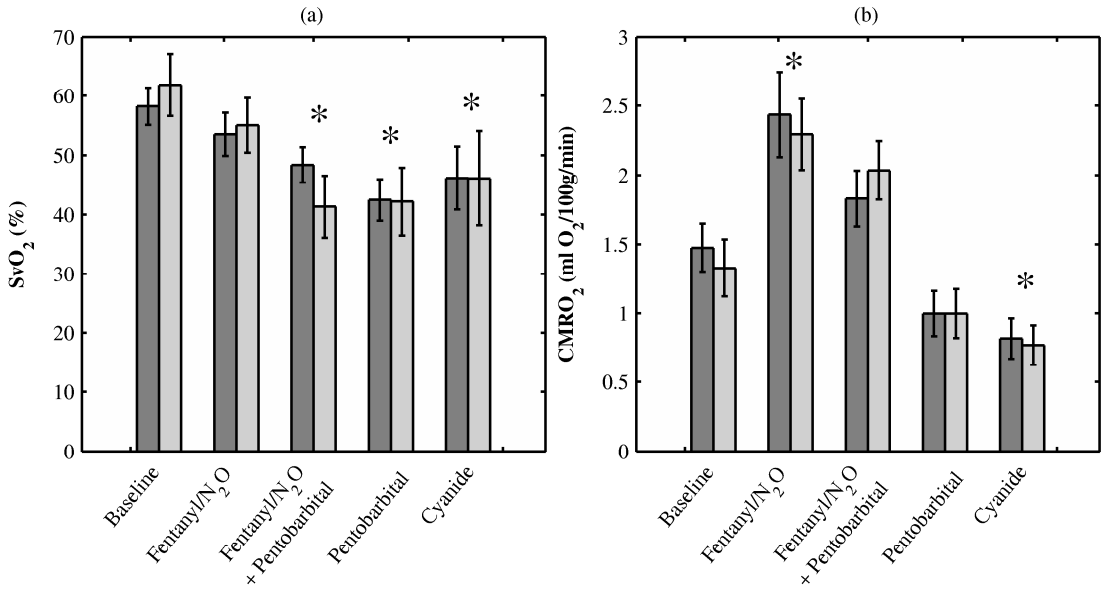

Figure 2-4: Mean values of SvO_2 and $CMRO_2$ after intake of various anesthetics/drugs

Average SvO_2 and $CMRO_2$ values at each induced condition comparing both techniques. The darker grey bars represent the NIRS technique, the lighter grey bars represent the blood oxygen sample method, and the error bars are standard error of the mean. Here * indicates p<0.05 compared to the parameter value under baseline conditions for both techniques combined.

Figure 2-4 illustrates the average SvO_2 and $CMRO_2$ measurements obtained from the blood sample and DCS/TR-NIRS techniques under the different conditions. Measurements were obtained over a range from 25 to 70 % for SvO_2 and from 0.3 to 4 ml O_2/100g/min for $CMRO_2$. A Bland-Altman plot of the difference between individual $CMRO_2$ measurements from the two techniques is shown in Figure 2-5. The mean difference was 0.027 ml O_2/100g/min with limits of agreement (i.e. 95% boundaries) of 0.861 and -0.807 ml O_2/100g/min.

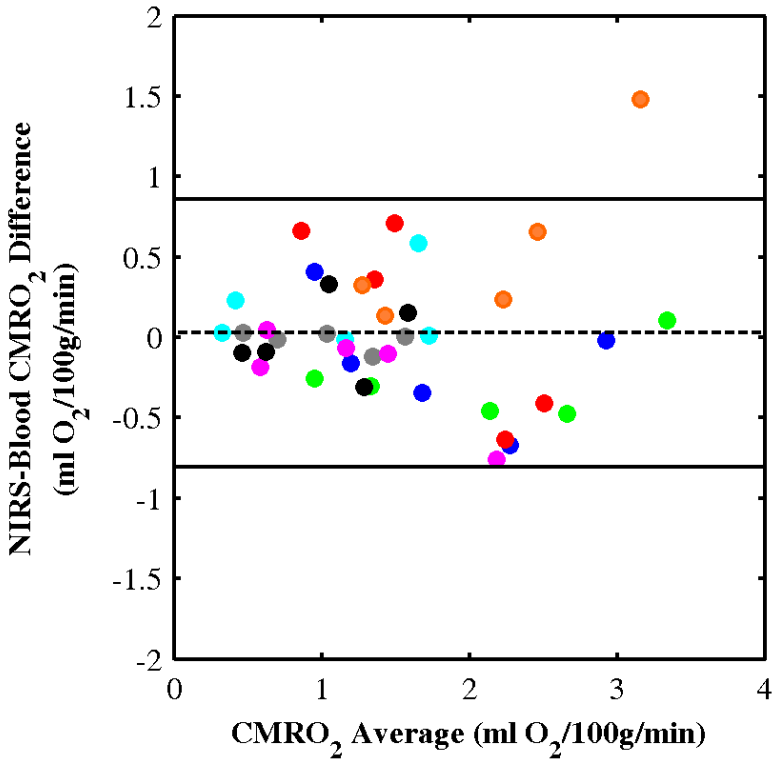

Figure 2-5: Bland-Altman analysis of $CMRO_2$

A Bland-Altman plot demonstrating the difference between NIRS and blood oxygen sample $CMRO_2$ measurements plotted against the average. Each colour represents a different piglet. The dotted line represents the average difference between the two techniques; 0.027 ml O_2/100g/min. The solid lines are the bias lines which represent the region boundaries for which 95% of the differences lie within; 0.027 ± 0.834 ml O_2/100g/min.

Figure 2-6 shows the predicted relationship between errors in the baseline optical properties to the errors in the amplitude factor as determined from the Monte Carlo simulations. The figure demonstrates that at typical experimental noise levels, μ_s' and μ_a were relatively insensitive to errors in the amplitude factor. For example, the error in either μ_s' or μ_a was only 6% in the extreme case of a 30% error in the amplitude factor.

From the Monte Carlo simulations, the coefficient of variation of μ_a for the one-parameter fitting routine was 1.7%. The small magnitude of this error was also reflected in the SEM of ScO_2 (0.1%) determined from the series of baseline measurements. Similarly, the SEM of the baseline BFI was 2%. The repeat measurements of absolute CBF from the bolus tracking method indicated that this was the greatest source of error with an estimated precision of 11.7%.

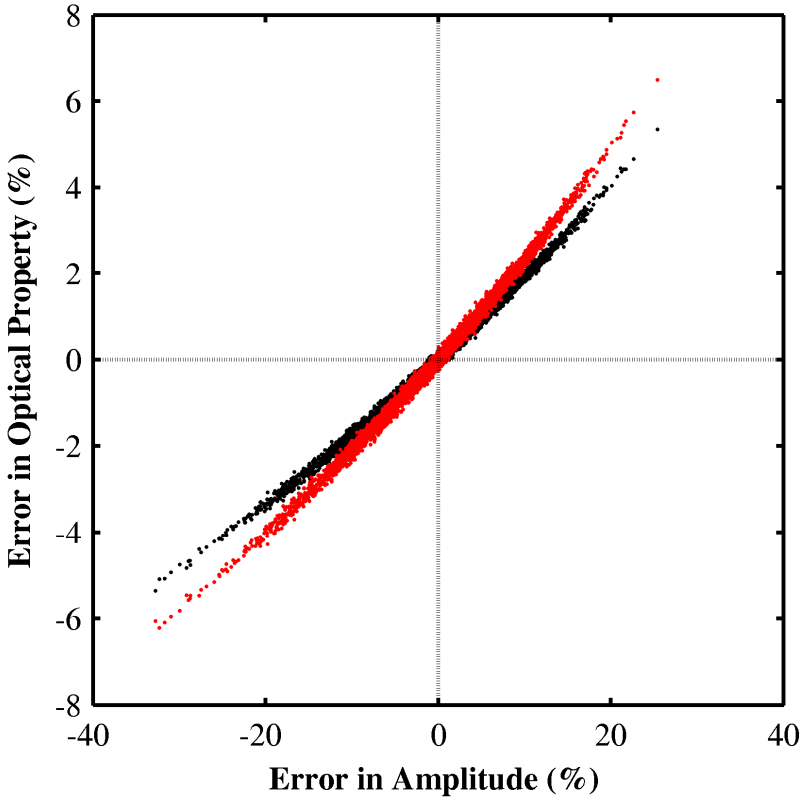

Figure 2-6: An error analysis of a three-parameter fit (μ_a, μ_s', and amplitude factor) of the diffusion approximation to TR NIRS data

An error analysis comparing the effects of noisy experimental data on a three parameter fit (μ_a, μ_s', and amplitude factor) from the diffusion approximation. Black represents μ_a and red represents μ_s', while each data point represents the error in optical properties corresponding to the error in the amplitude factor from the three parameter fit. The generated noise for 5000 simulated TPSFs had an average variance of 16.41 ± 0.05.

2.4 Discussion

The main finding of this study was that changes in absolute $CMRO_2$ could be measured by combining two near-infrared techniques: DCS and TR NIRS. This was accomplished by combining quantitative CBF and SvO_2 measurements obtained by a previously

validated DCS/TR-NIRS approach and multi-wavelength TR NIRS, respectively. The accuracy of the SvO_2 measurements was verified by comparison to direct measurements of cerebral blood oxygenation obtained from sagittal sinus blood samples. CBF, SvO_2 and $CMRO_2$ were measured over a metabolic range from approximately 0.3 to 4 ml O_2/100g/min with no evidence of any level-dependent bias in either the SvO_2 or $CMRO_2$ measurements (Figure 2-4 and Figure 2-5). DCS and NIRS have been combined previously to measure relative changes in $CMRO_2$ (Durduran et al., 2004, 2010; Roche-Labarbe et al., 2010, 2012; Zirak, Delgado-Mederos, Martí-Fàbregas, & Durduran, 2010); however, this is the first study to use this combination to quantify $CMRO_2$. The success of this combined optical approach ultimately depends on the accuracy of the underlying CBF and ScO_2 measurements. A number of studies have demonstrated the ability of DCS to track relative CBF (Buckley, Cook, Durduran, & Kim, 2009; Carp, Dai, Boas, Franceschini, & Kim, 2010; Diop et al., 2011; Kim et al., 2010; Zhou et al., 2009). In particular, Zhou et al., reported a strong correlation between changes in CBF measured by DCS compared to those measured by fluorescent microspheres in newborn piglets (Zhou et al., 2009). Similarly, we previously reported a strong correlation between CBF measurements obtained by the bolus-tracking TR NIRS technique and the BFI determined from DCS ($R^2 = 0.93$) (Diop et al., 2011).

In our previous study, a single pulsed laser was used to measure the absorption changes caused by the flow of ICG through brain tissue (Brown et al., 2002). Determining [HbO_2] and [Hb], and thereby ScO_2, requires measuring the tissue optical properties at multiple wavelengths. For this purpose, the TR system was expanded to three pulsed lasers, and time multiplexing was used to acquire the corresponding three TPSFs within the same time window (Contini et al., 2006). The disadvantage of this approach is a lower count rate per channel due to the reduced pulse repetition rate (29.3 compared to 80 MHz); however, for steady-state oxygenation measurements this was not a concern as the SNR can be improved by increasing the integration time. To quantify the wavelength-dependent μ_a and μ_s' values, the IRF was measured for each laser at similar count rates to those obtained experimentally. Temporal drift and variations in the laser pulse width (i.e. jitter) are potential sources of error when measuring tissue optical properties by TR NIRS (Ntziachristos & Chance, 2001). To minimize the former, every

experiment was preceded by a 1.5 h delay to allow sufficient time for the TR NIRS system to stabilize in order to avoid instrument drift during the course of an experiment (Diop, Tichauer, Elliott, Migueis, & Lee, 2010). The results displayed in Figure 2-6 indicate that the baseline μ_a and μ_s' values could be determined with reasonable accuracy even if there were large fluctuations in the amplitude factor, such as due to jitter. A possible improvement to the system would be to correct for both drift and jitter by acquiring reference data throughout the experiment (Tichauer et al., 2011).

The precision of $CMRO_2$ will depend on the uncertainties in the baseline optical properties, CBF and ScO_2. The Monte Carlo simulations demonstrated that the uncertainties in the optical properties were small for noise levels typical of the experimental TPSFs and had little effect on subsequent μ_a values determined from the one-parameter fitting routine. These predictions were in good agreement with the SEM of ScO_2 (0.1%) determined from the series of TPSFs acquired during the 5-min baseline period. Errors in CBF determined by the calibrated DCS approach will depend on the precision of both the baseline CBF determined by the bolus-tracking method and the relative BFI obtained by DCS. From repeat bolus injections at baseline, the precision of the former was estimated to be 11.7%, which is similar to the value determined previously (9.7%) with a continuous-wave NIRS system (Brown et al., 2002). In these experiments, the SEM of the BFI was less than 2% due to the large number of acquisitions obtained in each condition. A variability of less than 5% would still have been achieved if the acquisition time had been reduced to 5 min (i.e. 10 measurements). Maintaining the same precision at shorter acquisitions would require increasing the number of detectors (Buckley et al., 2009; Dietsche et al., 2007), as only a single SPCM was used to acquire the DCS data in these experiments. In addition to the uncertainties in the measurements parameters, the accuracy of the $CMRO_2$ measurements will depend on the assumed value of the cerebral venous blood volume fraction (f_v). The need to assume a value is a common limitation with $CMRO_2$ measurements obtained by NIRS and positron emission tomography (Elwell et al., 2005; Mintun, Raichle, Martin, & Herscovitch, 1984; Tichauer, Hadway, et al., 2006). The good agreement between the NIRS $CMRO_2$ measurements and the values derived from sagittal-sinus blood samples

(Figure 2-5) indicate that the assumed value of 75% is reasonable. However, any variation in f_v across animals or subjects will clearly reduce the accuracy of the measurements. It may be possible to circumvent this potential source of error by using NIRS spiroximetry to measure venous oxygen saturation (Franceschini et al., 2002).

The retrieved μ_s' values at baseline were similar with Diop et al. and Ijichi et al. (Diop et al., 2011; Ijichi et al., 2005). However, the average μ_a at 802 nm was greater than the values given in the two previous studies: 0.2 ± 0.009 cm^{-1} (Diop et al., 2011) and 0.189 ± 0.005 (Ijichi et al., 2005). The cause of this difference is uncertain; however, the average ScO_2 value (69 ± 2 %) was similar to baseline values previously reported in piglets (Fantini et al., 1999; Kurth, McCann, Wu, Miles, & Loepke, 2009; Kusaka et al., 2002; Springett, Newman, Cope, & Delpy, 2000). In addition, the SvO_2 values determined from the absorption changes at the different metabolic conditions ranging from 25 to 70% were in good agreement with the corresponding SvO_2 values measured directly from sagittal sinus blood samples (Table 2-2, Figure 2-4). Both sets displayed the same trend in venous oxygenation as cerebral metabolism was initially increased under fentanyl/N_2O anesthesia and subsequently decreased with successive injections of pentobarbital.

The overall agreement between $CMRO_2$ measurements derived from TR NIRS and sagittal sinus SvO_2 values is similar to our previous validation study, which was conducted using newborn piglets, but involved a broadband CW NIRS system (Tichauer, Hadway, et al., 2006). In that study, the mean difference between the two techniques was 0.006 ml O_2/100g/min and the 95% confidence interval was ± 0.74 ml O_2/100g/min. The latter is slightly smaller than the boundaries shown in Figure 2-5. However, this difference can be explained by the outlier that had an average $CMRO_2$ difference greater than the 95% confidence interval. Removing this point reduced the range to ± 0.704 ml O_2/100g/min, in excellent agreement with the previous results. It is interesting that the overall trends reported in the two studies were in good agreement considering the different approaches used to quantify cerebral blood oxygenation. The CW NIRS spectral data from the previous study were characterized by second derivative spectroscopy, which can only estimate [Hb] and not [HbO_2] since the latter has no definitive features in

the derivative spectrum (Matcher, Cope, & Delpy, 1993). Consequently, $CMRO_2$ was determined by normalizing [Hb] by the cerebral blood volume. This step is not required for TR NIRS since both [Hb] and [HbO_2] are determined from the measured optical properties. A further advantage to directly measuring μ_a and μ_s' by TR NIRS is these values can also be used in the analysis of DCS data rather than assuming known values. Another advantage with TR NIRS is its superior depth sensitivity, which could prove useful when adapting these optical technologies to measuring CBF and $CMRO_2$ in adult patients (Elliott, Diop, Tichauer, Lee, & St. Lawrence, 2010; Liebert, Wabnitz, Steinbrink, Obrig, & Mo, 2004).

Although both studies demonstrate similar agreements between the NIRS and sagittal sinus $CMRO_2$ measurements, there was a large difference in the initial baseline $CMRO_2$ values between the two studies: 1.48 ± 0.17 ml O_2/100g/min in the current study and 2.60 ± 0.28 ml O_2/100g/min from Tichauer et al. (Tichauer, Hadway, et al., 2006). One possible explanation is the difference in baseline anesthetics in the two studies. Baseline measurements in the current study were acquired using a higher concentration of isoflurane (1.75-2% compared to 1.5%), which will reduce cerebral energy metabolism. Another contributing factor could be the difference in CBF measurements from CW and TR NIRS techniques. Previously, we have demonstrated that the CBF values from TR NIRS underestimated the CW NIRS values, although the reason for this difference was unclear (Diop, Tichauer, Elliott, Migueis, Lee, et al., 2010). Adjusting the current $CMRO_2$ values for this difference would increase the mean baseline value to 2.00 ± 0.22 ml O_2/100g/min, which is still below our previous results. Most likely, the overall difference between the two studies is a combination of both factors.

In addition to the different anesthetics, measurements were also conducted after administering sodium cyanide. This drug was used to alter cerebral oxidative metabolism by an alternative means, namely, the inhibition of mitochondrial cytochrome oxidase. Overall, the agreement between the DCS/TR-NIRS and sagittal sinus $CMRO_2$ values under this condition was similar to that observed under the different anesthetics. However, the metabolic effect of cyanide was smaller than expected based on a previous study involving newborn piglets (C. Cooper et al., 1999). This muted effect is likely a

result of injecting the sodium cyanide while the animals were under the deepest anesthetic (pentobarbital plus isoflurane). Nevertheless, cyanide did cause a small reduction in $CMRO_2$, which was observable by both techniques.

A potential limitation with the current study is that the CBF measurements obtained by the calibrated DCS technique were used to convert both the sagittal-sinus and NIRS venous oxygenation measurements into $CMRO_2$. Consequently, any systemic error in the optical CBF measurements would not be observed in this study. We previously demonstrated a very strong correlation between relative flow changes measured by DCS and CBF values measured by TR NIRS with a slope from the linear regression of 1.05 (Diop et al., 2011). This comparison was conducted over a range of CBF values from 17 to 90 ml/100g/min, which is very similar to the range observed in the current study. However, more validation studies would be required if the combined DCS/TR-NIRS approach were used to measure $CMRO_2$ under pathological conditions such as during ischemia or severe hypoxia that could result in greater changes in either CBF or SvO_2 (Ijichi et al., 2005; Tichauer, Brown, et al., 2006).

2.5 Conclusion

In summary, this study demonstrated that the combination of DCS and TR NIRS can be used to measure $CMRO_2$, as verified by the comparison to $CMRO_2$ values derived from cerebral venous blood samples. Experiments were conducted using piglets because they are similar in size to human newborns and, therefore, the DCS/TR-NIRS system could be used in clinical studies. Adapting this approach to the neonatal intensive care unit will require synchronizing the two optical systems to provide truly continuous CBF and $CMRO_2$ measurements. Extending this approach to adult patients represents a significant challenge as it requires depth-resolved techniques, such as the use of multi-layered modeling approaches, to measure CBF, cerebral oxygenation and the BFI accurately (Gagnon, Desjardins, Jehanne-Lacasse, Bherer, & Lesage, 2008; Jaillon et al., 2006; Wabnitz et al., 2010). Incorporating sensitivity functions for the different tissue layers into the analysis of bolus tracking data has been shown to improve the accuracy of CBF measurements in animal models; however, clinical studies will require validating this approach in human subjects (Elliott, Diop, Lee, & Lawrence, 2012; Elliott et al., 2010).

2.6 References

Altman, D., & Bland, J. (1983). Measurement in medicine: the analysis of method comparison studies. *Journal of the Royal Statistical Society. Series D (The Sttistician)*, *32*(3), 307–317. Retrieved from http://www.jstor.org/stable/10.2307/2987937

Behrman, R. (2006). Preterm birth: causes, consequences, and prevention. *Institute of Medicine of the National Acedemies*, 1–4.

Boas, D., Campbell, L., & Yodh, A. G. (1995). Scattering and imaging with diffusing temporal field correlations. *Physical Review Letters*, *75*(9), 1855–1858. Retrieved from http://link.aps.org/doi/10.1103/PhysRevLett.75.1855

Boas, D., & Franceschini, M. A. (2011). Haemoglobin oxygen saturation as a biomarker: the problem and a solution. *Philosophical Transactions. Series A, Mathematical, Physical, and Engineering Sciences*, *369*(1955), 4407–24. doi:10.1098/rsta.2011.0250

Boas, D., & Yodh, A. G. (1997). Spatially varying dynamical properties of turbid media probed with diffusing temporal light correlation. *Journal of the Optical Society of America A*, *14*(1), 192–215. doi:10.1364/JOSAA.14.000192

Brown, D. W., Hadway, J., & Lee, T.-Y. (2003). Near-infrared spectroscopy measurement of oxygen extraction fraction and cerebral metabolic rate of oxygen in newborn piglets. *Pediatric Research*, *54*(6), 861–7. doi:10.1203/01.PDR.0000090928.93045.BE

Brown, D. W., Picot, P. a, Naeini, J. G., Springett, R., Delpy, D. T., & Lee, T.-Y. (2002). Quantitative near infrared spectroscopy measurement of cerebral hemodynamics in newborn piglets. *Pediatric Research*, *51*(5), 564–70. Retrieved from http://www.ncbi.nlm.nih.gov/pubmed/11978878

Brun, N., Moen, A., & Borch, K. (1997). Near-infrared monitoring of cerebral tissue oxygen saturation and blood volume in newborn piglets. *American Journal of Physiology Heart and Circulatory Physiology*, *273*, H682–H686. Retrieved from http://ajpheart.physiology.org/content/273/2/H682.short

Buckley, E. M., Cook, N., Durduran, T., & Kim, M. (2009). Cerebral hemodynamics in preterm infants during positional intervention measured with diffuse correlation spectroscopy and transcranial Doppler ultrasound. *Optics Express*, *17*(15), 12571–12581. Retrieved from http://www.opticsinfobase.org/abstract.cfm?URI=oe-17-15-12571

Carp, S. A., Dai, G. P., Boas, D., Franceschini, M. A., & Kim, Y. R. (2010). Validation of diffuse correlation spectroscopy measurements of rodent cerebral blood flow with simultaneous arterial spin labeling MRI; towards MRI-optical continuous cerebral metabolic monitoring. *Biomedical Optics Express*, *1*(2), 553–565. doi:10.1364/BOE.1.000553

Cheung, C., Culver, J. P., Takahashi, K., Greenberg, J. H., & Yodh, A. G. (2001). In vivo cerebrovascular measurement combining diffuse near-infrared absorption and

correlation spectroscopies. *Physics in Medicine and Biology*, *46*(8), 2053–65. Retrieved from http://www.ncbi.nlm.nih.gov/pubmed/11512610

Contini, D., Torricelli, A., Pifferi, A., Spinelli, L., Paglia, F., & Cubeddu, R. (2006). Multi-channel time-resolved system for functional near infrared spectroscopy. *Optics Express*, *14*(12), 5418–32. Retrieved from http://www.ncbi.nlm.nih.gov/pubmed/19516708

Cooper, C., Cope, M., Springett, R., Amess, P., Penrice, J., Tyszczuk, L., … Delpy, D. (1999). Use of mitochondrial inhibitors to demonstrate that cytochrome oxidase near-infrared spectroscopy can measure mitochondrial dysfunction noninvasively in the brain. *Journal of Cerebral Blood Flow and Metabolism*, *19*(1), 27–38. doi:10.1097/00004647-199901000-00003

Cooper, J., Tichauer, K. M., Boulton, M., Elliott, J. T., Diop, M., Arango, M., … St. Lawrence, K. (2011). Continuous monitoring of absolute cerebral blood flow by near-infrared spectroscopy during global and focal temporary vessel occlusion. *Journal of Applied Physiology*, *110*(6), 1691–8. doi:10.1152/japplphysiol.01458.2010

Dietsche, G., Ninck, M., Ortolf, C., Li, J., Jaillon, F., & Gisler, T. (2007). Fiber-based multispeckle detection for time-resolved diffusing-wave spectroscopy: characterization and application to blood flow detection in deep tissue. *Applied Optics*, *46*(35), 8506–8514. doi:10.1364/AO.46.008506

Diop, M., Tichauer, K. M., Elliott, J., Migueis, M., & Lee, T. (2010). Time-resolved near-infrared technique for bedside monitoring of absolute cerebral blood flow. *Proceedings of SPIE*, *7555*(64166), 75550Z–75550Z–9. doi:10.1117/12.842521

Diop, M., Tichauer, K. M., Elliott, J. T., Migueis, M., Lee, T.-Y., & St. Lawrence, K. (2010). Comparison of time-resolved and continuous-wave near-infrared techniques for measuring cerebral blood flow in piglets. *Journal of Biomedical Optics*, *15*(5), 057004. doi:10.1117/1.3488626

Diop, M., Verdecchia, K., Lee, T.-Y., & St. Lawrence, K. (2011). Calibration of diffuse correlation spectroscopy with a time-resolved near-infrared technique to yield absolute cerebral blood flow measurements. *Biomedical Optics Express*, *2*(7), 2068–81. doi:10.1364/BOE.2.002068

Dominguez de Villota, E. D., Ruiz Carmona, M. T., Rubio, J. J., & de Andrés, S. (1981). Equality of the in vivo and in vitro oxygen-binding capacity of haemoglobin in patients with severe respiratory disease. *British Journal of Anaesthesia*, *53*(12), 1325–8. Retrieved from http://www.ncbi.nlm.nih.gov/pubmed/7317251

Durduran, T., Yu, G., Burnett, M. G., Detre, J. a, Greenberg, J. H., Wang, J., … Yodh, A. G. (2004). Diffuse optical measurement of blood flow, blood oxygenation, and metabolism in a human brain during sensorimotor cortex activation. *Optics Letters*, *29*(15), 1766–8. Retrieved from http://www.ncbi.nlm.nih.gov/pubmed/15352363

Durduran, T., Zhou, C., Buckley, E. M., Kim, M. N., Yu, G., Choe, R., … Licht, D. J. (2010). Optical measurement of cerebral hemodynamics and oxygen metabolism

in neonates with congenital heart defects. *Journal of Biomedical Optics*, *15*(3), 037004. doi:10.1117/1.3425884

Elliott, J. T., Diop, M., Lee, T.-Y., & Lawrence, K. S. (2012). Model-independent dynamic constraint to improve the optical reconstruction of regional kinetic parameters. *Optics Letters*, *37*(13), 2571–3. Retrieved from http://www.ncbi.nlm.nih.gov/pubmed/22743458

Elliott, J. T., Diop, M., Tichauer, K. M., Lee, T.-Y., & St. Lawrence, K. (2010). Quantitative measurement of cerebral blood flow in a juvenile porcine model by depth-resolved near-infrared spectroscopy. *Journal of Biomedical Optics*, *15*(3), 037014. doi:10.1117/1.3449579

Elwell, C. E., Henty, J. R., Leung, T. S., Austin, T., Meek, J. H., Delpy, D. T., & Wyatt, J. S. (2005). Measurement of CMRO2 in neonates undergoing intensive care using near infrared spectroscopy. *Advances in Experimental Medicine and Biology*, *566*, 263–8. doi:10.1007/0-387-26206-7_35

Fantini, S., Hueber, D., Franceschini, M. A., Gratton, E., Rosenfeld, W., Stubblefield, P. G., … Stankovic, M. R. (1999). Non-invasive optical monitoring of the newborn piglet brain using continuous-wave and frequency-domain spectroscopy. *Physics in Medicine and Biology*, *44*(6), 1543–63. Retrieved from http://www.ncbi.nlm.nih.gov/pubmed/10498522

Franceschini, M. A., Boas, D., Zourabian, A., Diamond, S. G., Nadgir, S., Lin, D. W., … Fantini, S. (2002). Near-infrared spiroximetry: noninvasive measurements of venous saturation in piglets and human subjects. *Journal of Applied Physiology*, *92*(1), 372–84. Retrieved from http://www.ncbi.nlm.nih.gov/pubmed/11744680

Gagnon, L., Desjardins, M. ’R., Jehanne-Lacasse, J., Bherer, L., & Lesage, F. Ú. Ú. (2008). Investigation of diffuse correlation spectroscopy in multi-layered media including the human head. *Optics Express*, *16*(20), 15514–15530. Retrieved from http://www.opticsinfobase.org/abstract.cfm?id=172103

Gisler, T., Rüger, H., Egelhaaf, S. U., Tschumi, J., Schurtenberger, P., & Rička, J. (1995). Mode-selective dynamic light scattering: theory versus experimental realization. *Applied Optics*, *34*(18), 3546–53. Retrieved from http://www.ncbi.nlm.nih.gov/pubmed/21052170

Graham, J. W. (2009). Missing data analysis: making it work in the real world. *Annual Review of Psychology*, *60*, 549–76. doi:10.1146/annurev.psych.58.110405.085530

Holland, B. A., Haas, D. K., Norman, D., Brant-Zawadzki, M., & Newton, T. H. (1986). MRI of normal brain maturation. *American Journal of Neuroradiology*, *7*(2), 201–208. Retrieved from http://www.ncbi.nlm.nih.gov/pubmed/3082150

Ijichi, S., Kusaka, T., Isobe, K., Islam, F., Okubo, K., Okada, H., … Itoh, S. (2005). Quantification of cerebral hemoglobin as a function of oxygenation using near-infrared time-resolved spectroscopy in a piglet model of hypoxia. *Journal of Biomedical Optics*, *10*(2), 024026. doi:10.1117/1.1899184

Jaillon, F., Skipetrov, S. E., Li, J., Dietsche, G., Maret, G., & Gisler, T. (2006). Diffusing-wave spectroscopy from head-like tissue phantoms: influence of a non-

scattering layer. *Optics Express*, *14*(22), 10181–94. Retrieved from http://www.ncbi.nlm.nih.gov/pubmed/19529414

Kienle, A., & Patterson, M. (1997). Improved solutions of the steady-state and the time-resolved diffusion equations for reflectance from a semi-infinite turbid medium. *Journal of the Optical Society of America A*, *14*(1), 246–254. Retrieved from http://www.opticsinfobase.org/abstract.cfm?&id=1660

Kim, M. N., Durduran, T., Frangos, S., Edlow, B. L., Buckley, E. M., Moss, H. E., … Kofke, W. A. (2010). Noninvasive measurement of cerebral blood flow and blood oxygenation using near-infrared and diffuse correlation spectroscopies in critically brain-injured adults. *Neurocritical Care*, *12*(2), 173–80. doi:10.1007/s12028-009-9305-x

Kurth, C. D., McCann, J. C., Wu, J., Miles, L., & Loepke, A. W. (2009). Cerebral oxygen saturation-time threshold for hypoxic-ischemic injury in piglets. *Anesthesia and Analgesia*, *108*(4), 1268–77. doi:10.1213/ane.0b013e318196ac8e

Kusaka, T., Isobe, K., Nagano, K., Okubo, K., Yasuda, S., Kondo, M., … Onishi, S. (2002). Quantification of cerebral oxygenation by full-spectrum near-infrared spectroscopy using a two-point method. *Comparative Biochemistry and Physiology. Part A, Molecular & Integrative Physiology*, *132*(1), 121–32. Retrieved from http://www.ncbi.nlm.nih.gov/pubmed/12062200

Liebert, A., Wabnitz, H., Steinbrink, J., Obrig, H., & Mo, M. (2004). Time-resolved multidistance near-infrared spectroscopy of the adult head: intracerebral and extracerebral absorption changes from moments of distribution of times of flight of photons. *Applied Optics*, *43*(15), 3037–3047. Retrieved from http://www.opticsinfobase.org/abstract.cfm?id=79891

Matcher, S., Cope, M., & Delpy, D. T. (1993). Use of the water absorption spectrum to quantify tissue chromophore concentration changes in near-infrared spectroscopy. *Physics in Medicine and Biology*, *39*(1), 177–96. Retrieved from http://www.ncbi.nlm.nih.gov/pubmed/7651995

Mchedlishvili, G. (1986). *Arterial behavior and blood circulation in the brain*. (J. Bevan, Ed.)*Japanese Journal of Phyiosology*. New York: Consultants Bureau. Retrieved from http://www.ncbi.nlm.nih.gov/pubmed/11281993

Mintun, M., Raichle, M. E., Martin, W. R., & Herscovitch, P. (1984). Brain oxygen utilization measured with O-15 radiotracers and positron emission tomography. *Journal of Nuclear Medicine*, *25*(2), 177–87. Retrieved from http://www.ncbi.nlm.nih.gov/pubmed/6610032

Ntziachristos, V., & Chance, B. (2001). Accuracy limits in the determination of absolute optical properties using time-resolved NIR spectroscopy. *Medical Physics*, *28*(6), 1115. doi:10.1118/1.1373674

O'Leary, H., Gregas, M. C., Limperopoulos, C., Zaretskaya, I., Bassan, H., Soul, J. S., … du Plessis, A. J. (2009). Elevated cerebral pressure passivity is associated with prematurity-related intracranial hemorrhage. *Pediatrics*, *124*(1), 302–9. doi:10.1542/peds.2008-2004

Paunescu, L. A., Michalos, A., Choi, J. H., Wolf, U., Wolf, M., & Gratton, E. (2001). In vitro correlation between reduced scattering coefficient and hemoglobin concentration of human blood determined by near-infrared spectroscopy, *4250*, 319–326.

Powers, W., Grubb, R. L., Darriet, D., & Raichle, M. E. (1985). Cerebral blood flow and cerebral metabolic rate of oxygen requirements for cerebral function and viability in humans. *Journal of Cerebral Blood Flow and Metabolism*, *5*(4), 600–8. doi:10.1038/jcbfm.1985.89

Reivich, M. (1964). Arterial PCO2 and cerebral hemodynamics. *American Journal of Physiology--Legacy*, *206*(1), 25–35. Retrieved from http://ajplegacy.physiology.org/content/206/1/25.short

Roche-Labarbe, N., Carp, S. A., Surova, A., Patel, M., Boas, D. A., Grant, P. E., & Franceschini, M. A. (2010). Noninvasive optical measures of CBV, StO2, CBF index, and rCMRO2 in human premature neonates' brains in the first six weeks of life. *Human Brain Mapping*, *31*(3), 341–352. doi:10.1002/hbm.20868

Roche-Labarbe, N., Fenoglio, A., Aggarwal, A., Dehaes, M., Carp, S. A., Franceschini, M. A., & Grant, P. E. (2012). Near-infrared spectroscopy assessment of cerebral oxygen metabolism in the developing premature brain. *Journal of Cerebral Blood Flow & Metabolism*, *32*(3), 481–488. doi:10.1038/jcbfm.2011.145

Sakamoto, T., Jonas, R. a, Stock, U. a, Hatsuoka, S., Cope, M., Springett, R., & Nollert, G. (2001). Utility and limitations of near-infrared spectroscopy during cardiopulmonary bypass in a piglet model. *Pediatric Research*, *49*(6), 770–6. Retrieved from http://www.ncbi.nlm.nih.gov/pubmed/11385136

Scremin, O., Sonnenschein, R. R., & Rubinstein, E. H. (1982). Cerebrovascular anatomy and blood flow measurements in the rabbit. *Journal of Cerebral Blood Flow and Metabolism*, *2*(1), 55–66. doi:10.1038/jcbfm.1982.6

Siesjo, B. (1978). Brain energy metabolism and catecholaminergic activity in hypoxia, hypercapnia and ischemia. *J Neural Transm Suppl.*, *14*, 17–22. Retrieved from http://www.getcited.org/pub/101760013

Soul, J. S., Hammer, P. E., Tsuji, M., Saul, J. P., Bassan, H., Limperopoulos, C., … du Plessis, A. J. (2007). Fluctuating pressure-passivity is common in the cerebral circulation of sick premature infants. *Pediatric Research*, *61*(4), 467–73. doi:10.1203/pdr.0b013e31803237f6

Springett, R., Newman, J., Cope, M., & Delpy, D. T. (2000). Oxygen dependency and precision of cytochrome oxidase signal from full spectral NIRS of the piglet brain. *American Journal of Physiology Heart and Circulatory Physiology*, *279*(5), H2202–H2209.

Tichauer, K. M., Brown, D. W., Hadway, J., Lee, T.-Y., & St. Lawrence, K. (2006). Near-infrared spectroscopy measurements of cerebral blood flow and oxygen consumption following hypoxia-ischemia in newborn piglets. *Journal of Applied Physiology*, *100*(3), 850–7. doi:10.1152/japplphysiol.00830.2005

Tichauer, K. M., Elliott, J. T., Hadway, J., Lee, T.-Y., & St. Lawrence, K. (2009). Cerebral metabolic rate of oxygen and amplitude-integrated electroencephalography during early reperfusion after hypoxia-ischemia in piglets. *Journal of Applied Physiology*, *106*(5), 1506–12. doi:10.1152/japplphysiol.91156.2008

Tichauer, K. M., Hadway, J., Lee, T.-Y., & St. Lawrence, K. (2006). Measurement of cerebral oxidative metabolism with near-infrared spectroscopy: a validation study. *Journal of Cerebral Blood Flow and Metabolism*, *26*(5), 722–30. doi:10.1038/sj.jcbfm.9600230

Tichauer, K. M., Holt, R. W., El-Ghussein, F., Zhu, Q., Dehghani, H., Leblond, F., & Pogue, B. W. (2011). Imaging workflow and calibration for CT-guided time-domain fluorescence tomography. *Biomedical Optics Express*, *2*(11), 3021–36. doi:10.1364/BOE.2.003021

Volpe, J. (1990). Brain injury in the premature infant: is it preventable? *Pediatric Research*, *27*(6), S28–S33. Retrieved from http://journals.lww.com/pedresearch/Abstract/1990/06001/Brain_Injury_in_the_Premature_Infant__Is_It.8.aspx

Wabnitz, H., Moeller, M., Liebert, A., Obrig, H., Steinbrink, J., & Macdonald, R. (2010). Time-Resolved Near-Infrared Spectroscopy and Imaging of the Adult Human Brain. *Advances in Experimental Medicine and Biology*, *662*, 143–148. doi:10.1007/978-1-4419-1241-1

Watzman, H. H. M., Kurth, C. C. D., Montenegro, L. L. M., Rome, J., Steven, J. M., & Nicolson, S. C. (2000). Arterial and venous contributions to near-infrared cerebral oximetry. *Anesthesiology*, *93*(4), 947. doi:10.1002/star.200590022

Wintermark, M., Sesay, M., Barbier, E., Borbély, K., Dillon, W. P., Eastwood, J. D., … Yonas, H. (2005). Comparative overview of brain perfusion imaging techniques. *Stroke*, *36*(9), e83–99. doi:10.1161/01.STR.0000177884.72657.8b

Wong, F. Y., Leung, T. S., Austin, T., Wilkinson, M., Meek, J. H., Wyatt, J. S., & Walker, A. M. (2008). Impaired autoregulation in preterm infants identified by using spatially resolved spectroscopy. *Pediatrics*, *121*(3), e604–11. doi:10.1542/peds.2007-1487

Zhou, C., Eucker, S. a, Durduran, T., Yu, G., Ralston, J., Friess, S. H., … Yodh, A. G. (2009). Diffuse optical monitoring of hemodynamic changes in piglet brain with closed head injury. *Journal of Biomedical Optics*, *14*(3), 034015. doi:10.1117/1.3146814

Zierler, K. L. (1965). Equations for Measuring Blood Flow by External Monitoring of Radioisotopes. *Circulation Research*, *16*(4), 309–321. doi:10.1161/01.RES.16.4.309

Zirak, P., Delgado-Mederos, R., Martí-Fàbregas, J., & Durduran, T. (2010). Effects of acetazolamide on the micro- and macro-vascular cerebral hemodynamics: a diffuse optical and transcranial doppler ultrasound study. *Biomedical Optics Express*, *1*(5), 1443–1459. doi:10.1364/BOE.1.001443

Chapter 3

3 Measurements of Cerebral Blood Flow in Pigs by Diffuse Correlation Spectroscopy on the Exposed Cortex

This chapter is adapted from the paper entitled "Assessment of the best flow model to characterize diffuse correlation spectroscopy data acquired directly on the brain" by Verdecchia K, Diop M, Morrison L, Lee T-Y, St. Lawrence K, published in Biomedical Optics Express, vol. 6(11) pp. 4288-4301 (2015).

3.1 Introduction

Near-infrared spectroscopy (NIRS) methods based on the quantification of light absorption at specific wavelengths have been developed for measuring key physiological parameters, such as tissue perfusion, blood volume and oxygenation (Boas & Franceschini, 2011; Durduran & Yodh, 2014; Mesquita et al., 2011). For example, blood flow can be measured by manipulating arterial oxygenation saturation or injecting a light-absorbing contrast agent (Diop, Verdecchia, Lee, & St Lawrence, 2011; Kyle Verdecchia, Diop, Lee, & St. Lawrence, 2013; Weigl et al., 2014); however, these techniques only enable single time-point measurements. An alternative approach that provides continuous blood flow monitoring is diffuse correlation spectroscopy (DCS) (Durduran & Yodh, 2014). This method indirectly measures changes in blood flow by monitoring light intensity fluctuations caused by the movement of erythrocytes in tissue (Boas, Campbell, & Yodh, 1995; Ninck, Untenberger, & Gisler, 2010). More specifically, the propagation of photons through extravascular tissue, where they endure multiple scattering events that randomize their direction, and within vessels, which contain moving erythrocytes, induces decorrelation of the light that manifests as intensity fluctuations. Blood flow is assessed by characterizing light intensity decorrelation using a model that describes the movement of erythrocytes.

Currently, the most common approach for analyzing DCS data is by modeling erythrocyte motion as a Brownian diffusion-like process, which has previously been

shown in various species (swine, rodent and human) to provide a better characterization of the normalized temporal intensity autocorrelation function than the expected random flow model (R_{FM}) (Binzoni & Martelli, 2015), which describes the motion of erythrocytes as ballistic (Carp, Dai, Boas, Franceschini, & Kim, 2010; Diop et al., 2011; Kim et al., 2010; Yu et al., 2007; Zhou et al., 2007). To explain this unexpected finding, Carp et al. proposed a hybrid model, referred to as the hydrodynamic diffusion model (H_{DM}), that accounts for both the possibility of multiple light-scattering events within a vessel, characteristic of diffusive motion, and light-scattering events across vessels, characteristic of random ballistic motion (Carp et al., 2011). Furthermore, Carp et al. demonstrated that the DCS measurements are best fit by the H_{DM} for data acquired on premature newborns (Carp et al., 2011).

Although DCS has been shown to be a promising tool for blood flow monitoring, the most appropriate flow model for characterizing perfusion is still debatable. The purpose of the current study was to compare the ability of the three flow models to characterize DCS data acquired directly on the exposed cerebral cortex of juvenile pigs. This approach removes signal contributions from the extracerebral tissues (scalp and skull) that can alter the shape of DCS autocorrelation curves due to partial volume errors caused by tissue heterogeneity (Gagnon, Desjardins, Jehanne-Lacasse, Bherer, & Lesage, 2008). In addition, cerebral blood flow (CBF) was independently measured by computed tomography perfusion (CTP) for comparison to the flow estimates obtained by each of the three flow models.

3.1.1 Diffuse Correlation Spectroscopy

To assess dynamics of light scatterers, DCS measures the normalized intensity autocorrelation function, $g_2(\rho,\tau)$ given by (Cheung, Culver, Takahashi, Greenberg, & Yodh, 2001):

$$g_2(\rho,\tau) \equiv \frac{\langle I(\rho,t)I(\rho,t+\tau)\rangle}{\langle I(\rho,t)\rangle^2} \tag{3.1}$$

where <I> , ρ and τ represents the average detected intensity, the source-detector distance (SDD) and the correlation time, respectively. Equation 3.2 is related to the electric field autocorrelation function by the Siegert relation (Lemieux & Durian, 1999):

$$g_2(\rho,\tau) = 1 + \beta \frac{|G_1(\rho,t)|^2}{\langle I(\rho,t)\rangle^2} \tag{3.2}$$

where, β is the coherence factor of the detection channel and $G_1(\rho,\tau)$ is the electric field autocorrelation function. Previously shown, $G_1(\rho,\tau)$ satisfies a diffusion equation (Boas et al., 1995; Boas & Yodh, 1997). Assuming a point light source with unit intensity, the analytical solution to the correlation diffusion equation for a semi-infinite homogeneous medium is given by (Cheung et al., 2001; Diop et al., 2011; Durduran, Choe, Baker, & Yodh, 2010):

$$G_1(\rho,\tau) = \frac{3\mu_s'}{4\pi}\left[\frac{\exp(-\mu_D r_1)}{r_1} - \frac{\exp(-\mu_D r_1)}{r_2}\right] \tag{3.3}$$

Where, $r_1 = [\rho^2+(z_0)^2]^{1/2}$, $r_2 = [\rho^2+(z_0+2z_b)^2]^{1/2}$, z_b is the effective depth of the source, and $z_b = 2D(1+R_{eff})/(1-R_{eff})$ is the distance above the tissue surface at which the fluence vanishes, where D is the diffusion coefficient given as $(3\mu_s')^{-1}$ and R_{eff} is the effective reflection coefficient calculated to be 0.493 for the refraction indices of tissue and air (Haskell et al., 1994). Furthermore, in Equation 3.3, μ_D is given by:

$$\mu_D^2(\tau) = \frac{3\nu}{D}(\mu_a + \alpha\mu_s' k_0^2\langle r(\tau)\rangle) \tag{3.4}$$

The coefficients μ_a and μ_s' are the absorption and reduced scattering coefficient, respectively, k_0 is the wavenumber of light in the medium, α is the proportion of moving scatters (predominantly red blood cells) to all scatterers and is related to the blood volume, and $<\Delta r^2(\tau)>$ is the mean-square displacement of the moving scatterers during a correlation time τ. In the analysis of measured $g_2(\rho,\tau)$, the specific expression for $<\Delta r^2(\tau)>$ is given by one of the following flow models.

3.1.2 Random Flow Model

The R_{FM} is based on the assumption that photon scattering events associated with motion occur from scatterers that are uncorrelated (i.e. in separate vessels). In this case, the mean-square displacement is given by:

$$\langle \Delta r^2(\tau) \rangle = V^2 \tau^2 \tag{3.5}$$

where, V is the velocity of the moving erythrocytes. The product αV^2 is referred to as the random blood flow index (BFI_R).

3.1.3 Brownian Diffusion Model

The Brownian diffusion model (B_{DM}) assumes incoherent motion caused by multiple interactions of moving scatterers, such as erythrocytes within the same vessel. It is the most commonly used model in DCS analysis and the Brownian displacement formula is given by:

$$\langle \Delta r^2(\tau) \rangle = 6 D_B \tau \tag{3.6}$$

where, D_B is the effective diffusion coefficient, and αD_B is referred to as the Brownian blood flow index (BFI_B).

3.1.4 Hydrodynamic Diffusion Model

Carp et al. proposed using the Langevin formula for red blood cell mean squared displacement to account for the occurrence of both Brownian and random flow motion (Carp et al., 2011):

$$\langle \Delta r^2(\tau) \rangle = 6 D_H \left\{ \tau - \tau_c \left[1 - \exp\left(-\frac{\tau}{\tau_c} \right) \right] \right\} \tag{3.7}$$

required to establish diffusive motion. Unlike the Brownian diffusion model, τ_c accounts for possible ballistic motion at short delay times. For the H_{DM}, the two fitting parameters are τ_c and αD_H, the hydrodynamic blood flow index (BFI_H).

3.2 Methods

3.2.1 Experimental Procedure

Animal experiments were conducted in accordance with the guidelines of the Canadian Council of Animal Care (CCAC) and approved by the Animal Use Committee at Western University. Juvenile pigs (~6 weeks old) were obtained from a local supplier on the day of the experiment. Following anesthetic induction with 5% isoflurane, the animals were tracheotomized and mechanically ventilated on a mixture of oxygen and medical air. A catheter was inserted into a femoral artery for blood gas analysis. After surgery, the isoflurane was reduced to 3-4% and the animal was transported to the computed tomography (CT) suite where the experiments were conducted using a portable NIRS/DCS system.

The animal was placed prone on the bed of the CT scanner on top of a heated blanket used to maintain rectal temperature between 38 and 39 ºC throughout the experiment. To place the optical probes directly on the brain, a rectangular piece of scalp tissue (~10 cm^2) located laterally to the midline on the right hemisphere was first excised. A caustic pencil was used to cauterize the incised scalp tissue to prevent bleeding. Lastly, a handheld dremel was used to drill two burr holes, which were the size of optical fibers, into the skull parallel to the midline. Care was taken to ensure that the dura mater was not punctured by the dremel. Contact pressure on the dura was minimized since the fibers fit tightly in the holes, which carried their weight. Furthermore, the distance to the dura could be measured on the CT images (Figure 3-1) and used to guide the distance that the fibers were inserted. The burr holes were 7 mm apart, with the exception of one animal for which the separation was 20 mm. A scout CT scan with an anatomical marker on top of the skull was used to define the location of the burr holes.

Following surgery, the emission and detection fibers were placed in the posterior and anterior burr holes, respectively. The head of the pig was covered by an opaque blanket to reduce ambient light contamination. During the experiment, arterial oxygen saturation, heart and respiration rates, mean arterial pressure, and rectal temperature were continuously monitored. Arterial blood samples were obtained to measure arterial pH,

partial carbon dioxide tension ($paCO_2$), partial oxygen tension (paO_2) and blood glucose (BG) concentration. Samples were acquired before and after each set of measurements to assess physiological stability during the data acquisition period. Intermittent dextrose injections were administered to maintain normal BG levels (between 5 and 7 mmol/L).

Two sets of CT, time-resolved (TR) NIRS, and DCS data were acquired in each experiment: first at normocapnia ($paCO_2$ between 38 and 42 mmHg) and then at hypocapnia ($paCO_2$ between 20 and 25 mmHg). Each capnic level was maintained by adjusting the ventilation volume and rate. The sequence of data acquisition during normocapnia consisted of CT perfusion, TR NIRS measurements of optical properties and DCS. For the hypocapnic condition the sequence of data acquisition was reversed in order to avoid removing the optical probes from the burr holes between the two conditions.

3.2.2 Computed Tomography

The dynamic CT protocol consisted of a bolus injection of 1.0 mL/kg of iodine-based contrast agent (iopamidol [370-Isovue®], Bracco S.p.A., Milan, Italy) at a rate of 3 mL/s into the cephalic vein once during each capnic condition. The first five animals were scanned by a Lightspeed QXi multislice scanner (General Electric Company, Waukesha, WI) and the last three animals were scanned by the Revolution CT scanner (General Electric Company, Waukesha, WI) due to scanner availability. Each scan (slice thickness = 2.5 mm, current = 200 mA, energy = 80 kVp, FOV=140×140×40 mm) provided sixteen coronal slices, once every second, for a period of 40 s. The field of view covered the entire head of the pig. Functional maps of CBF were calculated using the clinical CT perfusion software package (PERFUSION 5, General Electric Healthcare Worldwide), which was developed and validated in house (Cenic, Nabavi, Craen, Gelb, & Lee, 1999). Region of interest (ROI) analysis was performed using an in-house developed software that performed pixel thresholding to remove signal contributions from large vessels that can lead to overestimation of CBF (Murphy et al., 2006). Five sequential slices between the burr holes that were visible on the anatomical CT images were chosen as they correspond to the “banana-shaped” path of the near-infrared light between the emission and detection optical fibers, as seen in Figure 3-1. For each slice, an ROI (~5 cm

diameter) was drawn on the cerebral cortex near the skull, since NIRS is most sensitive to superficial tissue. The CBF values were obtained by averaging over the ROIs in the five slices.

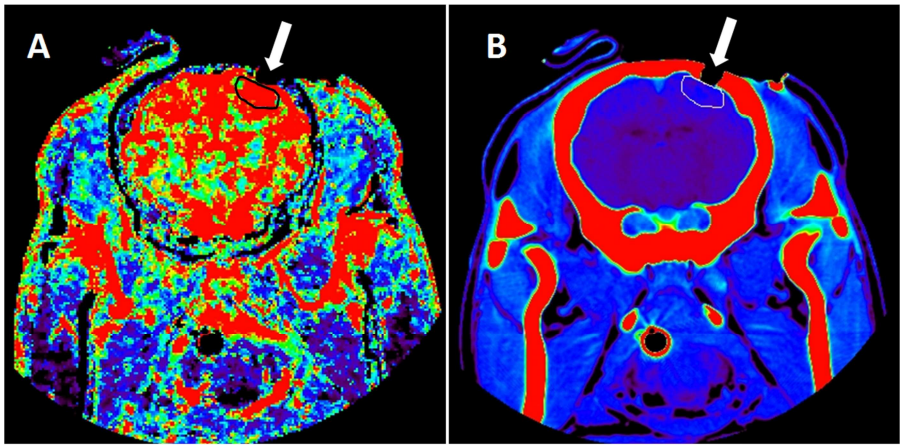

Figure 3-1: Single slice of the exposed cortex of a pig: perfusion map and anatomical CT images

A CT image of a single slice for a blood flow map (A) and the corresponding anatomical map (B). The ROI, shown in black for A and white for B, was manually drawn on the superficial cortex using in-house software. The burr hole, which exposed the cortex and held the optical fiber, is identified by the white arrow.

3.2.3 Optical Methods

3.2.3.1 Time-Resolved NIRS

The TR NIRS systems consisted of a picosecond pulsed diode laser (LDH-P-C 764, PicoQuant, Germany) emitting at 764 nm, with an average output power and pulse repetition rate of 1.4 mW and 80 MHz, respectively. The light was attenuated using electronically controlled variable neutral density filters (NDC-50C-4M, Thorlabs) and coupled to a multimode emission fiber used for both DCS and TR NIRS (emission probe: N.A. = 0.22, core = 400 µm; Fiberoptics Technology, Pomfret, CT). A 2-m fiber (N.A. = 0.22, core = 400 µm; Fiberoptics Technology, Pomfret, CT) was used to detect light at a SDD of 7-mm. The TR NIRS detection fiber was coupled to a fast hybrid photomultiplier detector with Peltier cooling (PMA Hybrid, PicoQuant, Germany). The output of the detector was sent to a multichannel picosecond event timer and time-correlated single-photon counting (TCSPC) module (HydraHarp 400, PicoQuant, Germany). The system was given at least a 2-hour warmup period to stabilize the laser and detection system

before acquiring data (Verdecchia, Diop, Lee, & St. Lawrence, 2015). Under each capnic condition, a distribution of times of flight of photons (DTOF) was recorded for 30 seconds. At the end of the study, the instrument response function (IRF) was measured to account for systemic temporal dispersion (Ntziachristos & Chance, 2001).

Tissue optical properties (μ_a and μ_s') were acquired for each condition to reduce inter-subject variability when extracting blood flow indices from DCS (Diop et al., 2011; Irwin et al., 2011). A three-parameter fitting routine, described in detail elsewhere (Diop et al., 2010), was used to extract estimates of μ_a, μ_s' and an amplitude scaling factor during normocapnia. The model used to fit the DTOF was the solution of the diffusion approximation for a semi-infinite homogeneous medium convolved with the measured IRF. The short SDD was calibrated with a phantom of known optical properties. The fitting range was set to 95% and 30% of the peak DTOF value for the ascending and descending sides, respectively. The measured μ_s' for normocapnia was fixed when analyzing the DTOF acquired during hypocapnia to reduce the number of fitting parameters to μ_a and amplitude scaling factor.

3.2.3.2 Diffuse Correlation Spectroscopy

The light source of the DCS system consisted of a continuous-wave laser (DL785-100-S, CrystalLaser, Nevada) emitting at 785 nm with a maximum output power of 100 mW and a coherence length >5 m. As with the TR NIRS system, the emitted light was attenuated by electronically controlled variable neutral density filters and coupled to the multimode emission fiber. A single-mode fiber (SMF-28e+, N.A. = 0.14, length = 4 m, core = 8.2 µm, single-mode cutoff wavelength at 1260 nm) was placed in the anterior burr hole of the animal and was used for detecting the temporal light intensity fluctuations. The SMF was tightly wrapped into a 5-cm coil to increase the losses of the higher-order modes before being coupled to the input-channel of the avalanche photodiode of a single photon counting module (SPCM-AQ4C, Excelitas Canada Inc, QC, Canada) (Dietsche et al., 2007; Gisler et al., 1995). The output of the SPCM was sent to a photon correlator board (DPC-230, Beker & Hickl, Germany) that computed the normalized intensity autocorrelation functions (g_2).

For each animal, two g_2 curves were acquired, one during normocapnia and one during hypocapnia, over an acquisition period of 90 s. The μ_a and μ_s' measured by TR NIRS were used in the DCS fitting routine. Each g_2 curve was analyzed three times using the solution of the diffusion approximation for a semi-infinite homogeneous medium including one of the three flow models (B_{DM}, R_{FM} and H_{DM}). The start and end limits for the fitting were defined by correlation times of 0.6 μs and 1 ms, respectively. In the fitting procedure, the coherence factor β was set to the value determined by averaging the first 10 data points of each g_2 curve.

3.2.4 Statistical Analysis

All errors are given as the standard errors of the mean (SEM), unless stated otherwise. All statistics were computed with the IBM SPSS Statistics 20 software package. For the measured physiological parameters, a multivariate analysis of variance (ANOVA), which included pH, $paCO_2$, paO_2, cGlu, ctHb, MAP, HR, temperature, and SpO_2, was computed to determine significant changes between capnic conditions. For two experiments, the TR NIRS data set was not experimentally collected due to overheating of the detector and therefore were determined by the average optical properties of the remaining animals during normocapnia. For the hypocapnia optical properties, the μ_a values were estimated from the average change in absorption from normocapnia to hypocapnia measured by all animals in this study. A one-way ANOVA compared capnic conditions for measured μ_a and BFI values, and, for the former, a post-hoc test [Tukey's honest significant difference (HSD)] identified any significant light absorbing outliers between subjects.

A direct comparison between the sums of squares (SS) determined the best fit of the B_{DM} and R_{FM}, since both models included one fitting parameter. However, the extra fitting parameter (τ_c) included in the H_{DM} is expected to reduce the variance in the fit of the measured $g_2(\rho,\tau)$. Therefore, an F-test was used to compare whether the improvements by the H_{DM} to fit the measured $g_2(\rho,\tau)$ curves, due to the additional fitting parameter, exceeded the reduction in variance similarly to the approach used by Carp et al. (Carp et al., 2011). The degree of freedom used in the F-test was determined by the number of correlation bins that the individual fit required, which was 164. For the H_{DM} to better characterize the data compared to either the B_{DM} or the R_{FM}, the calculated F-

number had to exceed a critical F-value of 3.9, as determined by the finv function in MATLAB (Mathworks, Natick, MA) for a $p<0.05$.

Linear regression analysis was performed to assess the correlation between CBF measured by CTP, and the blood flow index obtained by each of the three DCS models and τ_c for the H_{DM}. A Bland-Altman plot was used to assess the difference in the percent flow reductions measured by DCS and CTP (Altman & Bland, 1983). For the Bland-Altman plot, a one-sample t-test identified differences between the two modalities (DCS and CTP), and a linear regression was used to determine any proportionality bias.

3.3 Results

3.3.1 Physiological Parameters and Optical Properties

Eleven juvenile pigs (ten females, one male) were used in the study with an average weight of 16.0 ± 0.7 kg; however, only nine animals were scanned by CTP due to limited access to the CT scanner for the first two experiments.

Table 3-1: Physiological parameters during normocapnia and hypocapnia

Condition	*pH	*$paCO_2$ [mmHg]	paO_2 [mmHg]	ctHb [g/dL]	MAP [mmHg]	HR [bpm]
Normocapnia	7.45 ± 0.01	40.2 ± 0.3	182 ± 11	10.2 ± 0.3	43.6 ± 1.9	128 ± 8
Hypocapnia	7.62 ± 0.02	22.1 ± 0.4	213 ± 12	9.8 ± 0.4	38.1 ± 1.9	121 ± 7

Note: Data are presented as average ± SEM. $paCO_2$, partial pressure of carbon dioxide in the blood; paO_2, partial pressure of oxygen in the blood; MAP, mean arterial blood pressure; HR, heart rate.
* $p<0.05$ between conditions.

Table 3-1 lists the physiological parameters measured during normocapnia and hypocapnia. A multivariate ANOVA indicated significant differences between capnic conditions for blood pH [$p<0.001$, partial-$\eta^2=0.84$, power=1.00] and arterial carbon dioxide pressure ($paCO_2$) [$p<0.001$, partial-$\eta^2=0.98$, power=1.00] as expected. All other physiological parameters, including BG concentration, temperature and arterial oxygen saturation, did not change. Their mean values were 4.0 ± 0.2 mmol/L, 38.4 ± 0.1 °°C, and 95 ± 1%, respectively.

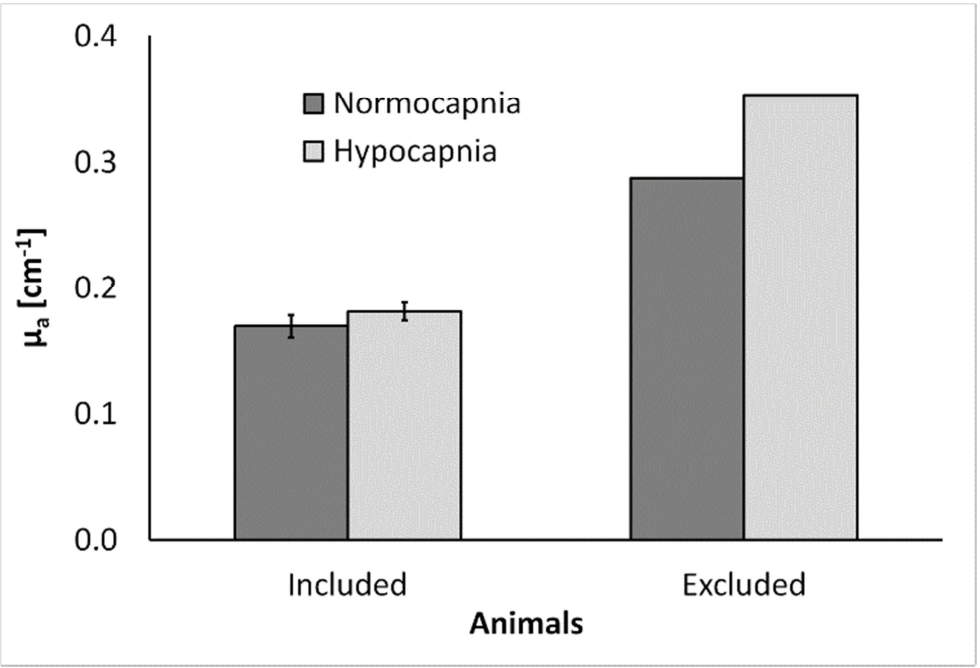

Figure 3-2: Tissue absorption measured by TR NIRS directly on the brain

Average μ_a values for the 10 animals included in this study and the μ_a value of the excluded outlier. Absorption values are presented for normocapnic (black) and hypocapnic (grey) conditions. The large μ_a for the outlier was attributed to excessive blood in the emission burr hole. Error bars represent the SEM.

Figure 3-2 presents the average μ_a values measured by TR NIRS during normocapnia and hypocapnia. No significant difference between the two conditions was observed [$p>0.55$, partial-$\eta^2=0.02$, power=0.09]. Following surgery, visible hemorrhaging in the emission burr hole was observed in one animal, which resulted in high μ_a values, as confirmed by a Tukey HSD post-hoc analysis (Figure 3-2). Consequently, the data from this animal were removed from further analysis, unless stated otherwise. The mean μ_s' for all animals was 10.7 ± 1.3 cm^{-1}.

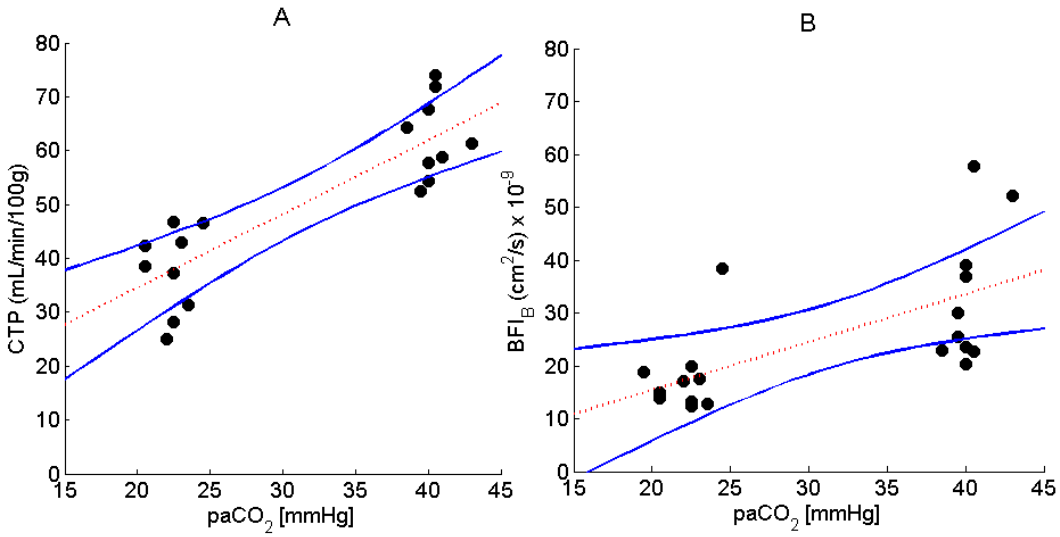

Figure 3-3: Hemodynamics measured by CTP and DCS during normocapnia and hypocapnia

Measured flow by (A) CTP (N = 9) and (B) DCS using the B_{DM} (N = 10), during normocapnia and hypocapnia. The line of best fit and $CI_{95\%}$ are represented by the dashed red line and blue lines, respectively.

Figure 3-3 presents CBF values measured by CTP and the BFI_B derived from the DCS data, both plotted as a function of $paCO_2$. The outlier identified in Figure 3-2 was excluded from the DCS data. The results from the B_{DM} are presented since it is the model most commonly used to analyze DCS data. Regression analysis resulted in a slope of 1.4 ± 0.20 mL/min/100g/mmHg ($CI_{95\%}$: 0.94, 1.8, $p<0.001$), an intercept of 7.1 ± 6.6 mL/min/100g ($CI_{95\%}$: -6.8, 21.1, $p>0.29$) and correlation coefficient (R) of 0.86 for CBF versus $paCO_2$. Likewise, the line of best fit from Figure 3-3B had a slope of (1.2 ± 0.3) x 10^{-9} $cm^2/s/mmHg$ [$CI_{95\%}$: (0.45, 1.86) x 10^{-9}, $p<0.003$], an intercept of (1.7 ± 10.9) x 10^{-9} cm^2/s [$CI_{95\%}$: (-21.2, 24.6) x 10^{-9}, $p>0.88$] and R of 0.63.

Table 3-2 lists the mean CBF values measured by CTP and corresponding BFI values derived from the DCS data using each of the three flow models. All values (CBF, BFI_B, BFI_R and BFI_H) were significantly different ($p<0.05$) between the two capnic conditions.

Table 3-2: Hemodynamic parameters measured by CTP and DCS during normocapnia and hypocapnia

Condition	*CBF [mL/min/100g]	*BFI_B [10^{-9} cm^2/s]	*BFI_R [10^{-3} cm^2/s]	*BFI_H [10^{-9} cm^2/s]	*τ_c [μs]
Normocapnia	62.5 ± 2.5	47.6 ± 4.9	37.2 ± 8.0	70.0 ± 8.2	2.72 ± 0.34
Hypocapnia	37.7 ± 2.6	27.9 ± 4.1	12.5 ± 3.3	38.2 ± 6.4	3.52 ± 0.29

Note: Values represent the average ± SEM. CBF, cerebral blood flow quantified by CTP; BFI_B, blood flow index determined by the Brownian flow model; BFI_R, blood flow index determined by the random flow model; BFI_H, blood flow index determined by the hydrodynamic flow model; τ_c, the time scale for the randomization of velocity vectors associated with RBC scattering events.
* $p<0.05$ between conditions.

Included in Table 3-2 is τ_c from the H_{DM}, which was also significantly different ($p<0.05$) between conditions. Not given in Table 3-2 are the average value of β, which was 0.152 ± 0.002 for all models; no significant differences were observed between capnic conditions.

3.3.2 Example of the Best-Fit of the Flow Models

Figure 3-4 shows normalized intensity autocorrelation curves obtained on the exposed cerebral cortex of one animal during normocapnia (blue) and hypocapnia (red).

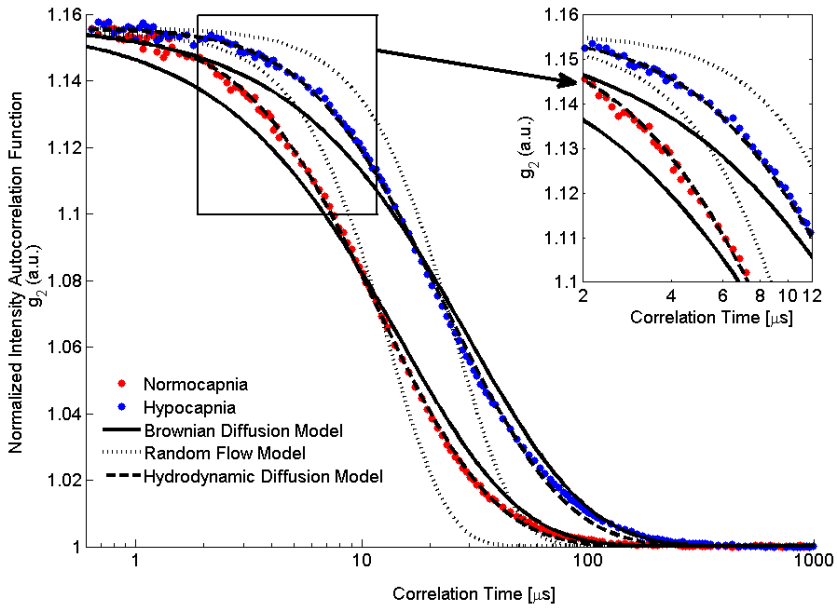

Figure 3-4: Measured DCS decay curves acquired during normocapnia and hypocapnia

DCS autocorrelation curves during normocapnia (red dots) and hypocapnia (blue dots) from one animal. Also shown are the best-fit to the three DCS flow models: BFI_B (solid line), BFI_R (dotted line) and BFI_H (dashed line). Data were acquired with a count rate of ~600 kHz for a total acquisition time of 30 seconds. To visually enhance the differences between the fits of the three models, a portion of the graph is displayed that focuses on correlation times between 2 to 12 μs, which encompass the initial decay of the measured intensity autocorrelation functions.

The normalized intensity autocorrelation curves decayed faster during normocapnia than during hypocapnia, reflecting the higher blood flow in the former condition. For the example shown in Figure 3-4, the blood flow reductions measured by BFI_B, BFI_R and BFI_H were 48.9%, 74.0% and 50.0%, respectively. Figure 3-4 illustrates the poor fit of the R_{FM} model. A statistical analysis by the F-test, as was described earlier, indicated that the fit of the H_{DM} was significantly better than for the B_{DM} for all autocorrelation curves. No differences were observed in the extracted BFI values by

including more of the tail component of the correlation curves in the fitting routine (data not shown).

To further investigate the fits of the three DCS flow models, Figure 3-5 presents continuous BFI values during the transition from normocapnia to hypocapnia. The BFI was determined from autocorrelation curves generated every two seconds. The flow reductions measured by the three models were 34.1%, 54.6% and 34.6% for the B_{DM}, R_{FM} and H_{DM}, respectively.

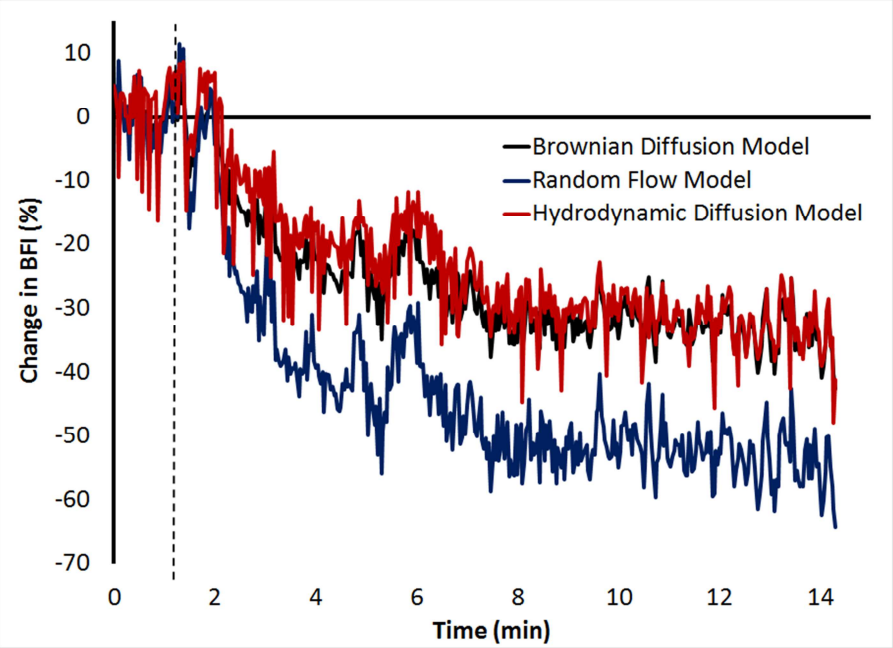

Figure 3-5: Real-time change of BFI measured during the transition from normocapnia to hypocapnia directly on the brain

Real-time change in BFI measured during the transition from normocapnia to hypocapnia in one pig. DCS data were acquired at a count rate of 780 ± 3 kHz and analyzed by each flow model. The dashed line represents the end of the normocapnic period before the respirator was adjusted to induce hypocapnia.

3.3.3 Computed Tomography Perfusion Comparison

Linear regression between the CBF change measured by CTP and the corresponding BFI change measured by each of the three DCS models was conducted on eight experiments after the outlier was removed (Figure 3-2). Also, linear regression between the CBF change measured by CTP and τ_c was conducted. The resulting regression slopes, intercepts and R-values are listed in Table 3-3.

Table 3-3: Linear relationship between CTP and corresponding DCS indices from different flow models

Parameter	Units	Slope ($CI_{95\%}$)	Intercept ($CI_{95\%}$)	R-value
BFI_B	cm^2/s	*1.03 ± 0.23 (0.54, 1.52)	-13.9 ± 12.1 (-39.9, 12.1)	0.78
BFI_R	cm^2/s	*1.24 ± 0.33 (0.52, 1.95)	-36.8 ± 17.7 (-74.8, 1.1)	0.70
BFI_H	cm^2/s	*1.66 ± 0.36 (0.89, 2.44)	-27.9 ± 19.1 (-68.9, 13.0)	0.78
τ_c	μs	*-0.030 ± 0.015 (-0.061, -0.001)	*4.86 ± 0.76 (3.24, 6.48)	0.46

Note: BFI_B, blood flow index determined by the DCS Brownian flow model; BFI_R, blood flow index determined by the DCS random flow model; BFI_H, blood flow index determined by the DCS hydrodynamic flow model; $CI_{95\%}$, 95% confidence intervals. Estimated slope and intercept (± SEM) for linear regression between CTP and BFI for each flow model along with the correlation coefficient (R) and p-values calculated by SPSS. * represents coefficients that are significantly different ($p<0.05$) from the null.

Table 3-3 demonstrates that the BFI values from each of the three models were correlated with CBF measured by CTP as indicated by a slope significantly different ($p<0.01$) from the null but a y-intercept not significantly different from zero. The displacement time constant τ_c, from the H_{DM} also correlated with CBF, but its R-value was not as strong and the y-intercept was significantly different from the zero.

Figure 3-6 presents the relative CBF decrease from normocapnia to hypocapnia as measured by CTP and DCS. The box-plot presents the results from all three DCS flow models, whereas only the results from the B_{DM} are presented in the Bland-Altman plot. In Figure 3-6A, the average CBF change measured by CTP was -39.7 ± 3.7%, which was only significantly different from the change in BFI_R (-63.2 ± 4.7%) and not from the BFI changes measured by the other two models (-41.0 ± 4.3% for BFI_B and -44.2 ± 5.0% for BFI_H). In Figure 3-6B, the mean difference between BFI_B and CTP, indicated by the solid line, was 9.0 ± 5.1%, which was not significant ($CI_{95\%}$: -19.1 and 37.0, as indicated by the two solid lines).

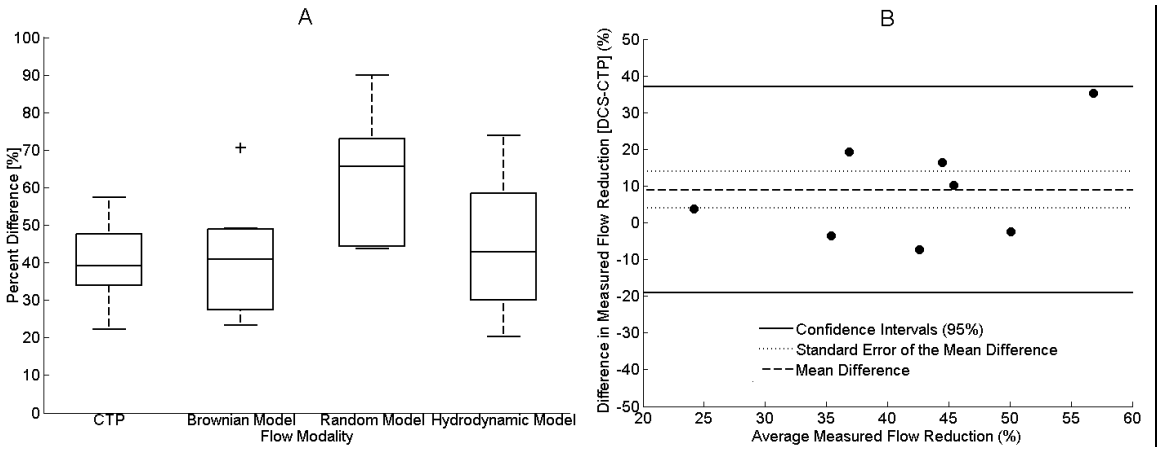

Figure 3-6: Comparison between the percent difference of CBF measured by CTP and different DCS flow models acquired on the exposed cortex of pigs

Flow percent differences measured by CTP and DCS directly on exposed cortical tissue. (A) Box plots of the reductions in flow from normocapnia to hypocapnia measured by CTP (N = 9) and the three DCS flow models (N = 10). The center line, box edges, error bars, and the cross represents the median, 1st and 3rd quartiles, $CI_{95\%}$, and outliers, respectively. (B) Bland-Altman plot comparing the reductions in CBF measured by CTP and BFI_B (N = 8). Each symbol represents a single animal. The mean difference between the two modalities, the standard error of the mean, and the $CI_{95\%}$ are indicated by the solid line, the dotted line and the dashed line, respectively.

In Figure 3-6B the animals that did not undergo CTP and the optical outlier for DCS were removed due to listwise deletion. For clarity, Table 3-4 summarizes all of the pigs in this study with their acquired modalities (CTP, TR NIRS and DCS) and SDD.

Table 3-4: A summary of all animals with acquired modalities.

Animal Number	CTP	TR NIRS	DCS	SDD [mm]
1	No	Yes	Yes	7
2	No	Yes	Yes	7
3	Yes	No (Unstable System)	Yes	7
4	Yes	No (Unstable System)	Yes	7
5	Yes	Yes	Yes	7
6	Yes	Yes	Yes	20
7	Yes	Yes	Yes	7
8*	Yes	Yes	Yes	7
9×	Yes	Yes	Yes	7
10	Yes	Yes (Identified Outlier)	Yes (Removed Outlier)	7
11^	Yes	Yes	Yes	7

Note: ×, * and ^ represents the animal used in Figure 3-1, Figure 3-4 and Figure 3-5, respectively. An unstable TR NIRS system occurred by an overheated detector prior to acquisitions. The identified outlier was described in detail above by Figure 3-2.

3.4 Discussion

The main aims of this study were to assess which DCS flow model best characterized 'brain' autocorrelation curves and to compare measured flow reductions obtained with the different models to an independent measure of CBF. These experiments were conducted with the optical probes placed directly on the exposed cortex in order to collect DCS data without any signal contamination from extracerebral tissues. To verify that the interrogated cortical region was relatively homogeneous with regards to blood flow, the autocorrelation curves were re-analyzed using only the early portion (i.e. between correlation times of 0.3 and ~10 μs) since this range is considered more sensitive to deeper propagating photons (Selb et al., 2014). No significant differences in blood flow indices were observed compared to the larger range of correlation times (0.6 μs to 1 ms) used in the Methods section, indicating that it was reasonable to consider the exposed cerebral cortex as a homogeneous medium (Verdecchia, Diop, & St. Lawrence, 2015).

Of the three models used to characterize normalized intensity autocorrelation functions, the hybrid model, H_{DM}, which accounts for both diffusive and ballistic motion, provided the best fit as determined by the F-test. This was evident at early correction times, which represents the transition from the ballistic to diffusion regime (Figure 3-4). This finding is in agreement with Carp et al., who found that the H_{DM} provided a superior fit to DCS data acquired from premature infants (Carp et al., 2011). The additional constant τ_c, which represents the time scale to transition from ballistic to diffusive motion, was found to be significantly greater (~29%) at hypocapnia compared to normocapnia. This inverse relationship with CBF would be expected considering that within a given period fewer interactions between RBCs within a vessel would occur as flows decreases. Despite the better fit provided by the H_{DM}, differences in blood flow indices from this model and the more commonly used B_{DM} were small. No significant differences were observed between the two models in terms of absolute BFI values and relative changes. This agreement indicates that the ballistic range of photons detected by DCS is relatively small, suggesting that most detected photons undergo correlated scattering events (i.e. scattering events occurring within a single vessel).

A practical limitation with using the H_{DM} is the addition of an extra fitting parameter, τ_c, which leads to a greater sensitivity to noise in the measured autocorrelation curves. This was demonstrated visually by the continuous monitoring example shown in Figure 3-5, in which data were acquired every two seconds. To characterize the noise sensitivity of each model, the coefficient of variation of the BFI over the baseline period was computed. The coefficient for BFI_H was 38.5% larger than for BFI_B. Furthermore, the linear regression analysis between the blood flow indices and CBF measurements from CTP showed less uncertainty and a tighter confidence interval range for the B_{DM} than the H_{DM} (Table 3-3). Therefore, the B_{DM} model, which is more robust and provides similar BFI measurements to the H_{DM}, is the more practical model to use, particularly for data with a lower signal-to-noise ratio, such as the real-time DCS monitoring displayed in Figure 3-5.

For the second aim of this study, CTP was used to measure CBF at normocapnia and hypocapnia. The latter causes a substantial reduction in CBF because of the tight coupling between cerebrovascular tone and arterial blood carbon dioxide tension. Hypocapnia rather than hypercapnia was used in these experiments because decreases in blood flow are clinically relevant to the management of critical care patients due to the incidence of delayed cerebral ischemia. Flow reductions caused by hypocapnia are not as great as caused by ischemia; however, the good agreement with the CTP results is further evidence of the ability of DCS to measure CBF changes accurately. The cerebral vascular reactivity measured with the B_{DM} was (-2.3 ± 0.2)% per mmHg of $paCO_2$, which is in good agreement with our previous study, which used the same animal model (juvenile pigs) and a contrast-enhanced NIRS technique to measure CBF (Elliott et al., 2014). Likewise, these findings confirm previous validation studies involving both animal models and human subjects that have shown a good correlation between BFI_B and CBF changes measured by other modalities (Yu et al., 2007; Zhou et al., 2006). Considering that the DCS data in the current study were collected directly on the brain, this agreement is evidence that DCS is relatively insensitive to extracerebral signal contamination in applications in which the scalp and skull are thin. These would include animal models, such as piglets and rats (Carp et al., 2010; Diop et al., 2011), but more importantly, also

applies to newborns (Diop, Kishimoto, Toronov, Lee, & Lawrence, 2015; Jain et al., 2014).

A possible limitation with this study is the potential for CTP to overestimate CBF due to the presence of pixels with extremely high flow estimates. These 'vascular' pixels are attributed to high contrast enhancement in vessels and were removed in the current study by setting perfusion thresholds (Murphy et al., 2006). This procedure has been shown to significantly improve the correlation with CBF measurements from positron emission tomography (Kudo et al., 2003) and from magnetic resonance imaging (Koziak, Winter, Lee, Thompson, & St. Lawrence, 2008). Another potential limitation was the possibility of variations in CBF between measurements from the different modalities. To minimize this, $paCO_2$ was monitored frequently to ensure it remained stable during each capnic level.

3.5 Conclusion

In summary, contributions from the superficial layers (scalp and skull) were eliminated by exposing the cerebral cortex of juvenile pigs and acquiring DCS directly on the brain. In agreement with Carp et al., the flow model that demonstrated the best fit to the intensity autocorrelation functions was the hybrid flow model, as evident at early correlation times. However, BFI values from the B_{DM} and the H_{DM} were very similar and both were in agreement with the CBF changes measured by CTP, indicating that the diffusion-like flow of erythrocytes dominates. Furthermore, the B_{DM} is the more practical model for characterizing DCS data due to its greater robustness.

3.6 References

Altman, D., & Bland, J. (1983). Measurement in medicine: the analysis of method comparison studies. *Journal of the Royal Statistical Society. Series D (The Statistician)*, *32*(3), 307–317. Retrieved from http://www.jstor.org/stable/10.2307/2987937

Binzoni, T., & Martelli, F. (2015). Assessing the reliability of diffuse correlation spectroscopy models on noise-free analytical Monte Carlo data. *Applied Optics*, *54*(17), 5320–5326. doi:10.1364/AO.54.005320

Boas, D., Campbell, L., & Yodh, A. G. (1995). Scattering and imaging with diffusing temporal field correlations. *Physical Review Letters*, *75*(9), 1855–1858. Retrieved from http://link.aps.org/doi/10.1103/PhysRevLett.75.1855

Boas, D., & Franceschini, M. A. (2011). Haemoglobin oxygen saturation as a biomarker: the problem and a solution. *Philosophical Transactions. Series A, Mathematical, Physical, and Engineering Sciences*, *369*(1955), 4407–24. doi:10.1098/rsta.2011.0250

Boas, D., & Yodh, A. G. (1997). Spatially varying dynamical properties of turbid media probed with diffusing temporal light correlation. *Journal of the Optical Society of America A*, *14*(1), 192–215. doi:10.1364/JOSAA.14.000192

Carp, S. A., Dai, G. P., Boas, D., Franceschini, M. A., & Kim, Y. R. (2010). Validation of diffuse correlation spectroscopy measurements of rodent cerebral blood flow with simultaneous arterial spin labeling MRI; towards MRI-optical continuous cerebral metabolic monitoring. *Biomedical Optics Express*, *1*(2), 553–565. doi:10.1364/BOE.1.000553

Carp, S. A., Roche-Labarbe, N., Franceschini, M. A., Srinivasan, V. J., Sakadžić, S., & Boas, D. (2011). Due to intravascular multiple sequential scattering, Diffuse Correlation Spectroscopy of tissue primarily measures relative red blood cell motion within vessels. *Biomedical Optics Express*, *2*(7), 2047–54. doi:10.1364/BOE.2.002047

Cenic, A., Nabavi, D. G., Craen, R. a, Gelb, a W., & Lee, T. Y. (1999). Dynamic CT measurement of cerebral blood flow: a validation study. *American Journal of Neuroradiology*, *20*(1), 63–73. Retrieved from http://www.ncbi.nlm.nih.gov/pubmed/9974059

Cheung, C., Culver, J. P., Takahashi, K., Greenberg, J. H., & Yodh, A. G. (2001). In vivo cerebrovascular measurement combining diffuse near-infrared absorption and correlation spectroscopies. *Physics in Medicine and Biology*, *46*(8), 2053–65. Retrieved from http://www.ncbi.nlm.nih.gov/pubmed/11512610

Dietsche, G., Ninck, M., Ortolf, C., Li, J., Jaillon, F., & Gisler, T. (2007). Fiber-based multispeckle detection for time-resolved diffusing-wave spectroscopy: characterization and application to blood flow detection in deep tissue. *Applied Optics*, *46*(35), 8506–8514. doi:10.1364/AO.46.008506

Diop, M., Kishimoto, J., Toronov, V., Lee, D. S. C., & Lawrence, K. S. (2015). Development of a combined broadband near-infrared and diffusion correlation system for monitoring cerebral blood flow and oxidative metabolism in preterm infants. *Biomedical Optics Express*, *6*(10), 3907–3918. doi:10.1364/BOE.6.003907

Diop, M., Tichauer, K. M., Elliott, J. T., Migueis, M., Lee, T.-Y., & St. Lawrence, K. (2010). Comparison of time-resolved and continuous-wave near-infrared techniques for measuring cerebral blood flow in piglets. *Journal of Biomedical Optics*, *15*(5), 057004. doi:10.1117/1.3488626

Diop, M., Verdecchia, K., Lee, T.-Y., & St Lawrence, K. (2011). Calibration of diffuse correlation spectroscopy with a time-resolved near-infrared technique to yield absolute cerebral blood flow measurements. *Biomedical Optics Express*, *2*(7), 2068. doi:10.1364/BOE.2.002068

Durduran, T., Choe, R., Baker, W. B., & Yodh, A. G. (2010). Diffuse optics for tissue monitoring and tomography. *Reports on Progress in Physics*, *73*(7), 076701. doi:10.1088/0034-4885/73/7/076701

Durduran, T., & Yodh, A. G. (2014). Diffuse correlation spectroscopy for non-invasive, micro-vascular cerebral blood flow measurement. *NeuroImage*, *85 Pt 1*, 51–63. doi:10.1016/j.neuroimage.2013.06.017

Elliott, J. T., Diop, M., Morrison, L. B., D'Esterre, C. D., Lee, T.-Y., & St Lawrence, K. (2014). Quantifying cerebral blood flow in an adult pig ischemia model by a depth-resolved dynamic contrast-enhanced optical method. *NeuroImage*, *94C*, 303–311. doi:10.1016/j.neuroimage.2014.03.023

Gagnon, L., Desjardins, M. 'R., Jehanne-Lacasse, J., Bherer, L., & Lesage, F. Ú. Ú. (2008). Investigation of diffuse correlation spectroscopy in multi-layered media including the human head. *Optics Express*, *16*(20), 15514–15530. Retrieved from http://www.opticsinfobase.org/abstract.cfm?id=172103

Gisler, T., Rüger, H., Egelhaaf, S. U., Tschumi, J., Schurtenberger, P., & Rička, J. (1995). Mode-selective dynamic light scattering: theory versus experimental realization. *Applied Optics*, *34*(18), 3546–53. Retrieved from http://www.ncbi.nlm.nih.gov/pubmed/21052170

Haskell, R. C., Svaasand, L. O., Tsay, T. T., Feng, T. C., McAdams, M. S., & Tromberg, B. J. (1994). Boundary conditions for the diffusion equation in radiative transfer. *Journal of the Optical Society of America. A, Optics, Image Science, and Vision*, *11*(10), 2727–2741.

Irwin, D., Dong, L., Shang, Y., Cheng, R., Kudrimoti, M., Stevens, S. D., & Yu, G. (2011). Influences of tissue absorption and scattering on diffuse correlation spectroscopy blood flow measurements. *Biomedical Optics Express*, *2*(7), 1969–85. doi:10.1364/BOE.2.001969

Jain, V., Buckley, E. M., Licht, D. J., Lynch, J. M., Schwab, P. J., Naim, M. Y., … Wehrli, F. W. (2014). Cerebral oxygen metabolism in neonates with congenital heart disease quantified by MRI and optics. *Journal of Cerebral Blood Flow and Metabolism : Official Journal of the International Society of Cerebral Blood Flow and Metabolism*, *34*(3), 380–8. doi:10.1038/jcbfm.2013.214

Kim, M. N., Durduran, T., Frangos, S., Edlow, B. L., Buckley, E. M., Moss, H. E., … Kofke, W. A. (2010). Noninvasive measurement of cerebral blood flow and blood oxygenation using near-infrared and diffuse correlation spectroscopies in critically brain-injured adults. *Neurocritical Care*, *12*(2), 173–80. doi:10.1007/s12028-009-9305-x

Koziak, A. M., Winter, J., Lee, T. Y., Thompson, R. T., & St. Lawrence, K. S. (2008). Validation study of a pulsed arterial spin labeling technique by comparison to

perfusion computed tomography. *Magnetic Resonance Imaging*, *26*(4), 543–553. doi:10.1016/j.mri.2007.10.005

Kudo, K., Terae, S., Katoh, C., Oka, M., Shiga, T., Tamaki, N., & Miyasaka, K. (2003). Quantitative cerebral blood flow measurement with dynamic perfusion CT using the vascular-pixel elimination method: comparison with H2(15)O positron emission tomography. *AJNR. American Journal of Neuroradiology*, *24*(3), 419–426.

Lemieux, P., & Durian, D. (1999). Investigating non-Gaussian scattering processes by using nth-order intensity correlation functions. *Journal of the Optical Society of America A*. doi:10.1364/JOSAA.16.001651

Mesquita, R. C., Durduran, T., Yu, G., Buckley, E. M., Kim, M. N., Zhou, C., … Yodh, A. G. (2011). Direct measurement of tissue blood flow and metabolism with diffuse optics. *Philosophical Transactions. Series A, Mathematical, Physical, and Engineering Sciences*, *369*, 4390–406. doi:10.1098/rsta.2011.0232

Murphy, B. D., Fox, a J., Lee, D. H., Sahlas, D. J., Black, S. E., Hogan, M. J., … Lee, T.-Y. (2006). Identification of penumbra and infarct in acute ischemic stroke using computed tomography perfusion-derived blood flow and blood volume measurements. *Stroke; a Journal of Cerebral Circulation*, *37*(7), 1771–7. doi:10.1161/01.STR.0000227243.96808.53

Ninck, M., Untenberger, M., & Gisler, T. (2010). Diffusing-wave spectroscopy with dynamic contrast variation: disentangling the effects of blood flow and extravascular tissue shearing on signals from deep tissue. *Biomedical Optics Express*, *1*(5), 1502–1513. doi:10.1364/BOE.1.001502

Ntziachristos, V., & Chance, B. (2001). Accuracy limits in the determination of absolute optical properties using time-resolved NIR spectroscopy. *Medical Physics*, *28*(6), 1115. doi:10.1118/1.1373674

Selb, J., Boas, D. a., Chan, S.-T., Evans, K. C., Buckley, E. M., & Carp, S. a. (2014). Sensitivity of near-infrared spectroscopy and diffuse correlation spectroscopy to brain hemodynamics: simulations and experimental findings during hypercapnia. *Neurophotonics*, *1*(1), 015005. doi:10.1117/1.NPh.1.1.015005

Verdecchia, K., Diop, M., Lee, A., & St. Lawrence, K. (2015). Characterization of a hybrid diffuse correlation spectroscopy and time-resolved near-infrared spectroscopy system for real-time monitoring of cerebral blood flow and oxygenation. In A. Mahadevan-Jansen, T. Vo-Dinh, W. S. Grundfest, & Q. Liu (Eds.), (Vol. 9313, p. 931310). doi:10.1117/12.2079457

Verdecchia, K., Diop, M., Lee, T.-Y., & St. Lawrence, K. (2013). Quantifying the cerebral metabolic rate of oxygen by combining diffuse correlation spectroscopy and time-resolved near-infrared spectroscopy. *Journal of Biomedical Optics*, *18*(2), 027007. doi:10.1117/1.JBO.18.2.027007

Verdecchia, K., Diop, M., & St. Lawrence, K. (2015). Investigation of the best model to characterize diffuse correlation spectroscopy measurements acquired directly on

the brain. In A. Wax & V. Backman (Eds.), (Vol. 9333, p. 93330E). doi:10.1117/12.2079499

Weigl, W., Milej, D., Gerega, a., Toczylowska, B., Kacprzak, M., Sawosz, P., … Liebert, a. (2014). Assessment of cerebral perfusion in post-traumatic brain injury patients with the use of ICG-bolus tracking method. *NeuroImage*, *85*, 555–565. doi:10.1016/j.neuroimage.2013.06.065

Yu, G., Floyd, T. F., Durduran, T., Zhou, C., Wang, J., Detre, J. a, & Yodh, A. G. (2007). Validation of diffuse correlation spectroscopy for muscle blood flow with concurrent arterial spin labeled perfusion MRI. *Optics Express*, *15*(3), 1064–75. Retrieved from http://www.ncbi.nlm.nih.gov/pubmed/19532334

Zhou, C., Choe, R., Shah, N., Durduran, T., Yu, G., Durkin, A., … Yodh, A. G. (2007). Diffuse optical monitoring of blood flow and oxygenation in human breast cancer during early stages of neoadjuvant chemotherapy. *Journal of Biomedical Optics*, *12*(5), 051903. doi:10.1117/1.2798595

Zhou, C., Yu, G., Furuya, D., Greenberg, J., Yodh, A. G., & Durduran, T. (2006). Diffuse optical correlation tomography of cerebral blood flow during cortical spreading depression in rat brain. *Optics Express*, *14*(3), 1125–44. Retrieved from http://www.ncbi.nlm.nih.gov/pubmed/19503435

Chapter 4

4 Measurements of Cerebral Blood Flow in Adolescent Pigs by Diffuse Correlation Spectroscopy

This chapter is adapted from the paper entitled "Assessment of a multi-layered diffuse correlation spectroscopy method for monitoring cerebral blood flow in adults" by Verdecchia K, Diop M, Morrison L, Lee T-Y, St. Lawrence K, published in Biomedical Optics Express, vol. 7(9) (2016).

4.1 Introduction

Patients requiring intensive care due to life-threatening neurological emergencies, such as ischemic stroke, traumatic brain injury and subarachnoid hemorrhage, are at high risk of secondary brain injury (De Oliveira Manoel et al., 2015; English et al., 2013; Kirkman, Citerio, & Smith, 2014). Although multiple factors contribute to poor outcome, a major focus is preventing delayed cerebral ischemia. For example, approximately one-third of patients with subarachnoid hemorrhage will develop secondary brain injury within two weeks of the initial event primarily due to cerebral vasospasm (Al-Tamimi, Orsi, Quinn, Homer-Vanniasinkam, & Ross, 2010). Consequently, a major focus of neurointensive care is maintaining adequate cerebral blood flow (CBF) through treatments such as administering nimodipine, inducing hypertension, and intervening with surgical or pharmacological angioplasty (Macdonald, 2014). A key component of patient management is the use of monitoring techniques to detect signs of impaired CBF, such as elevated flow velocities in cerebral arteries as measured by transcranial Doppler. However, this is not a direct measure of CBF and cerebral ischemia can occur without evidence of arterial narrowing (Dhar et al., 2012). Cerebral blood flow can be monitored directly by thermal diffusion and laser Doppler flowmetry (Kirkpatrick, Smielewski, Czosnyka, & Pickard, 1994; Vajkoczy et al., 2000), but these are invasive methods, which has hindered their wider applicability. To date, there remains no established bedside technique capable of monitoring CBF.

Near-infrared spectroscopy (NIRS) is a portable, non-invasive technology that can be used to monitor cerebral oxygenation at the bedside of critical-care patients (Obrig & Steinbrink, 2011; Zweifel et al., 2010). Cerebral blood flow can be measured directly using the optical dye indocyanine green as an intravascular contrast agent (Brown et al., 2002; Steinkellner et al., 2010; Weigl et al., 2014). With the application of light propagation models to account for absorption in extracerebral tissues, this contrast-enhanced approach can also provide quantitative CBF measurements (Elliott et al., 2014), but it is limited to single time point measurements. An alternative approach is diffuse correlation spectroscopy (DCS) that monitors changes in CBF by detecting speckle patterns caused by the motion of red blood cells (Baker et al., 2014; Boas, Campbell, & Yodh, 1995; Buckley, Parthasarathy, Grant, Yodh, & Franceschini, 2014). A normalized intensity autocorrelation curve is determined from the measured temporal speckle pattern, and a blood flow index is obtained by fitting the autocorrelation curve with an analytical solution to the correlation diffusion equation for a semi-infinite homogeneous medium (Cheung, Culver, Takahashi, Greenberg, & Yodh, 2001). A number of validation studies involving alternative methods of measuring blood flow have shown that DCS can track perfusion changes in the brain accurately (Buckley et al., 2014; Durduran & Yodh, 2014). Modeling DCS data in this manner is reasonable if contributions from extracerebral tissues are small such as for neonates and certain animal models (Buckley et al., 2014; Diop, Kishimoto, Toronov, Lee, & Lawrence, 2015; Lin et al., 2013). However in the adult head, reflected light measured on the scalp must travel through more substantial extracerebral layers (i.e. scalp and skull), leading to partial volume errors and underestimations of CBF.

A number of approaches have been proposed to account for tissue heterogeneity when applying DCS to monitor CBF in adults, starting with the use of a correction factor based on partial volumes estimates (Durduran et al., 2004). Another approach is to weight the model fit to shorter correlation times since these represent longer photon pathlengths (i.e. photons that have a greater chance of having propagated deeper into tissue) (Baker et al., 2015; Selb et al., 2014). However, these methods can only enhance the sensitivity to CBF but do not completely separate the effects of light propagation and blood flow in the various tissues. A more direct approach is to adapt a multi-layered solution to the

diffusion approximation that accounts for the contribution of the extracerebral layers. Using Monte Carlo simulations and layered tissue phantom, this approach has been shown to improve the sensitivity to CBF (Gagnon, Desjardins, Jehanne-Lacasse, Bherer, & Lesage, 2008), and it has been used to analyze DCS data acquired from participants performing a functional task (Li et al., 2005). These studies highlight the importance of using a theoretical model that accounts for extracerebral tissue layers to improve sensitivity to cerebral tissue when analyzing DCS data acquired on the adult head.

The current study investigates the application of a multi-layered (ML) DCS model to data acquired at multiple source-detector distances with the aim of separating brain and scalp blood flow. Two sets of experiments were conducted to assess the improved depth sensitivity of the ML modeling approach. First, a two-layered tissue-mimicking phantom was constructed in which the pseudo-flow property of each layer could be independently altered. Data were acquired at two source-detector distances while the diffusion coefficient in the deeper layer was gradually increased. Second, the approach was applied to measuring CBF in a juvenile swine model, which was chosen because the thickness of the extracerebral layers is similar to that of the adult human head. Cerebral blood flow was reduced by altering blood CO_2 tension from normocapnia to hypocapnia. For validation, CBF was independently measured by computed tomography perfusion (CTP) (Elliott et al., 2014; Lee, 2002).

4.2 Theory

With DCS, the measured temporal intensity fluctuations are used to compute the normalized intensity autocorrelation function, $g_2(\rho,\tau)$ (Cheung et al., 2001):

$$g_2(\rho,\tau) \equiv \frac{\langle I(\rho,t)I(\rho,t+\tau)\rangle}{\langle I(\rho,t)\rangle^2} \tag{4.1}$$

where, $\langle I(\rho,t)\rangle$ is the light intensity measured by a detector located at a distance ρ from the source at time t, and τ is the correlation time. Equation 1 is related to the electric field autocorrelation function, $G_1(\rho,z,\tau) \equiv \langle E(\rho,z,\tau) \bullet E^*(\rho,z,t+\tau)\rangle$, by the Siegert relation (Lemieux & Durian, 1999):

$$g_2(\rho,\tau) = 1 + \beta \frac{|G_1(\rho,z,\tau)|^2}{\langle I(\rho,t)\rangle^2} \tag{4.2}$$

where, β is the coherence factor of the detection system. It has been shown for a high scattering, low-absorbing medium, such as tissue, that $G_1(\rho,z,\tau)$ can be modeled by the correlation diffusion equation at a depth z in the medium (Boas et al., 1995; Skipetrov & Maynard, 1996). By modeling the medium as a series of parallel slabs over a semi-infinite medium, the diffusion equation is given by (Boas et al., 1995; Skipetrov & Maynard, 1996):

$$P_i\left[\nabla^2 - {\mu_{P_i}}^2(\tau)\right]G_1(\rho,z,\tau) = -v S\delta(z - z_0) \tag{4.3}$$

where, $P_i = v/(3\mu_{ai} + 3\mu'_{si})$ is the photon diffusion coefficient in layer i, v is the speed of light, μ_{ai} is the absorption coefficient and μ'_{si} is the reduced scattering coefficient. S is the light source defined at an effective depth z_0 ($= 1/\mu'_{s1}$) by the delta function $\delta(z - z_0)$. Finally, μ_{Pi} accounts for the loss of correlation due to dynamical processes (i.e. the motion of scatterers) and is given by:

$$\mu_{P_i}^2(\tau) = \frac{3v}{P_i}\left(\mu_{a_i} + 2\mu'_{s_i}k_0^2\alpha D_i\tau\right) \tag{4.4}$$

where, $k_0 = 2\pi n/\lambda$ is the wavenumber of light (λ is wavelength and n is the refractive index, which is set to 1.4 for all tissues), α represents the fraction of scattering events related to motion, which in tissue represents the fractional blood volume, and D_i is the diffusion coefficient of the i^{th} layer. If blood flow is modeled as a pseudo-Brownian process (Cheung et al., 2001), which is valid for brain (Verdecchia, Diop, Morrison, Lee, & St. Lawrence, 2015), then the blood flow index, F_i, is given by αD_i.

Modeling tissue as a semi-infinite homogeneous medium, the analytical solution to Equation 4.3 is given as [16,18]:

$$G_1(\rho,z,\tau) = \frac{3\mu'_{s_i}}{4\pi}\left[\frac{\exp(-\mu_{P_1}r_1)}{r_1} - \frac{\exp(-\mu_{P_1}r_1)}{r_2}\right] \tag{4.5}$$

where, $r_1 = [\rho^2 + {z_0}^2]^{1/2}$, $r_2 = [\rho^2 + (z_0 + 2z_b)^2]^{1/2}$, and z_b is the extrapolated boundary defined by $2P_1(1 + R_{eff})(1 - R_{eff})^{-1}$ (Kienle & Glanzmann, 1999). The effective reflection

coefficient, R_{eff}, is given by 0.493 for the refraction indices of tissue and air (Haskell et al., 1994). In the general case consisting of parallel slabs on a semi-infinite medium, the field autocorrelation function at the surface (i = 0), $\tilde{G}_1^0(s,z,\tau)$, can be determined by solving Equation 4.3 in the Fourier domain (Li et al., 2005):

$$\tilde{G}_1^0(s,z,\tau) = \int G_1^0(\rho,z,\tau)e^{is\rho}d^2\rho \tag{4.6}$$

Similar to Li et al., the appropriate boundary conditions were applied to $G_1^0(\rho,z,\tau)$, which is obtained by numerically computing the inverse Fourier transform of $\tilde{G}_1^0(s,z,\tau)$ at the surface (Gagnon et al., 2008; Li et al., 2005):

$$G_1^0(\rho,z,\tau) = \frac{1}{2\pi}\int_0^\infty \tilde{G}_1^0(s,z=0,\tau)sJ_0(s\rho)ds \tag{4.7}$$

where s is the radial spatial frequency, J_0 is the Bessel function of zeroth order computed by the MATLAB function *besselj* and the solution of $\tilde{G}_1^0(s,z,\tau)$. The Hankel transform in Equation 4.7 was computed numerically by rearranging the solution for a three-layered model to the form of the Gauss-Laguerre quadrature in MATLAB:

$$\tilde{G}_1^0(s,z,\tau) = \frac{\text{numerator}}{\text{denominator}} \tag{4.8}$$

$$\begin{aligned}\text{numerator} = {} & S(0,z-z_b) \\ & \times z_0\left\{\tilde{\mu}_{P_1}P_1\cosh\left(\tilde{\mu}_{D_1}(L_1-z_b)\right)\left[\tilde{\mu}_{P_2}P_2\cosh\left(\tilde{\mu}_{P_2}L_2\right)\right.\right. \\ & \left. + \tilde{\mu}_{P_3}P_3\sinh\left(\tilde{\mu}_{P_2}L_2\right)\right] \\ & \left. + \tilde{\mu}_{P_2}P_2\sinh\left(\tilde{\mu}_{P_1}(L_1-z_b)\right)\left[\tilde{\mu}_{P_3}P_3\cosh\left(\tilde{\mu}_{P_2}L_2\right)+\tilde{\mu}_{P_2}P_2\sinh\left(\tilde{\mu}_{P_2}L_2\right)\right]\right\}\end{aligned}$$

$$\begin{aligned}\text{denominator} = \; & \tilde{\mu}_{P_2} P_2 \cosh\left(\tilde{\mu}_{P_2} L_2\right) \left[\tilde{\mu}_{P_1} \cosh\left(\tilde{\mu}_{P_1} L_1\right) \left(P_1 + \tilde{\mu}_{P_3} P_3 z_0\right)\right. \\ & + \sinh\left(\tilde{\mu}_{P_1} L_1\right) \left(\tilde{\mu}_{P_3} P_3 + \tilde{\mu}_{P_1}^2 P_1 z_0\right)\Big] \\ & + \sinh\left(\tilde{\mu}_{P_2} L_2\right) \Big[\tilde{\mu}_{P_1} \cosh\left(\tilde{\mu}_{P_1} L_1 \left(\tilde{\mu}_{P_3} P_1 P_3 + \tilde{\mu}_{P_2}^2 P_2^2 z_0\right)\right) \\ & + \sinh\left(\tilde{\mu}_{P_1} L_1\right) \left(\tilde{\mu}_{P_2}^2 P_2^2 + \tilde{\mu}_{P_1}^2 \tilde{\mu}_{P_3} P_1 P_3 z_0\right)\Big]\end{aligned}$$

where, $\tilde{\mu}_{Pi}^2(s,\tau) = \mu_{Pi}^2(\tau) + s^2$ for the i^{th} layer, and L_1 and L_2 are the thicknesses of the first and second tissue layers (i.e. scalp and skull, respectively); the third layer is brain, which is assumed to be infinitely thick.

4.3 Methods

4.3.1 Instrumentation

4.3.1.1 Hybrid Optical System

The light source of the DCS instrument was a continuous-wave laser (DL785-100-S, CrystalLaser, Nevada) emitting at 785 nm with a maximum output power of 100 mW and a coherence length >5 m. The emitted light was attenuated by electronically controlled variable neutral density filters and coupled to a multimode emission fiber (N.A. = 0.22, core = 400 µm; Fiberoptics Technology, Pomfret, CT). Twelve single-mode fibers (SMF-28e +, N.A. = 0.14, length = 4 m, core = 8.2 µm, single-mode cutoff wavelength at 1260 nm) were split into separate fiber bundles located at source-detector distances (SDDs) of 20 and 27 mm. Due to the considerable drop in light intensity with distance, one fiber was placed at 20 mm and the remaining 11 were placed at 27 mm. Each fiber was coupled to the input of a single photon counting module (SPCM-AQ4C, Excelitas Canada Inc). The output of each SPCM was sent to a 16-channel photon correlator board (DPC-230, Beker & Hickl) that computed the normalized intensity autocorrelation functions, $g_2(\rho,\tau)$.

Tissue optical properties (i.e. μ_a and μ_s') were measured by a TR NIRS system described in detail elsewhere, (Diop et al., 2010; Verdecchia et al., 2015). Briefly, the

instrument consisted of a picoseconds pulsed diode laser (LDH-P-C 764, PicoQuant, Germany) emitting at 764 nm with an average output power and pulse repetition rate of 1.4 mW and 80 MHz, respectively. The light was guided by the same type of optical fiber as the DCS emission probe; the two probes were bundled together to emit light at the same location. The pulsed light was detected by 121 optical fibers (core = 200 µm, cladding = 220 µm, N.A. = 0.22, length = 0.5 m), which were bundled together with the 11 DCS single-mode detection fibers located at the SDD of 27 mm. Collected photons were guided to a fast hybrid photomultiplier detector (PMA Hybrid, PicoQuant, Germany) whose output was sent to a time-correlated single-photon counting (TCSPC) module (HydraHarp 400, PicoQuant, Germany). At the end of the study, the instrument response function (IRF) was measured to account for instrument-related temporal dispersion (Ntziachristos & Chance, 2001).

4.3.1.2 Computed Tomography Perfusion

All CT imaging was performed with a Revolution CT scanner (General Electric Company, Waukesha, WI). Perfusion images were acquired by performing a dynamic contrast-enhanced protocol, which involved serial acquisition of image volumes, one acquired every second, for 40 seconds (200 mA, 80 kVp, 2.5-mm slice thickness, and a FOV of 140 x 140 x 40 mm). Each volume consisted of 32 coronal slices, which encompassed the entire head. The beginning of the dynamic scanning was immediately followed by a bolus injection of 1.0 mL/kg of iodine-based contrast agent (iopamidol [370-Isovue®], Bracco S.p.A., Milan, Italy) at a rate of 3 mL/s into the cephalic vein.

4.3.2 Experimental Procedure

4.3.2.1 Two-Layered Diffusion Phantom Experiment

A two-layered phantom was designed using computer-aided 3D drawing software (Rhinoceros 5; Robert McNeel & Associates, North America). It was constructed from dark polyvinyl chloride (12 mm thick) and had internal dimensions of 180 x 140 x 110 mm. Two layers were created by inserted a polyester Mylar sheet (polyethylene terephthalate; McMaster-Carr) with a thickness of 25.4 µm. The Mylar sheet was framed by a clear polycarbonate that could be positioned at a depth of either 5 or 10 mm from the

top of the box. Three holes were drilled into the top of the box to hold the probes in place: one emission fiber and two detection fibers at SDDs of 20 and 30 mm. To mimic the light scattering properties of tissue, both layers were filled with 0.8% Intralipid (Fresenius Kabi, Germany). The viscosity in the bottom layer was increased by adding methyl cellulose (4000 cP; Sigma-Aldrich, St. Louis, MO) (Cheung et al., 2001).

To replicate the homogeneous condition, DCS data were first acquired at a SDD of 30 mm and multiple cellulose concentrations (0, 0.05, 0.1, 0.15, and 0.2%), but without the Mylar membrane. In addition to acquiring DCS data, μ_a and μ_s' were measured by TR NIRS at each cellulose concentration. Next, the membrane was inserted to create a top layer with a thickness of 5 or 10 mm. DCS data were acquired at 20 and 30 mm while increasing the cellulose concentration in the bottom layer from 0 to 0.2%, but maintaining the top-layer concentration at 0%. Data acquired with the homogeneous phantom were analyzed by the analytical solution (Equation 4.5) for the homogeneous model (DCS_{HM}). Data acquired with the two-layered phantom were analyzed with DCS_{HM} (SDD = 30 mm) and ML DCS method using data from both separations.

4.3.2.2 Animal Experiments

Experiments were conducted under the guidelines of the Canadian Council of Animal Care (CCAC) and approved by the Animal Use Sub-Committee at Western University. The animals were obtained from a local supplier on the day of the experiment. Following anesthetic induction with 5% isoflurane, the animals were tracheotomized and mechanically ventilated on a mixture of oxygen and medical air. A catheter was inserted into a femoral artery for blood gas analysis. After surgery, isoflurane was reduced to 3-4% and the animal was transported to the CT suite where the experiments were conducted.

Before data collection, CT scout images were acquired to determine the best location for the probe holder on the head (i.e. the position corresponding to the largest brain diameter). During the experiment, arterial oxygen saturation, heart rate (HR), respiratory rate, mean arterial pressure (MAP), and rectal temperature were continuously monitored. Arterial blood samples were obtained to measure arterial pH, the arterial

partial pressure of carbon dioxide ($paCO_2$), the arterial partial pressure of oxygen (paO_2), the concentration of blood glucose (BG), and the total blood hemoglobin concentration (ctHb). Samples were acquired before and after each set of measurements to assess physiological stability during data acquisition. The order for the three modalities was CTP, TR NIRS, and DCS at normocapnia ($paCO_2$ between 38 and 42 mmHg) and reversed at hypocapnia ($paCO_2$ between 20 and 25 mmHg) to avoid removing the DCS probes from the head between measurements. Each capnic level was maintained by adjusting the ventilation volume and rate. To investigate if the multi-distance DCS measurements were affected by scalp blood flow, the acquisition protocol was repeated after creating incisions in the scalp around three lateral sides of the probe holder to reduce scalp blood flow (Elliott et al., 2014).

4.3.3 Data Analysis

4.3.3.1 Computed Tomography Perfusion

Maps of CBF were calculated using the CT perfusion software package PERFUSION 5 (GE Healthcare Worldwide), which was developed and validated in-house (Cenic, Nabavi, Craen, Gelb, & Lee, 1999). Region-of-interest (ROI) analysis was performed using in-house developed software that performed pixel thresholding to remove signal contributions from large vessels that can lead to CBF overestimations (Murphy et al., 2006). For each slice, three ROI's (~5 cm^2) were manually drawn on the scalp, skull, and cerebral cortex, as seen in Figure 4-1. The location of the scalp ROI was located laterally to the actual positions of the DCS probes. This was done to avoid motion artifacts near tissue interfaces such as bone and scalp caused by breathing. The brain ROI was drawn on the cerebral cortex since the NIRS signal is more sensitive to superficial brain tissue than deeper white matter. Absolute blood flow values for each of the three tissues (scalp, skull and brain) were obtained by averaging ROIs across ten to twelve sequential slices. Finally, the thicknesses of the scalp and the skull (i.e. L_1 and L_2, respectively) were measured by image-viewing software (AW VolumeShare 4, GE Healthcare).

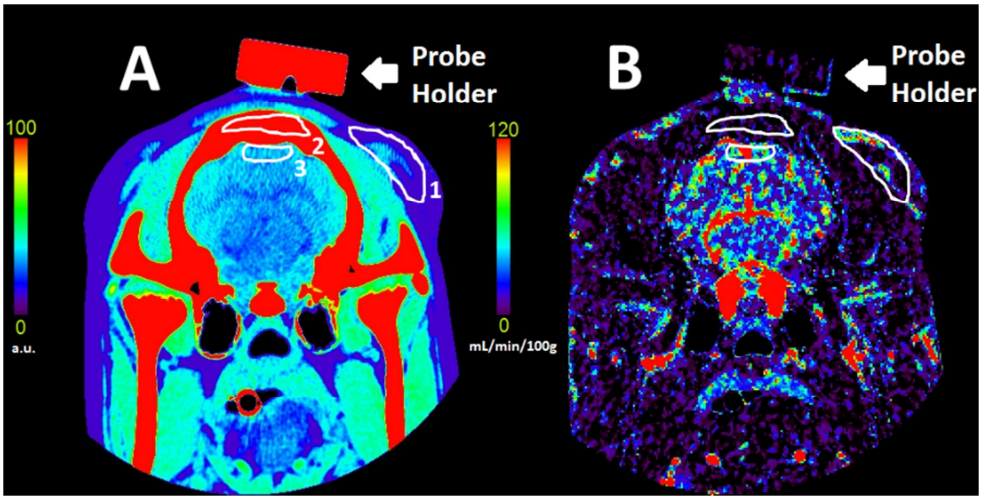

Figure 4-1: Single slice of the intact head of a pig: anatomical and perfusion map CT images

Coronal CT image of a pig's head (A) and the corresponding blood flow map (B). The scalp (1), skull (2) and brain (3) ROIs are shown in white. Bar codes are given to illustrate relative x-ray attenuation (A) and blood flow in mL/min/100g (B).

4.3.3.2 Diffuse Correlation Spectroscopy

All intensity autocorrelation functions were acquired over an integration time between 30 and 90 s depending on the achieved count rate. Measured $g_2(\rho,\tau)$ functions were converted to the field autocorrelation function by Equation 4.2. Data were analyzed using both solutions to the diffusion approximation: the semi-infinite homogeneous model (Equation 4.5) and the ML model (Equations 4.6 and 4.7). Estimates of the diffusion coefficients were determined using a non-linear least squares fitting routine (MATLAB© function *fminsearchbnd* with D_i values constrained to be positive) to fit an analytical model to $g_2(\rho,\tau)$. For the homogeneous model, data from one SDD were analyzed to generate a diffusion coefficient for the tissue-mimicking phantom or a blood flow index denoted F_{HM} for the in vivo data. These values were derived using the values of μ_a and μ_s' measured by TR NIRS, which were also determined by the solution to the diffusion approximation for a semi-infinite homogeneous medium (Diop, Verdecchia, Lee, & St Lawrence, 2011). The fitting was performed for correlation times from 1 μs up to times corresponding to $g_1(\rho,\tau) > 0.5$, since focusing the fit of the autocorrelation function to short correlation times increases the sensitivity to deeper propagating photons (Selb et al.,

2014). For the animal experiments the $g_2(\rho,\tau)$ functions acquired at 20 and 27 mm were analyzed separately and denoted $F_{HM,1}$ and $F_{HM,2}$, respectively.

For the ML DCS model, the $g_2(\rho,\tau)$ functions acquired at the two SDDs were analyzed simultaneously. The μ_a and μ_s' values for all three layers were set to the values obtained from TR NIRS using the homogeneous model, and L_1 and L_2 values were obtained from the CT images. For each animal, the coherence factor (β) was estimated prior to the fitting by averaging the first five points of each autocorrelation function. To focus on deeper propagating photons, the fitting was performed between correlation times defined by $g_2(\rho,\tau) < 0.8$ to 0.1 s for the shorter SDD (20 mm), and 1 μs to $g_2(\rho,\tau) > 0.5$ for the longer SDD (27 mm). For the flow phantom, the two fitting parameters were the diffusion coefficients in the top and bottom layers (D_T and D_B, respectively). Similarly, the fitting parameters for the analysis of the in vivo data were the blood flow indices in scalp and brain (denoted F_S and F_B, respectively), assuming negligible flow in the middle (skull) layer.

4.3.3.3 Statistical Analysis

Uncertainties are given as the standard error of the mean unless otherwise stated. All statistics were computed with the IBM SPSS Statistics 20 software package. For the phantom experiments, linear regression analysis was conducted to identify a significant relationship between increasing viscosity in the bottom layer and the measured diffusion coefficients (D_T and D_B).

For the animal experiments, possible changes in the measured physiological parameters and optical properties due to altering $paCO_2$ or the scalp incisions were tested by a repeated measures analysis of variance (ANOVA). The same test was conducted on all measured flow parameters, which include the blood flow estimates for scalp, skull and brain measured by CTP, and for the blood flow indices measured by DCS techniques: F_S and F_B from the ML DCS analysis, and $F_{HM,1}$ and $F_{HM,2}$ from the homogeneous model. Relative blood flow changes measured by CTP and ML DCS when $paCO_2$ was altered from normocapnia to hypocapina were compared by a paired t-test. Finally, Bland-Altman analysis was conducted to compare the reductions in CBF and F_B obtained by

CTP and ML DCS, respectively. This included a one-sample t-test to identify differences between the two modalities and linear regression to determine proportionality bias.

4.4 Results

4.4.1 Phantom Experiments

Figure 4-2 illustrates the relative change (i.e. from 0% cellulose) in the estimated diffusion coefficient from the homogeneous model (A) and the ML DCS model (B) as the viscosity in the bottom layer of the phantom was increased by adding cellulose. In the latter case, the diffusion coefficient from the bottom layer (D_B) is shown. For comparison, each graph also includes the measured change in the diffusion coefficient for the homogeneous phantom.

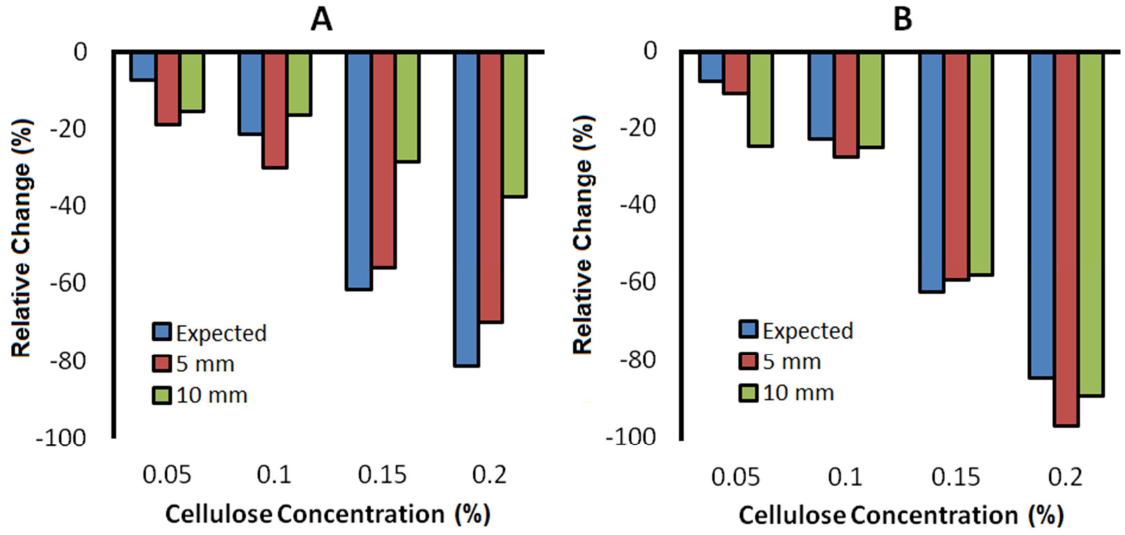

Figure 4-2: Relative change in the measured diffusion coefficient from the deepest layer of a multi-layered phantom: analyzed by homogeneous and heterogeneous DCS flow models

Relative change in the measured diffusion coefficient as the viscosity of the tissue-mimicking phantom was increased. The label 'expected' refers to the homogeneous case (blue bars), and the labels '5 mm' and '10 mm' refer to thickness of the top layer for the two-layered case (red and green bars, respectively). For the two-layered experiments, cellulose was only added to the bottom layer. (A) Diffusion coefficient determined by analyzing the two-layered data with the homogeneous model (SDD = 30 mm). (B) Diffusion coefficient for the bottom layer of a two-layered model applied to the same data used in (A). This analysis used data acquired at SDD of 20 and 30 mm.

The results in Figure 4-2A were obtained using the HM-DCS model to characterize the $g_2(\rho,\tau)$ curves acquired at a SDD of 30 mm, and as expected the magnitude of the error was larger as the top layer thickness increased. The results in Figure 4-2B were obtained using the ML DCS model to characterize $g_2(\rho,\tau)$ acquired at SDDs of 20 and 30 mm. Linear regression analysis indicated that increasing the viscosity in the bottom layer significantly reduced D_B, but had no effect on D_T for either a 5 or 10 mm thick top layer. The optical properties measured by TR NIRS in the homogeneous phantom were $\mu_a = 0.033 \pm 0.003$ cm^{-1} and $\mu_s' = 8.5 \pm 0.2$ cm^{-1}.

4.4.2 Animal Experiments

4.4.2.1 Physiological Experiments

Experiments were conducted on seven pigs (all female) with an average weight of 15.5 ± 0.4 kg and average scalp and skull thicknesses of 3.5 ± 0.2 mm and 6.4 ± 0.4 mm, respectively. For all physiological parameters, significant differences were observed pre- and post-scalp incision, except for pH, $paCO_2$ and paO_2.

As expected, significant differences between normocapnia and hypocapnia were observed for pH and $paCO_2$ [$p<0.001$, partial-$\eta^2 > 0.98$, Power = 1]; however, a significant change in paO_2 and MAP were also observed [$p<0.05$, partial-$\eta^2 > 0.69$, Power > 0.85] (see Table 4-1). Significant changes were not observed for any of the other measured physiological parameters. Their mean values were 38.4 ± 0.1 °C (temperature), 120 ± 2 beats per minute (HR), 5.3 ± 0.2 mmol/L (BG) and 9.2 ± 0.1 g/dL (ctHb). Lastly, no differences were observed in μ_a (0.168 ± 0.008 cm^{-1}) and μ_s' (9.0 ± 0.8 cm^{-1}) between capnic conditions.

Table 4-1: Physiological parameters during normocapnia and hypocapnia

Condition	*pH	*$paCO_2$ (mmHg)	*paO_2 (mmHg)	*MAP (mmHg)
Normocapnia	7.473 ± 0.006	39.5 ± 0.4	173 ± 10	41 ± 1
Hypocapnia	7.658 ± 0.006	22.2 ± 0.4	210 ± 10	38 ± 1

Average values at normocapnia and hypocapnia for the arterial partial pressure of carbon dioxide ($paCO_2$,) and oxygen (paO_2). * $p<0.05$ between conditions. Data are presented as average ± SEM.

4.4.2.2 Absolute Blood Flow

Five blood flow index sets (F_S and F_B) measured by ML DCS out of a total of 28 were removed due to either a large residue (i.e. > 0.01) in the optimization procedure (two cases) or an F_B value that approached zero (i.e. < 10^{-9}) (one case). Lastly, both sets of $g_2(\rho,\tau)$ curves (i.e. during normocapnia and hypocapnia) from one experiment were removed due to poor coupling between the optical probes and skin.

Normalized intensity autocorrelation curves from one experiment are plotted in Figure 4-3. This set was chosen as the F_B values at normo- and hypo-capnia were similar

to the average values across all animals. The shift to longer correlations times from normocapnia to hypocapnia evident in Figure 4-3 represents a -38.7 % flow change measured by ML DCS.

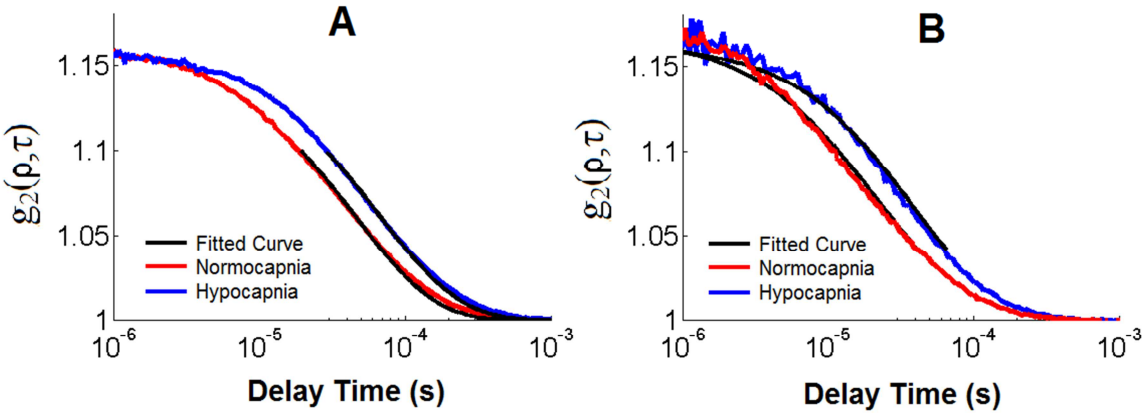

Figure 4-3: Measured DCS decay curves acquired on the intact head of a pig during normocapnia and hypocapnia

Normalized intensity autocorrelation functions acquired during normocapnia (red curve) and hypocapnia (blue curve) at SDD of 20 mm (A) and 27 mm (B) with count rates of ~465 and ~55 kHz, respectively. The fit of the ML DCS model is illustrated by the black curve.

No significant changes in any of the blood flow indices (i.e. F_S and F_B values from the ML DCS analysis and F_{HM} from the HM-DCS analysis) were found by comparing values pre and post scalp incisions. This unexpected finding was likely due to increased variability in the DCS signal due to probe pressure effects since it was necessary to remove the fibers to perform the incisions (Mesquita et al., 2013). Consequently, capnic data before and after scalp incision were grouped together in all subsequent analysis. Note, SBF measured by CTP did not change with scalp incisions since the scalp ROI (Figure 4-1) was lateral to probe location to avoid breathing-related motion artifacts.

Figure 4-4 plots the blood flow estimates obtained by CTP and DCS for the two $paCO_2$ conditions. Significant differences between normocapnia and hypocapnia were found for CBF measured by CTP [$p<0.001$, partial-η^2 = 0.984, Power = 1] and F_B measured by ML DCS [$p<0.05$, partial-η^2 = 0.816, Power = 0.685]. Significant differences were also found for F_{HM} at a SDD of 20 mm [$p<0.05$, partial-η^2 > 0.876,

Power > 0.852] and a SDD of 27 mm [$p<0.05$, partial-$\eta^2 > 0.826$, Power > 0.710]. In contrast, no significant differences between capnic conditions were found for SBF measured by CTP, and F_S measured by ML DCS. Finally, skull flow measured by CTP (8.9 ± 0.7 mL/min/100g) and the coherence factors β (0.158 ± 0.001 and 0.168 ± 0.002, for SDD of 20 and 27 mm, respectively) did not change significantly with $paCO_2$ (data not shown).

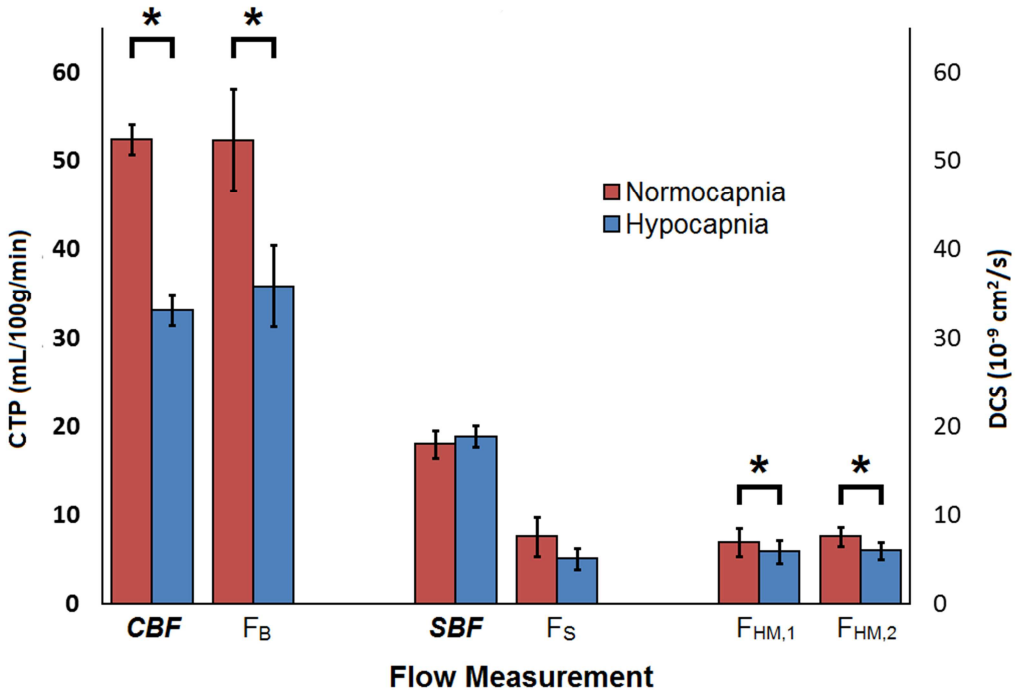

Figure 4-4: Absolute blood flow in the scalp and brain measured by CTP and DCS during normocapnia and hypocapnia

Scalp blood flow (SBF) and cerebral blood flow (CBF) measured by CT, and the corresponding blood flow indices measured by DCS during normocapnia (red bars) and hypocapnia (blue bars). All values were averaged over their pre- and post- scalp incision measurements. F_S and F_B were obtained from the ML model analysis of DCS data acquired at SDDs of 20 and 27 mm. F_{HM} was obtained by analyzing data from each SDD separately with the HM model ($F_{HM,1}$ refers to 20 mm and $F_{HM,2}$ refers to 27 mm). Significant differences observed between capnic conditions are represented by *.

Table 4-2: Mean absolute flow values in the scalp and brain measured by CTP and DCS during normocapnia and hypocapnia

Capnic Condition	*CBF (mL/min/100g)	*F_B (10^{-9} cm^2/s)	SBF (mL/min/100g)	F_S (10^{-9} cm^2/s)	*$F_{HM,1}$ (10^{-9} cm^2/s)	*$F_{HM,2}$ (10^{-9} cm^2/s)
Normocapnia	52.4 ± 1.7	52.3 ± 6.9	18.1 ± 1.5	7.3 ± 2.1	7.1 ± 1.3	7.7 ± 1.1

Hypocapnia	33.2 ± 1.7	36.3 ± 4.2	19.0 ± 1.2	5.0 ± 1.2	6.0 ± 1.3	6.1 ± 1.0

Average flow values (CBF and SBF, F_B and F_S) measured by CTP and ML DCS, respectively, for normocapnic and hypocapnic conditions. Significant differences between capnic conditions are indicated by *.

A significant Pearson correlation (R = 0.538) was observed between CBF and F_B. Likewise, significant correlations were observed between F_S and both $F_{HM,1}$ (R = 0.972) and $F_{HM,2}$ (R = 0.881).

4.4.2.3 Relative Blood Flow

The relative change in CBF and DCS indices when reducing $paCO_2$ from normocapnia to hypocapnia are presented in Figure 4-5.

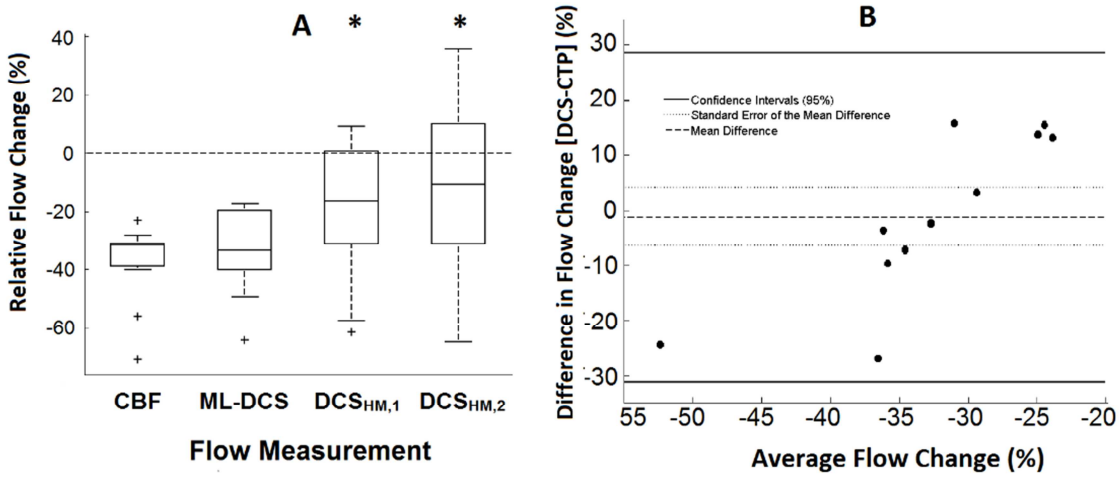

Figure 4-5: Comparison between the percent difference of CBF measured by CTP and different DCS flow models acquired on the skin of the intact head of pigs

(A) Box plot of relative flow change caused by reducing $paCO_2$ from normocapnia to hypocapnia. Flow values of CBF, F_B, $F_{HM,1}$ and $F_{HM,2}$ measured by CTP (N = 14), ML DCS (N = 11), DCS$_{HM,1}$ (N = 14) and DCS$_{HM,2}$ (N = 14), respectively. The center line, box edges, error bars, and the cross represent the median, 1st and 3rd quartiles, $CI_{95\%}$, and outliers, respectively. Significant changes compared to CBF are represented by *. (B) Bland-Altman plot comparing reductions in CBF and F_B measured by CTP and ML DCS (N = 11). The mean difference between the two modalities, the standard error of the mean, and the $CI_{95\%}$ are indicated by the solid line, the dotted line and the dashed line, respectively. Flow change measured while the scalp tissue was intact or incised is represented by circle and diamond symbols, respectively.

Mean CBF reduction measured by CTP (−36.4 ± 3.3 %) was not significantly different from the corresponding F_B change (−33.5 ± 4.5 %). In contrast, the $F_{HM,1}$ change (-13.2 ± 7.5 %) was significantly different from both the CTP and ML DCS results.

Similarly, the change in $F_{HM,2}$ (-19.1 ± 6.0 %) was significantly different from CTP results and a trend was observed when compared to F_B ($p = 0.054$). A Bland-Altman analysis comparing relative CBF changes measured by CTP and ML DCS is shown in Figure 4-5B. The mean difference between the two modalities was -1.2 ± 4.6 % ($CI_{95\%}$: -31.1 and 28.6). Linear regression analysis of the Bland-Altman plot indicted a significant proportional bias ($p<0.001$, $R = 0.837$).

4.4.2.4 Real-Time Flow Monitoring

To demonstrate the ability of ML DCS to resolve dynamic differences in scalp and brain blood flow, a series of $g_2(\rho,\tau)$ curves acquired during the transition from normocapnia to hypocapnia from one experiment were analyzed (Figure 4-6). In this example, the flow change calculated by the difference between means of the first and last minutes was -42.9 % in the brain and 5.2 % in the scalp. The coefficients of variation for the baseline scalp and brain time series were 9.8 % and 8.4 %, respectively.

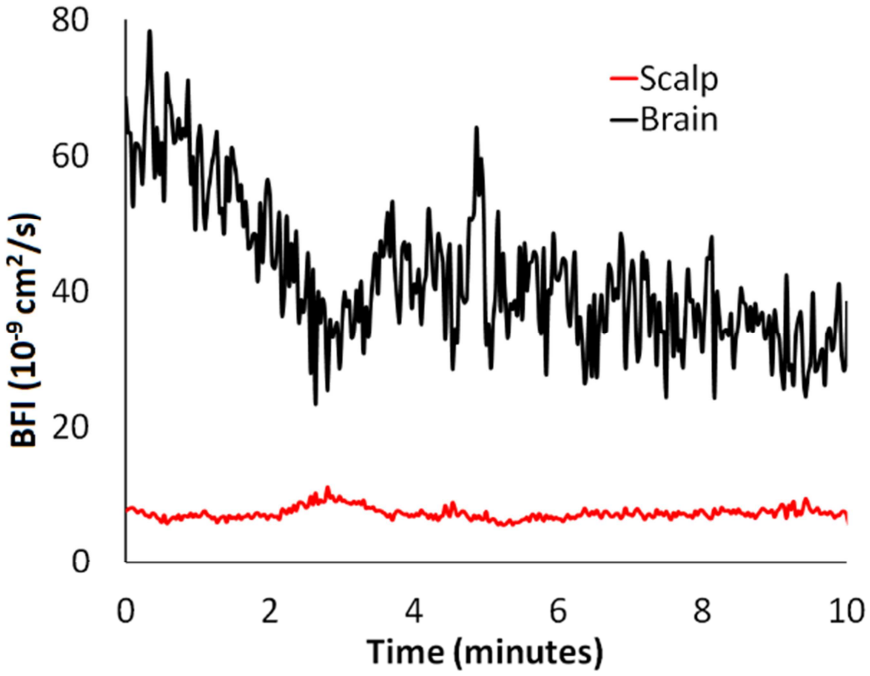

Figure 4-6: Real-time change of scalp and brain BFIs measured during the transition from normocapnia to hypocapnia

Blood flow dynamics during the transition from normocapnia to hypocapnia from one experiment. Each $g_2(\rho,\tau)$ curve was acquired for 2 seconds and analyzed separately by the ML DCS model to obtain time series of FB and FS. Data were acquired at a count rate of 554.3 ± 0.4 kHz and 101.5 ± 0.2 kHz at SDDs of 20 mm and 27 mm, respectively. The thickness of the scalp and the skull were 3.7 ± 0.4 mm and 6.0 ± 0.4 mm, respectively.

4.5 Discussion

The aim of this work was to test the ability of a depth-sensitive DCS approach to retrieve the blood flow index from the brain despite the presence of a substantial superficial tissue layer. The approach was based on obtaining two autocorrelation functions with varying depth sensitivities by placing detectors at distances from the source of 20 and 27 mm. The multi-distance data were then analyzed with a three-layered solution to the correlation diffusion equation to account for light propagation through scalp, skull and brain, and the different blood flows in scalp and brain (Li et al., 2005). Rather than fitting a complete autocorrelation curve, different ranges of correlation times were used to fit the curves obtained at the two source-detector distances in order to alter the weighting to shorter or longer photon pathlengths (Farzam & Durduran, 2015; Selb et al., 2014). More specifically, the range for the longer SDD (27 mm) was restricted to early correlation times, while longer correlation times were selected for the shorter SDD (20 mm).

The feasibility of the ML DCS approach was first verified using a two-layer tissue-mimicking phantom in which the diffusion property of the bottom layer was altered by adding four different cellulose concentrations (Cheung et al., 2001). The change in the measured diffusion coefficient of the bottom layer, which varied from 20% to 80% by increasing the cellulose concentration, was in good agreement with the change observed in the homogeneous phantom over the same concentration range (Figure 4-2). In contrast, as expected, the diffusion coefficient of the 10-mm thick top layer did not change when cellulose was added to the bottom compartment (data not shown). In agreement with Gagnon et al. (Gagnon et al., 2008), these results highlight the ability of a multi-layered model to resolve differences in flow rates in different layers with minimal crosstalk between the measured diffusion coefficients.

The second aim of the study was to apply the same ML DCS approach to an animal model in which CBF was independently measured by CT perfusion. Juvenile pigs

were selected as the total thickness of their extracerebral tissues was expected to be similar to that of adult humans. The mean values of scalp and skull thicknesses were 3.5 ± 0.2 and 6.4 ± 0.4 mm, respectively, which are within the expected range for humans, although larger values can be found depending on the location on the head (Strangman, Zhang, & Li, 2014). Global CBF was reduced by lowering $paCO_2$ from normocapnia to hypocapnia. Overall, good agreement was found between the average CBF reductions measured by CTP (36.4 ± 3.3 %) and ML DCS (33.5 ± 4.5 %). The corresponding estimates of cerebrovascular reactivity (CVR), defined as the change in CBF per unit change in $paCO_2$, were -1.9 ± 0.2 % per mmHg and -1.7 ± 0.2 % per mmHg for CTP and ML DCS, respectively. These estimates are in good agreement with our previous studies involving this animal model: -2.3 % per mmHg from CTP and -2.3 % per mmHg from DCS probes placed directly on the exposed cerebral cortex (Elliott et al., 2014; Verdecchia et al., 2015). In addition, good agreement was also found between the absolute blood flow index determined from ML DCS (Table 4-2: Mean absolute flow values in the scalp and brain measured by CTP and DCS during normocapnia and hypocapnia) and our previous values derived from autocorrelation functions measured directly on the brain, (~$48x10^{-9}$ cm^2/s at normocapnia and ~$28x10^{-9}$ cm^2/s at hypocapnia) (Verdecchia et al., 2015). This agreement suggests that F_B could be used as a marker to track longitudinal changes in CBF, similar to previous DCS studies involving infants (Roche-Labarbe et al., 2012). However, this would require careful assessment of the reproducibility of F_B considering the added complexity of the analysis. Intriguingly, the group-wise variability in F_B (~40%) was in good agreement with previous studies in which the blood flow index was derived from the semi-infinite homogeneous model (Diop et al., 2011; Verdecchia et al., 2015). This is despite the addition of a scalp blood flow index (i.e. F_s) in the fitting routine.

Although the results of this study demonstrate that a multi-layered modeling approach can account for the effects of extracerebral tissue, the accuracy of F_B will be affected by errors in the additional model input parameters (i.e. the thicknesses of scalp and skull, and tissue optical properties). To assess the sensitivity to uncertainties in the thickness measurements, the $g_2(\rho,\tau)$ curves from the tissue-mimicking phantom with a 10-mm top layer were re-analyzed with the top layer thickness varied by ± 20%. The

resulting error in the diffusion coefficient for the bottom layer was less than 10%, similar to that reported by Gagnon et al. (2008). In clinical practice, the thicknesses of the scalp and skull could be obtained from medical images or possibly measured directly using ultrasound. Alternately, the total scalp/skull thickness could be included as an additional fitting parameter, similar to an approach proposed for measuring cerebral oxygenation by multi-distance frequency-domain NIRS (Hallacoglu, Sassaroli, & Fantini, 2013). This would likely require more SD distances than used in the current study and careful attention to the shortest SDD in order to avoid violating the Siegert relationship (Binzoni, Sanguinetti, Van de Ville, Zbinden, & Martelli, 2016). Regarding the optical properties, all three tissue layers were set to the single μ_a and μ_s' values measured by TR NIRS since the primary focus was assessing the ability of DCS to measure changes in CBF, which is fairly insensitive to uncertainties in absolute μ_a and μ_s' (Diop et al., 2011; Irwin et al., 2011). Separate values of μ_a and μ_s' for each tissue layer could be obtained using a multi-layer solution to analyze the TR NIRS data (Diop & St Lawrence, 2013; Liemert & Kienle, 2013).

An alternative and simpler approach to account for partial volume errors is to multiply the change in the blood flow index obtained from the homogeneous model by a correction factor based on the partial pathlength through brain (Durduran et al., 2004; Gagnon et al., 2008; Selb et al., 2014). Durduran et al. (2004a) initially used a value of 5 based on modeling the head as a two-layered medium. More recently, Selb et al. proposed a factor of 3 by restricting the fitting to early correlation times. In the current study, correction factors of 2.4 and 1.8 were found for SDDs of 20 and 27 mm, respectively, by comparing the mean change in F_{HM} to the CBF change measured by CTP. Similarly, a factor of 1.5 was determined from the tissue phantom experiments with a 10-mm thick top layer and a SDD of 30 mm. The smaller values at larger separations (27 and 30 mm) would be expected given the improvement in depth sensitivity as the SDD is increased. Although applying a correction factor is simpler than using a multi-layered model, high variability across experiments was found. In this study, the correction factor varied by ± 60% across animals. Furthermore, the similarity between mean F_{HM} and F_S values in Table 4-2: Mean absolute flow values in the scalp and brain measured by CTP and DCS during normocapnia and hypocapnia indicates that the DCS

signal is heavily weighted by extracerebral tissue. This sensitivity could lead to erroneous CBF estimates if scalp blood flow changed due to systemic effects or variations in surface probe pressure, highlighting the value of a multi-layered model to uncouple brain and scalp blood flow.

An unexpected finding was the proportional bias revealed by regression analysis in the Bland-Altman plot (Figure 4-5B) despite similar flow changes measured by CTP and ML DCS (mean difference = -1.2 ± 4.6 %). This bias remained even after removing the outlier that had a mean CBF change greater than 50%. One explanation is the accuracy of the ML DCS approach could be affected by variations in the thickness of the extracerebral layer; however, no correlation with F_B was found. Considering the range of CBF reductions was limited to between 20 to 40%, this bias should be viewed with caution. A wider range of flow changes, for instance by including hypercapnia experiments to increase CBF, would help to assess the validity of the observed bias. Another unexpected finding was an average perfusion signal in skull of 9 mL/min/100g measured by CTP. This would appear to contradict the assumption of the ML DCS method that skull has negligible blood flow. However, this value is likely artificial considering a similar 'perfusion' signal (10 mL/min/100g) was found in the probe holder (see Figure 4-1B). Likely this artifact is related to greater variability in flow estimates in areas of extremely low contrast enhancement. It should be noted that there was no change in skull blood flow between capnic levels.

4.6 Conclusion

In summary, this study demonstrates that DCS has the ability to separate scalp and brain blood flow, as demonstrated in Figure 4-6, despite the presence of a relatively thick extracerebral layer (of the order of 1 cm). The ML DCS technique could be further optimized by incorporating optical property measurements for the different tissue layers and by improving the SNR through the use of a software correlator to measure only relevant correlations times (Wang et al., 2016). Recent improvements for monitoring CBF were demonstrated in the adult head by a pressure modulation algorithm, without requiring a priori anatomical information (Baker et al., 2015). The approach taken by Baker et al. could be combined with the multi-layered model presented in this study to

isolate cerebral signals detected by DCS when estimating extracerebral tissue thickness by imaging methods is unavailable. Future work will implement a multi-layered DCS/TR-NIRS hybrid to demonstrate a means of quantifying the cerebral metabolic rate of oxygen in adults (Elliott et al., 2014; Verdecchia, Diop, Lee, & St. Lawrence, 2013).

4.7 References

Al-Tamimi, Y. Z., Orsi, N. M., Quinn, A. C., Homer-Vanniasinkam, S., & Ross, S. A. (2010). A review of delayed ischemic neurologic deficit following aneurysmal subarachnoid hemorrhage: Historical overview, current treatment, and Pathophysiology. *World Neurosurgery*, *73*(6), 654–667. doi:10.1016/j.wneu.2010.02.005

Baker, W. B., Parthasarathy, A. B., Busch, D. R., Mesquita, R. C., Greenberg, J. H., & Yodh, a G. (2014). Modified Beer-Lambert law for blood flow. *Biomedical Optics Express*, *5*(11), 4053–75. doi:10.1364/BOE.5.004053

Baker, W. B., Parthasarathy, A. B., Ko, T. S., Busch, D. R., Abramson, K., Tzeng, S.-Y., … Yodh, A. G. (2015). Pressure modulation algorithm to separate cerebral hemodynamic signals from extracerebral artifacts. *Neurophotonics*, *2*(3), 035004. doi:10.1117/1.NPh.2.3.035004

Binzoni, T., Sanguinetti, B., Van de Ville, D., Zbinden, H., & Martelli, F. (2016). Probability density function of the electric field in diffuse correlation spectroscopy of human bone in vivo. *Applied Optics*, *55*(4), 757–762. doi:10.1364/AO.55.000757

Boas, D., Campbell, L., & Yodh, A. G. (1995). Scattering and imaging with diffusing temporal field correlations. *Physical Review Letters*, *75*(9), 1855–1858. Retrieved from http://link.aps.org/doi/10.1103/PhysRevLett.75.1855

Brown, D. W., Picot, P. a, Naeini, J. G., Springett, R., Delpy, D. T., & Lee, T.-Y. (2002). Quantitative near infrared spectroscopy measurement of cerebral hemodynamics in newborn piglets. *Pediatric Research*, *51*(5), 564–70. Retrieved from http://www.ncbi.nlm.nih.gov/pubmed/11978878

Buckley, E. M., Parthasarathy, A. B., Grant, P. E., Yodh, A. G., & Franceschini, M. A. (2014). Diffuse correlation spectroscopy for measurement of cerebral blood flow: future prospects. *Neurophotonics*, *1*(1), 011009. doi:10.1117/1.NPh.1.1.011009

Cenic, A., Nabavi, D. G., Craen, R. a, Gelb, a W., & Lee, T. Y. (1999). Dynamic CT measurement of cerebral blood flow: a validation study. *American Journal of Neuroradiology*, *20*(1), 63–73. Retrieved from http://www.ncbi.nlm.nih.gov/pubmed/9974059

Cheung, C., Culver, J. P., Takahashi, K., Greenberg, J. H., & Yodh, A. G. (2001). In vivo cerebrovascular measurement combining diffuse near-infrared absorption and correlation spectroscopies. *Physics in Medicine and Biology*, *46*(8), 2053–65. Retrieved from http://www.ncbi.nlm.nih.gov/pubmed/11512610

De Oliveira Manoel, A. L., Goffi, A., Marotta, T. R., Schweizer, T. A., Abrahamson, S., & Macdonald, R. L. (2015). The critical care management of poor-grade subarachnoid haemorrhage. *Critical Care*, *20*(1), 21. doi:10.1186/s13054-016-1193-9

Dhar, R., Scalfani, M. T., Blackburn, S., Zazulia, A. R., Videen, T., & Diringer, M. (2012). Relationship between angiographic vasospasm and regional hypoperfusion in aneurysmal subarachnoid hemorrhage. *Stroke*, *43*(7), 1788–1794. doi:10.1161/STROKEAHA.111.646836

Diop, M., Kishimoto, J., Toronov, V., Lee, D. S. C., & Lawrence, K. S. (2015). Development of a combined broadband near-infrared and diffusion correlation system for monitoring cerebral blood flow and oxidative metabolism in preterm infants. *Biomedical Optics Express*, *6*(10), 3907–3918. doi:10.1364/BOE.6.003907

Diop, M., & St Lawrence, K. (2013). Improving the depth sensitivity of time-resolved measurements by extracting the distribution of times-of-flight. *Biomedical Optics Express*, *4*(3), 447–59. doi:10.1364/BOE.4.000447

Diop, M., Tichauer, K. M., Elliott, J. T., Migueis, M., Lee, T.-Y., & St. Lawrence, K. (2010). Comparison of time-resolved and continuous-wave near-infrared techniques for measuring cerebral blood flow in piglets. *Journal of Biomedical Optics*, *15*(5), 057004. doi:10.1117/1.3488626

Diop, M., Verdecchia, K., Lee, T.-Y., & St Lawrence, K. (2011). Calibration of diffuse correlation spectroscopy with a time-resolved near-infrared technique to yield absolute cerebral blood flow measurements. *Biomedical Optics Express*, *2*(7), 2068. doi:10.1364/BOE.2.002068

Durduran, T., & Yodh, A. G. (2014). Diffuse correlation spectroscopy for non-invasive, micro-vascular cerebral blood flow measurement. *NeuroImage*, *85 Pt 1*, 51–63. doi:10.1016/j.neuroimage.2013.06.017

Durduran, T., Yu, G., Burnett, M. G., Detre, J. a, Greenberg, J. H., Wang, J., … Yodh, A. G. (2004). Diffuse optical measurement of blood flow, blood oxygenation, and metabolism in a human brain during sensorimotor cortex activation. *Optics Letters*, *29*(15), 1766–8. Retrieved from http://www.ncbi.nlm.nih.gov/pubmed/15352363

Elliott, J. T., Diop, M., Morrison, L. B., D'Esterre, C. D., Lee, T.-Y., & St Lawrence, K. (2014). Quantifying cerebral blood flow in an adult pig ischemia model by a depth-resolved dynamic contrast-enhanced optical method. *NeuroImage*, *94C*, 303–311. doi:10.1016/j.neuroimage.2014.03.023

English, S. W., Turgeon, A. F., Owen, E., Doucette, S., Pagliarello, G., & McIntyre, L. (2013). Protocol management of severe traumatic brain injury in intensive care units: A systematic review. *Neurocritical Care*, *18*(1), 131–142. doi:10.1007/s12028-012-9748-3

Farzam, P., & Durduran, T. (2015). Multidistance diffuse correlation spectroscopy for simultaneous estimation of blood flow index and optical properties. *Journal of Biomedical Optics*, *20*(5), 055001. doi:10.1117/1.JBO.20.5.055001

Gagnon, L., Desjardins, M. 'R., Jehanne-Lacasse, J., Bherer, L., & Lesage, F. Ú. Ú. (2008). Investigation of diffuse correlation spectroscopy in multi-layered media including the human head. *Optics Express*, *16*(20), 15514–15530. Retrieved from http://www.opticsinfobase.org/abstract.cfm?id=172103

Hallacoglu, B., Sassaroli, A., & Fantini, S. (2013). Optical Characterization of Two-Layered Turbid Media for Non-Invasive, Absolute Oximetry in Cerebral and Extracerebral Tissue. *PLoS ONE*, *8*(5), e64095. doi:10.1371/journal.pone.0064095

Haskell, R. C., Svaasand, L. O., Tsay, T. T., Feng, T. C., McAdams, M. S., & Tromberg, B. J. (1994). Boundary conditions for the diffusion equation in radiative transfer. *Journal of the Optical Society of America. A, Optics, Image Science, and Vision*, *11*(10), 2727–2741.

Irwin, D., Dong, L., Shang, Y., Cheng, R., Kudrimoti, M., Stevens, S. D., & Yu, G. (2011). Influences of tissue absorption and scattering on diffuse correlation spectroscopy blood flow measurements. *Biomedical Optics Express*, *2*(7), 1969–85. doi:10.1364/BOE.2.001969

Kienle, A., & Glanzmann, T. (1999). In vivo determination of the optical properties of muscle with time-resolved reflectance using a layered model. *Physics in Medicine and Biology*, *44*(11), 2689–702. Retrieved from http://www.ncbi.nlm.nih.gov/pubmed/10588278

Kirkman, M. A., Citerio, G., & Smith, M. (2014). The intensive care management of acute ischemic stroke: An overview. *Intensive Care Medicine*, *40*(5), 640–653. doi:10.1007/s00134-014-3266-z

Kirkpatrick, P. J., Smielewski, P., Czosnyka, M., & Pickard, J. D. (1994). Continuous monitoring of cortical perfusion by laser Doppler flowmetry in ventilated patients with head injury. *Journal of Neurology, Neurosurgery, and Psychiatry*, *57*(11), 1382–8. Retrieved from http://www.ncbi.nlm.nih.gov/pubmed/1073191

Lee, T.-Y. (2002). Functional CT: physiological models. *Trends in Biotechnology*, *20*(8), S3–S10. doi:10.1016/S0167-7799(02)02035-8

Lemieux, P., & Durian, D. (1999). Investigating non-Gaussian scattering processes by using nth-order intensity correlation functions. *Journal of the Optical Society of America A*. doi:10.1364/JOSAA.16.001651

Li, J., Dietsche, G., Iftime, D., Skipetrov, S. E., Maret, G., Elbert, T., … Gisler, T. (2005). Noninvasive detection of functional brain activity with near-infrared diffusing-wave spectroscopy. *Journal of Biomedical Optics*, *10*(4), 44002. doi:10.1117/1.2007987

Liemert, A., & Kienle, A. (2013). Light diffusion in N-layered turbid media: steady-state domain. *Journal of Biomedical Optics*, *15*(2), 025003. doi:10.1117/1.3368685

Lin, P.-Y., Roche-Labarbe, N., Dehaes, M., Carp, S., Fenoglio, A., Barbieri, B., … Franceschini, M. A. (2013). Non-invasive optical measurement of cerebral metabolism and hemodynamics in infants. *Journal of Visualized Experiments : JoVE*, (73), e4379. doi:10.3791/4379

Macdonald, R. L. (2014). Delayed neurological deterioration after subarachnoid haemorrhage. *Nature Reviews. Neurology*, *10*(1), 44–58. doi:10.1038/nrneurol.2013.246

Mesquita, R. C., Schenkel, S. S., Minkoff, D. L., Lu, X., Favilla, C. G., Vora, P. M., … Yodh, a G. (2013). Influence of probe pressure on the diffuse correlation spectroscopy blood flow signal: extra-cerebral contributions. *Biomedical Optics Express*, *4*(7), 978–94. doi:10.1364/BOE.4.000978

Murphy, B. D., Fox, a J., Lee, D. H., Sahlas, D. J., Black, S. E., Hogan, M. J., … Lee, T.-Y. (2006). Identification of penumbra and infarct in acute ischemic stroke using computed tomography perfusion-derived blood flow and blood volume measurements. *Stroke; a Journal of Cerebral Circulation*, *37*(7), 1771–7. doi:10.1161/01.STR.0000227243.96808.53

Ntziachristos, V., & Chance, B. (2001). Accuracy limits in the determination of absolute optical properties using time-resolved NIR spectroscopy. *Medical Physics*, *28*(6), 1115. doi:10.1118/1.1373674

Obrig, H., & Steinbrink, J. (2011). Non-invasive optical imaging of stroke. *Philosophical Transactions of the Royal Society A: Mathematical, Physical and Engineering Sciences*, *369*(1955), 4470–4494. doi:10.1098/rsta.2011.0252

Roche-Labarbe, N., Fenoglio, A., Aggarwal, A., Dehaes, M., Carp, S. A., Franceschini, M. A., & Grant, P. E. (2012). Near-infrared spectroscopy assessment of cerebral oxygen metabolism in the developing premature brain. *Journal of Cerebral Blood Flow & Metabolism*, *32*(3), 481–488. doi:10.1038/jcbfm.2011.145

Selb, J., Boas, D. a., Chan, S.-T., Evans, K. C., Buckley, E. M., & Carp, S. a. (2014). Sensitivity of near-infrared spectroscopy and diffuse correlation spectroscopy to brain hemodynamics: simulations and experimental findings during hypercapnia. *Neurophotonics*, *1*(1), 015005. doi:10.1117/1.NPh.1.1.015005

Skipetrov, S. E., & Maynard, R. (1996). Dynamic multiple scattering of light in multilayer turbid media. *Physics Letters, Section A: General, Atomic and Solid State Physics*, *217*(2-3), 181–185. doi:10.1016/0375-9601(96)00335-0

Steinkellner, O., Gruber, C., Wabnitz, H., Jelzow, A., Steinbrink, J., Fiebach, J. B., … Obrig, H. (2010). Optical bedside monitoring of cerebral perfusion: technological and methodological advances applied in a study on acute ischemic stroke. *Journal of Biomedical Optics*, *15*(6), 61708–61710. doi:10.1117/1.3505009

Strangman, G. E., Zhang, Q., & Li, Z. (2014). Scalp and skull influence on near infrared photon propagation in the Colin27 brain template. *NeuroImage*, *85 Pt 1*, 136–49. doi:10.1016/j.neuroimage.2013.04.090

Vajkoczy, P., Roth, H., Horn, P., Lucke, T., Thomé, C., Hubner, U., … Schmiedek, P. (2000). Continuous monitoring of regional cerebral blood flow: experimental and

clinical validation of a novel thermal diffusion microprobe. *Journal of Neurosurgery*, *93*(2), 265–274. doi:10.3171/jns.2000.93.2.0265

Verdecchia, K., Diop, M., Lee, T.-Y., & St. Lawrence, K. (2013). Quantifying the cerebral metabolic rate of oxygen by combining diffuse correlation spectroscopy and time-resolved near-infrared spectroscopy. *Journal of Biomedical Optics*, *18*(2), 027007. doi:10.1117/1.JBO.18.2.027007

Verdecchia, K., Diop, M., Morrison, L. B., Lee, T.-Y., & St. Lawrence, K. (2015). Assessment of the best flow model to characterize diffuse correlation spectroscopy data acquired directly on the brain. *Biomedical Optics Express*, *6*(11), 4288. doi:10.1364/BOE.6.004288

Wang, D., Parthasarathy, A. B., Baker, W. B., Gannon, K., Kavuri, V., Ko, T., … Yodh, A. G. (2016). Fast blood flow monitoring in deep tissues with real-time software correlators. *Biomedical Optics Express*, *7*(3), 776. doi:10.1364/BOE.7.000776

Weigl, W., Milej, D., Gerega, a., Toczylowska, B., Kacprzak, M., Sawosz, P., … Liebert, a. (2014). Assessment of cerebral perfusion in post-traumatic brain injury patients with the use of ICG-bolus tracking method. *NeuroImage*, *85*, 555–565. doi:10.1016/j.neuroimage.2013.06.065

Zweifel, C., Castellani, G., Czosnyka, M., Helmy, A., Manktelow, A., Carrera, E., … Smielewski, P. (2010). Noninvasive monitoring of cerebrovascular reactivity with near infrared spectroscopy in head-injured patients. *J Neurotrauma*, *27*(11), 1951–1958. doi:10.1089/neu.2010.1388

Chapter 5

5 Discussion/Conclusion

The main objective of this thesis was to advance diffuse correlation spectroscopy (DCS) techniques with the long-term aim of assessing cerebral hemodynamics and metabolism in the intensive care unit (ICU). Typically, near-infrared spectroscopy (NIRS) measures tissue oxygen saturation but it also can measure CBF using an optical dye as an intravascular contrast agent (Brown et al., 2002). This approach has been subsequently adapted to time-resolved (TR) NIRS to improve its depth sensitivity and used to calibrate DCS in order to monitor absolute perfusion (Diop, Verdecchia, Lee, & St. Lawrence, 2011). In chapter 2, this NIRS/DCS method was expanded to quantify the cerebral metabolic rate of oxygen ($CMRO_2$). In chapter 3, the most appropriate flow model for DCS was investigated by acquired data directly on the brain. Chapter 4 outlined experiments aimed at assessing a multi-layered (ML) DCS method capable of measuring CBF through extracerebral tissues comparable in thickness to adults. The individual advancements in DCS techniques achieved in each chapter will be summarized in this chapter, and future work to further improve DCS will be discussed. Lastly, the main conclusions of the thesis will be listed.

5.1 Summary

The main objectives of this thesis focused towards advancing DCS techniques by:

1) Demonstrating an all-optical device that includes DCS is capable of quantifying $CMRO_2$.

2) Furthering our understanding of the widely accepted diffusion model of flow applied to DCS.

3) Implementing a multi-layered DCS model to separate flow in extracerebral and cerebral tissues.

Outlined in the following subsections is an overview of the progress to DCS methods made by the three objectives of this work.

5.1.1 Quantification of $CMRO_2$ by an all-optical modality

Monitoring CBF at the bedside would improve patient outcome by detecting reductions in flow; however, additional monitoring of the metabolic rate would help evaluate tissue viability since $CMRO_2$ is considered a better indicator of cerebral ischemia than CBF and oxygenation measurements alone (Powers, Grubb, Darriet, & Raichle, 1985; Tichauer et al., 2009; Tichauer, Brown, Hadway, Lee, & St. Lawrence, 2006). Diffuse correlation spectroscopy provides a means to monitor flow changes directly, but it is unable to assess the tissue metabolic demands. Combining DCS with NIRS has been used to measure changes in $CMRO_2$ in the developing brain (Roche-Labarbe et al., 2010, 2012), but the inability of DCS to quantify CBF hinders the all-optical technique from establishing absolute metabolic thresholds.

Recently, our group demonstrated that the DCS signal can be used to measure absolute perfusion through calibration with a TR NIRS bolus-tracking method (Diop et al., 2011). This technique was expanded in Chapter 2 to show that the combination of DCS with TR NIRS can also measure $CMRO_2$. In this combination, DCS and contrast-enhanced NIRS were used to measure CBF, and multi-wavelength TR NIRS was used to determine the cerebral venous blood oxygenation (SvO_2), which was verified by directly measuring oxygenation in the sagittal sinus. Different cerebral metabolic rates were induced by altering the anesthetics in newborn pigs. This animal model was chosen since the scalp and skull are relatively thin and, hence, the optical measurements are principally from the brain. No significant differences were found between the two sets of SvO_2 measurements obtained by TR NIRS and sagittal sinus blood samples. In addition, Bland–Altman analysis showed a small difference in the corresponding $CMRO_2$ values (0.027 ± 0.834 mL O_2/100g/min) over a range from 0.3 to 4 mL O_2/100g/min. This initial validation study demonstrates that quantitative $CMRO_2$ values can be obtained by a DCS/NIRS hybrid system.

5.1.2 Measurements of Relative Blood Flow Changes Directly on Brain Parenchyma

The normalized temporal intensity autocorrelation function generated by DCS is typically characterized by assuming that the movement of erythrocytes can be modeled as a Brownian diffusion-like process instead of by the expected random flow model (Cheung, Culver, Takahashi, Greenberg, & Yodh, 2001). Most applications of DCS accept the assumption that Brownian diffusion characterizes moving erythrocytes since this flow model approximates the computed autocorrelation function well (Durduran & Yodh, 2014). Recently, a hybrid model, referred to as the hydrodynamic diffusion model, was proposed, which combines the random and Brownian flow models (Carp et al., 2011).

Chapter 3 investigated the most appropriate flow model to describe autocorrelation functions used to monitor CBF. To avoid confounding effects of extracerebral tissues, these experiments were conducted with the probes placed directly on the brain. Relative flow changes were measured by DCS and were analyzed by three different flow models: random flow, Brownian diffusion, and the combined hydrodynamic diffusion model. Relative flow changes were verified by computed tomography perfusion (−39.7 ± 3.7%), of which, only the random flow model was significantly different (−63.2 ± 4.7%). No significant difference was found compared to the flow measurements derived using the Brownian and hydrodynamic diffusion models (-41.0 ± 4.3% and -44.2 ± 5.0 %, respectively). Although the latter provided better characterization of the autocorrelation functions, the Brownian diffusion model was more robust and, therefore, it is the most practical model for characterizing DCS data.

5.1.3 Measurements of Relative Blood Flow Changes Through Thick Extracerebral Tissue

Arguably the greatest challenge with DCS is the influence of superficial tissue on the detected signal. For simplicity, common DCS techniques assume tissue homogeneity; however in the adult head, extracerebral tissues, such as scalp and skull, lead to underestimations of CBF by DCS (Durduran et al., 2004; Gagnon, Selb, & Boas, 2008). Chapter 4 investigated a ML model that accounts for light propagation in multiple tissue layers, which was applied to DCS data acquired at multiple source-detector distances.

First, the ML DCS model was verified in a two-layer diffusion phantom by separating diffusion in the bottom and top layers. Next, global reductions in CBF (−33.5 ± 4.5 %) were measured by ML DCS in pigs with an extracerebral tissue thickness similar to adults (9.8 ± 0.4 mm). For validation, perfusion changes (−36.4 ± 3.3 %) were measured independently by computed tomography. Bland-Altman analysis determined a mean difference of -1.2 ± 4.6 % between the two flow modalities, which was bound by a 95% confidence interval of −31.1 to 28.6 %. This final study demonstrated that reductions in CBF can be measured accurately by ML DCS in adolescent pigs, which mimic the head of adults.

5.2 Future Work

5.2.1 Multi-Layered DCS/NIRS Hybrid System

The main focus of the work completed in this thesis was towards advancing and validating DCS with the long-term goal of using this emerging optical method in combination with NIRS to monitoring CBF and $CMRO_2$ in critical-care patients. In all three chapters, tissue optical properties were quantified by TR NIRS and input into the fitting routine of DCS. For DCS data analysis, the number of fitting parameters were reduced and, more importantly, the accuracy of the DCS fitting routine improved (Diop et al., 2011; Irwin et al., 2011). Notably, combining DCS with TR NIRS provides the ability to monitor both perfusion and $CMRO_2$.

Similar to DCS, TR NIRS is highly sensitive to superficial tissues, which result in underestimations of CBF (Gora et al., 2002). The excellent temporal resolution due to the measurement of the time-of-flight of photons by TR NIRS makes it possible to improve depth sensitivity by time-gating and moment analysis strategies (Diop & St. Lawrence, 2013; Liebert, Wabnitz, & Elster, 2012). A previous colleague demonstrated that multi-detector TR NIRS can accurately quantify CBF in a heterogeneous medium (Elliott et al., 2014; Elliott, 2013). Naturally, similar to Diop et al. (Diop et al., 2011), the next step is to combine the dissertation work completed by Elliot (2013) with the ML DCS technique presented in Chapter 4 in order to calibrate changes in CBF in the adult head. This idea can be expanded by estimating optical properties for separate tissues using a multi-layer

solution to analyze the TR NIRS data (Liemert & Kienle, 2013). In turn, the cerebral oxygen saturation could be measured, and therefore, the method presented in Chapter 2 could be used to measure CBF and $CMRO_2$ in the adult head.

5.2.2 Real-Time Data Acquisition

The current NIRS/DCS hybrid device designed for the experiments conducted in this thesis did not have the capability to provide real-time monitoring. Simultaneous data acquisition of TR NIRS and DCS is not feasible due to the interplay of detected light, and alternating manually between optical components is required. A possible solution would be to automate transitions between NIRS/DCS components but would not allow simultaneous acquisitions. Installing band-pass filters would make concurrent NIRS and DCS measurements feasible by removing unnecessary wavelengths at the detection site of each component. A more challenging approach would be to design a detection system that utilizes the same components to generate both the autocorrelation functions and the TPSFs required for DCS and TR NIRS, respectively.

All data analysis in this thesis required post-analysis to compute the respective physiological parameters. Before transferring the NIRS/DCS system from the laboratory to the clinic, real-time digitization of measured data is needed. Specific for DCS, the current data throughput is relatively slow (~1 Hz), which means detected light generates an autocorrelation curve with sufficient SNR to assess tissue hemodynamics every second. Work completed in this thesis used few-mode fiber bundles for optimal temporal resolution of light detection (Dietsche et al., 2007). However for the adult head (Chapter 4), long data acquisition times (~30-60 seconds) were acquired by ML DCS despite utilizing up to 10 few-mode detection fibers located at the largest source-detector distance. Future improvements to DCS techniques presented in this thesis would be to incorporate new innovative methods. For example, converting the correlator board from the computationally expensive hardware to software would improve the throughput up to 50 Hz, which is fast enough to resolve heartbeat fluctuations (Wang et al., 2016). Implementing recent innovations with the ML DCS technique presented in Chapter 4 will increase the speed of blood flow measurements, which may provide real-time perfusion changes at the bedside of neurocritical adults.

5.2.3 Clinical Validation

Pre-clinical experiments simplify optical data collection by lessening potential artifacts, such to hair and motion; however, in the clinic, these artifacts are difficult to avoid. Therefore, it is imperative to demonstrate and validate the feasibility of a NIRS/DCS system at the bedside of patients in clinical trials.

Due to the challenges presented in the clinic, the accuracy and precision of ML DCS should be investigated and compared to various perfusion imaging modalities, including positron emission tomography, computed tomography, and magnetic resonance imaging (arterial spin labeling or phase-contrast). Next, different neurological emergencies should be assessed to investigate the clinical value of monitoring CBF with regards to improving the detection and prognosis of delayed cerebral ischemia. Lastly, a comparison of the success/failure of monitoring changes in CBF by ML DCS with different management strategies to current clinical care practices would determine the extent ML DCS fulfills a niche as a noninvasive bedside monitoring device of blood flow before accepting DCS as a useful bedside management tool in the ICU. The same extent of clinical trials should be performed to investigate the clinical utility of combining ML DCS and TR NIRS to quantify $CMRO_2$. Clinical trials, in which, both CBF and $CMRO_2$ is monitored should be completed to understand the relationship during treatment of neurological emergencies in the ICU to optimize patient outcome.

5.3 Conclusions

With the purpose of assessing cerebral hemodynamics at the bedside, the primary findings of this thesis advanced DCS by:

1. An all-optical modality, which included combining DCS and TR NIRS, demonstrated changes in absolute $CMRO_2$ agree well with direct measurements of blood oxygenation in newborn pigs.

2. Relative flow changes measured by DCS, which was confirmed by computed tomography, are similar when characterized by Brownian and hydrodynamic models directly on the exposed cortical tissue in pigs. Although the latter provides a

better fit to DCS data, the former is more robust deeming it the better model to characterize flow changes by DCS.

3. Implementation of a multi-layered model to DCS separates flow in extracerebral and cerebral tissues successfully. Furthermore, the relative changes in CBF measured by a multi-layered DCS technique were in good agreement with perfusion changes measured by computed tomography in pigs, which had an extracerebral tissue thickness of 1 cm.

5.4 References

Brown, D. W., Picot, P. a, Naeini, J. G., Springett, R., Delpy, D. T., & Lee, T.-Y. (2002). Quantitative near infrared spectroscopy measurement of cerebral hemodynamics in newborn piglets. *Pediatric Research*, *51*(5), 564–70. Retrieved from http://www.ncbi.nlm.nih.gov/pubmed/11978878

Carp, S. A., Roche-Labarbe, N., Franceschini, M. A., Srinivasan, V. J., Sakadžić, S., & Boas, D. (2011). Due to intravascular multiple sequential scattering, Diffuse Correlation Spectroscopy of tissue primarily measures relative red blood cell motion within vessels. *Biomedical Optics Express*, *2*(7), 2047–54. doi:10.1364/BOE.2.002047

Cheung, C., Culver, J. P., Takahashi, K., Greenberg, J. H., & Yodh, A. G. (2001). In vivo cerebrovascular measurement combining diffuse near-infrared absorption and correlation spectroscopies. *Physics in Medicine and Biology*, *46*(8), 2053–65. Retrieved from http://www.ncbi.nlm.nih.gov/pubmed/11512610

Dietsche, G., Ninck, M., Ortolf, C., Li, J., Jaillon, F., & Gisler, T. (2007). Fiber-based multispeckle detection for time-resolved diffusing-wave spectroscopy: characterization and application to blood flow detection in deep tissue. *Applied Optics*, *46*(35), 8506–8514. doi:10.1364/AO.46.008506

Diop, M., & St Lawrence, K. (2013). Improving the depth sensitivity of time-resolved measurements by extracting the distribution of times-of-flight. *Biomedical Optics Express*, *4*(3), 447–59. doi:10.1364/BOE.4.000447

Diop, M., Verdecchia, K., Lee, T.-Y., & St. Lawrence, K. (2011). Calibration of diffuse correlation spectroscopy with a time-resolved near-infrared technique to yield absolute cerebral blood flow measurements. *Biomedical Optics Express*, *2*(7), 2068–81. doi:10.1364/BOE.2.002068

Durduran, T., & Yodh, A. G. (2014). Diffuse correlation spectroscopy for non-invasive, micro-vascular cerebral blood flow measurement. *NeuroImage*, *85 Pt 1*, 51–63. doi:10.1016/j.neuroimage.2013.06.017

Durduran, T., Yu, G., Burnett, M. G., Detre, J. a, Greenberg, J. H., Wang, J., … Yodh, A. G. (2004). Diffuse optical measurement of blood flow, blood oxygenation, and

metabolism in a human brain during sensorimotor cortex activation. *Optics Letters*, *29*(15), 1766–8. Retrieved from http://www.ncbi.nlm.nih.gov/pubmed/15352363

Elliott, J. T. (2013). on the Development of a Dynamic Contrast-Enhanced Near-Infrared Technique To Measure Cerebral Blood Flow in the Neurocritical Care Unit, (June).

Elliott, J. T., Diop, M., Morrison, L. B., D'Esterre, C. D., Lee, T.-Y., & St Lawrence, K. (2014). Quantifying cerebral blood flow in an adult pig ischemia model by a depth-resolved dynamic contrast-enhanced optical method. *NeuroImage*, *94C*, 303–311. doi:10.1016/j.neuroimage.2014.03.023

Gagnon, L., Selb, J., & Boas, D. (2008). Measurements of Hemoglobin Concentrations in the Human Forehead Using Time-Resolved Reflectance. In *Biomedical Optics* (Vol. 1, pp. 5–7). Retrieved from http://www.opticsinfobase.org/abstract.cfm?URI=BIOMED-2008-BSuE73

Gora, F., Shinde, S., Elwell, C. E., Goldstone, J. C., Cope, M., Delpy, D. T., & Smith, M. (2002). Noninvasive measurement of cerebral blood flow in adults using near-infrared spectroscopy and indocyanine green: a pilot study. *Journal of Neurosurgical Anesthesiology*, *14*(3), 218–222. doi:10.1097/01.ANA.0000018212.74048.52

Irwin, D., Dong, L., Shang, Y., Cheng, R., Kudrimoti, M., Stevens, S. D., & Yu, G. (2011). Influences of tissue absorption and scattering on diffuse correlation spectroscopy blood flow measurements. *Biomedical Optics Express*, *2*(7), 1969–85. doi:10.1364/BOE.2.001969

Liebert, A., Wabnitz, H., & Elster, C. (2012). Determination of absorption changes from moments of distributions of times of flight of photons: optimization of measurement conditions for a two-layered Tissue Model. *Journal of Biomedical Optics*, *17*(5), 057005–1–8. Retrieved from http://biomedicaloptics.spiedigitallibrary.org/article.aspx?articleid=1183164

Liemert, A., & Kienle, A. (2013). Light diffusion in N-layered turbid media: steady-state domain. *Journal of Biomedical Optics*, *15*(2), 025003. doi:10.1117/1.3368685

Powers, W., Grubb, R. L., Darriet, D., & Raichle, M. E. (1985). Cerebral blood flow and cerebral metabolic rate of oxygen requirements for cerebral function and viability in humans. *Journal of Cerebral Blood Flow and Metabolism*, *5*(4), 600–8. doi:10.1038/jcbfm.1985.89

Roche-Labarbe, N., Carp, S. A., Surova, A., Patel, M., Boas, D. A., Grant, P. E., & Franceschini, M. A. (2010). Noninvasive optical measures of CBV, StO2, CBF index, and rCMRO2 in human premature neonates' brains in the first six weeks of life. *Human Brain Mapping*, *31*(3), 341–352. doi:10.1002/hbm.20868

Roche-Labarbe, N., Fenoglio, A., Aggarwal, A., Dehaes, M., Carp, S. A., Franceschini, M. A., & Grant, P. E. (2012). Near-infrared spectroscopy assessment of cerebral oxygen metabolism in the developing premature brain. *Journal of Cerebral Blood Flow & Metabolism*, *32*(3), 481–488. doi:10.1038/jcbfm.2011.145

Tichauer, K. M., Brown, D. W., Hadway, J., Lee, T.-Y., & St. Lawrence, K. (2006). Near-infrared spectroscopy measurements of cerebral blood flow and oxygen consumption following hypoxia-ischemia in newborn piglets. *Journal of Applied Physiology*, *100*(3), 850–7. doi:10.1152/japplphysiol.00830.2005

Tichauer, K. M., Wong, D. Y. L., Hadway, J., Rylett, R. J., Lee, T.-Y., & St. Lawrence, K. (2009). Assessing the severity of perinatal hypoxia-ischemia in piglets using near-infrared spectroscopy to measure the cerebral metabolic rate of oxygen. *Pediatric Research*, *65*(3), 301–6. doi:10.1203/PDR.0b013e318194faa6

Wang, D., Parthasarathy, A. B., Baker, W. B., Gannon, K., Kavuri, V., Ko, T., … Yodh, A. G. (2016). Fast blood flow monitoring in deep tissues with real-time software correlators. *Biomedical Optics Express*, *7*(3), 776. doi:10.1364/BOE.7.000776

APPENDICES

Appendix A: Animal Protocol Approval and Modifications

(Note: signatures, addresses, email addresses, and phone numbers have been removed from original correspondence as per School of Graduate and Postdoctoral Studies requirements.)

A.1: Animal Protocol Approval for Chapter 2

Western

March 24, 2009

This is the Original Approval for this protocol
A Full Protocol submission will be required in 2013

Dear Dr. St. Lawrence:

Your Animal Use Protocol form entitled:
Using Time-resolved Near-infrared Spectroscopy to Measure Cerebral Blood Flow and Energy Metabolism
Funding Agency ONTARIO FEDERATION FOR CEREBRAL PALSY - Grant #R-08-258

has been approved by the University Council on Animal Care. This approval is valid from **March 24th, 2009 to March 31, 2010.** The protocol number for this project is **2009-018**.

1. This number must be indicated when ordering animals for this project.
2. Animals for other projects may not be ordered under this number.
3. If no number appears please contact this office when grant approval is received.
   If the application for funding is not successful and you wish to proceed with the project, request that an internal scientific peer review be performed by the Animal Use Subcommittee office.
4. Purchases of animals other than through this system must be cleared through the ACVS office. Health certificates will be required.

ANIMALS APPROVED FOR 2 Years

Species	Strain	Other Detail	Pain Level	Animal # Total for 2 Years
Pig	Duroc Cross	0-7 days M/F	B	50

REQUIREMENTS/COMMENTS
Please ensure that individual(s) performing procedures on live animals, as described in this protocol, are familiar with the contents of this document.

c.c. Approved Protocol - K. St. Lawrence, J. Hadway, D. Forder
Approval Letter - K. St. Lawrence, J. Hadway, D. Forder

[Removed Signature]

The University *of* Western Ontario
Animal Use Subcommittee / University Council on Animal Care
Health Sciences Centre, • London, Ontario • CANADA – N6A 5C1
PH: 519-661-2111 ext. 86770 • FL 519-661-2028 • www.uwo.ca / animal

A.2: Animal Protocol Modification for Chapter 2

From:
Sent: Thursday, November 17, 2011 11:14 AM
To:
Subject: FW: eSirius Notification - New Protocol Modification Has Been APPROVED2009-018::3

Western

Approval Date:

AUP Number: 2009-018
PI Name: St. Lawrence, Keith
AUP Title: Using Time-Resolved Near-Infrared Spectroscopy to Measure Cerebral Blood Flow and Energy Metabolism

Official Notification of AUS Approval: A MODIFICATION to Animal Use Protocol 2009-018 has been approved.

The holder of this Animal Use Protocol is responsible to ensure that all associated safety components (biosafety, radiation safety, general laboratory safety) comply with institutional safety standards and have received all necessary approvals. Please consult directly with your institutional safety officers.

Submitted by: Copeman, Laura
on behalf of the Animal Use Subcommittee

[signature]

The University *of* Western Ontario
Animal Use Subcommittee / University Council on Animal Care
Health Sciences Centre, • London, Ontario • CANADA – N6A 5C1
PH: 519-661-2111 ext. 86768 • FL 519-661-2028
Email: auspc@uwo.ca • http://www.uwo.ca/animal/website/

A.3: Animal Protocol Approval for Chapters 3 and 4

From:
Sent: Friday, October 07, 2011 3:14 PM
To:
Cc:
Subject: eSirius Notification - New Animal Use Protocol is APPROVED2007-050-06::5

Western

Approval Date:

AUP Number: 2007-050-06
PI Name: St. Lawrence, Keith
AUP Title: Using Near-infrared Spectroscopy To Measure Cerebral Blood Flow In The Neurointensive Care Unit

Official Notice of Animal Use Subcommittee (AUS) Approval: Your new Animal Use Protocol (AUP) entitled "Using Near-infrared Spectroscopy To Measure Cerebral Blood Flow In The Neurointensive Care Unit" has been APPROVED by the Animal Use Subcommittee of the University Council on Animal Care. This approval, although valid for four years, and is subject to annual Protocol Renewal.2007-050-06::5

1. This AUP number must be indicated when ordering animals for this project.
2. Animals for other projects may not be ordered under this AUP number.
3. Purchases of animals other than through this system must be cleared through the ACVS office. Health certificates will be required.

The holder of this Animal Use Protocol is responsible to ensure that all associated safety components (biosafety, radiation safety, general laboratory safety) comply with institutional safety standards and have received all necessary approvals. Please consult directly with your institutional safety officers.

Submitted by: Copeman, Laura
on behalf of the Animal Use Subcommittee
University Council on Animal Care

[signature]

The University *of* Western Ontario
Animal Use Subcommittee / University Council on Animal Care
Health Sciences Centre, ● London, Ontario ● CANADA – N6A 5C1
PH: 519-661-2111 ext. 86768 ● FL 519-661-2028
Email: auspam@uwo.ca ● http://www.uwo.ca/animal/website/

A.4: Animal Protocol Modification for Chapters 3 and 4

From:
Sent: Tuesday, April 17, 2012 10:00 AM
To:
Cc:
Subject: eSirius Notification - New Protocol Modification Has Been APPROVED2007-050-06::5

Western

Approval Date:

AUP Number: 2007-050-06
PI Name: St. Lawrence, Keith
AUP Title: Using Near-Infrared Spectroscopy to Measure Cerebral Blood Flow in the Neurointensive Care Unit

Official Notification of AUS Approval: A MODIFICATION to Animal Use Protocol 2007-050-06 has been approved.

The holder of this Animal Use Protocol is responsible to ensure that all associated safety components (biosafety, radiation safety, general laboratory safety) comply with institutional safety standards and have received all necessary approvals. Please consult directly with your institutional safety officers.
Submitted by: Kinchlea, Will D
on behalf of the Animal Use Subcommittee

[signature]

The University *of* Western Ontario
Animal Use Subcommittee / University Council on Animal Care
Health Sciences Centre, ● London, Ontario ● CANADA – N6A 5C1
PH: 519-661-2111 ext. 86768 ● FL 519-661-2028
Email: auspc@uwo.ca ● http://www.uwo.ca/animal/website/

Appendix B: Copyright Reprint Permission

B.1: Reprint Permission from JBO for Chapter 2

Subject **RE: Request for Reprint Permission**
From
To
Date 2016-06-07 11:30 am

Dear Kyle,

Thank you for seeking permission from SPIE to reprint material from our publications. As author, SPIE shares the copyright with you, so you retain the right to reproduce your paper in part or in whole.
Publisher's permission is hereby granted under the following conditions:
(1) the material to be used has appeared in our publication without credit or acknowledgment to another source; and
(2) you credit the original SPIE publication. Include the authors' names, title of paper, volume title, SPIE volume number, and year of publication in your credit statement.

Sincerely,

Nicole Harris
Administrative Editor, SPIE Publications

SPIE is the international society for optics and photonics.

-----Original Message-----
From:
Sent: Tuesday, June 7, 2016 8:26 AM
To:
Subject: Request for Reprint Permission

Hello,

I am writing to request a copyright agreement granting permission to use the following published papers, in its entirety, for the purpose of my doctoral thesis:

[1] K. Verdecchia, M. Diop, T.-Y. Lee, and K. St. Lawrence, "Quantifying the cerebral metabolic rate of oxygen by combining diffuse correlation spectroscopy and time-resolved near-infrared spectroscopy," J. Biomed.
Opt., vol. 18, no. 2, p. 027007, Feb. 2013.

Thank you for your assistance in this matter.

Kind regards,

Kyle

--
Kyle Verdecchia
PhD/MClSc Candidate (CAMPEP)
Department of Medical Biophysics
Western University
Lawson Health Research Institute

B.2: Reprint Permission from OSA for Chapter 3 and 4

Subject **RE: Request for Reprint Permission**
From
To
Date 2016-06-08 2:37 pm

Dear Kyle Verdecchia,

Thank you for contacting The Optical Society.

Because you are the author of the source paper from which you wish to reproduce material, OSA considers your requested use of its copyrighted materials to be permissible within the author rights granted in the Copyright Transfer Agreement submitted by the requester on acceptance for publication of his/her manuscript. It is requested that a complete citation of the original material be included in any publication. This permission assumes that the material was not reproduced from another source when published in the original publication.

Let me know if you have any questions.

Kind Regards,

Rebecca Robinson
June 8, 2016
Authorized Agent, The Optical Society

-----Original Message-----
From:
Sent: Tuesday, June 07, 2016 11:26 AM
To:
Subject: Request for Reprint Permission

Hello,

I am writing to request a copyright agreement granting permission to use the following published paper, in its entirety, for the purpose of my doctoral thesis:

[1] K. Verdecchia, M. Diop, L. B. Morrison, T.-Y. Lee, and K. St.
Lawrence, “Assessment of the best flow model to characterize diffuse correlation spectroscopy data acquired directly on the brain,” Biomed.
Opt. Express, vol. 6, no. 11, p. 4288, 2015.

Furthermore, I have recently submitted a second manuscript that is currently in your peer-review process. Regarding this submitted manuscript, I would also request copyright agreement granting permission to use the following submitted paper, in its entirety, for the purpose of my doctoral thesis, should it be successfully accepted for publication in your journal:

[2] K. Verdecchia, M. Diop, A. Lee, L. B. Morrison, T.-Y. Lee, and K.
St. Lawrence, "Assessment of a Multi-Layered Diffuse Correlation Spectroscopy Method for Monitoring Cerebral Blood Flow in Adults,"
Biomed. Opt. Express, Manuscript ID: 266705, Submitted May 24, 2016.

Thank you for your assistance in this matter.

Regards,

Kyle
--
Kyle Verdecchia
PhD/MClSc Candidate (CAMPEP)
Department of Medical Biophysics
Western University
Lawson Health Research Institute

Appendix C: Curriculum Vitae

Kyle J. Verdecchia

Post-Secondary Education:

The University of Western Ontario
London, ON
2010 – 2016 Ph.D./Cl-M.Sc. (CAMPEP)

McMaster University
Hamilton, ON
2005 – 2010 B.Sc.

Scholarships and Awards:

2014-2015	Queen Elizabeth II Graduate Scholarship in Science and Technology
2012-2015	CAMPEP Graduate Student Remittance
2011-2015	Western Graduate Research Scholarship
2013-2014	Ontario Graduate Scholarship
2009	Harold E. Johns Studentship in Medical Physics
2005	McMaster Entrance Scholarship
2005	Giovanni Caboto Club Scholarship

Clinical/Teaching Experience:

Teaching Assistant
Western University, London, ON
2013 – 2015

Quality Assurance Physicist
London Regional Cancer Program (LRCP)
2013 & 2015

Medical Physicist Assistant
Windsor Regional Cancer Centre (WRCC)
2009

Selected Publications:

K. Verdecchia, M. Diop, L. B. Morrison, T-Y. Lee, K. St. Lawrence, "Assessment of a Multi-Layered Diffuse Correlation Spectroscopy Method for Monitoring Cerebral Blood Flow in Adults", *Biomedical Optics Express,* **7(9)** (2016).

K. Verdecchia, M. Diop, L. B. Morrison, T-Y. Lee, K. St. Lawrence, "Assessment of the Best Flow Model to Characterize Diffuse Correlation Spectroscopy Data Acquired Directly on the Brain", *Biomedical Optics Express,* **6(11)**:4288-4301 (2015).

K. St. Lawrence, **K. Verdecchia**, J. Elliott, M. Diop, "Measuring Cerebral Hemodynamics and Energy Metabolism by Near-Infrared Spectroscopy", *Brain Energy Metabolism: Neuromethods,* Springer Protocols. Humana Press. Vol. **90**, 265-292 (2014).

K. St. Lawrence, **K. Verdecchia**, J. Elliott, K. Tichauer, M. Diop, T-Y. Lee, "Kinetic Model Optimization for Characterizing Tumour Physiology by Dynamic Contrast-Enhanced Near-Infrared Spectroscopy", *Physics in Medicine and Biology,* **58(5)**:1591-604 (2013).

K. Verdecchia, M. Diop, T-Y. Lee, K. St. Lawrence, "Quantifying the Cerebral Metabolic Rate of Oxygen by Combining Diffuse Correlation Spectroscopy and Time-Resolved Near-Infrared Spectroscopy", *Journal of Biomedical Optics,* **18(2)**:27007 (2013).

M. Diop, **K. Verdecchia**, T-Y. Lee, K. St. Lawrence, "Calibration of Diffuse Correlation Spectroscopy with a Time-Resolved Near-Infrared Technique to Yield *Absolute* Cerebral Blood Flow Measurements", *Biomedical Optics Express,* **2(7)**:2068–2082 (2011).

Conference Proceedings:

K. Verdecchia, A. Lee, M. Diop, K. St. Lawrence, "Characterization of a Hybrid Diffuse Correlation Spectroscopy and Time-Resolved Near-Infrared Spectroscopy System for Real-Time Monitoring of Cerebral Blood Flow and Oxygenation", *Proc. SPIE,* 9313:**35** (2015).

K. Verdecchia, M. Diop, K. St. Lawrence, "Investigation of the Best Model to Characterize Diffuse Correlation Spectroscopy Measurements Acquired Directly on the Brain", *Proc. SPIE,* 9333:**14** (2015).

K. Verdecchia, J. Elliott, K. Tichauer, M. Diop, T-Y. Lee, K. St. Lawrence, "Assessment of Tumour Physiology by Dynamic Contrast-Enhanced Near-Infrared Spectroscopy", *Proc. SPIE,* 8578:**76** (2013).

Professional Meetings:

Oral Presentations

K. Verdecchia, A. Lee, M. Diop, K. St. Lawrence, "Characterization of a Hybrid Diffuse Correlation Spectroscopy and Time-Resolved Near-Infrared Spectroscopy System for Real-Time Monitoring of Cerebral Blood Flow and Oxygenation", Presented as an oral talk at SPIE BiOS, San Francisco, California, USA, February 7 – 12 (2015).

K. Verdecchia, M. Diop, K. St. Lawrence, "Investigation of the Best Model to Characterize Diffuse Correlation Spectroscopy Measurements Acquired Directly on the Brain", Presented as an oral talk at SPIE BiOS, San Francisco, California, USA, February 7 – 12 (2015).

K. Verdecchia, J. Elliott, K. Tichauer, M. Diop, T-Y. Lee, K. St. Lawrence, "Assessment of Tumour Physiology by Dynamic Contrast-Enhanced Near-Infrared Spectroscopy", Presented as an oral talk at SPIE BiOS, San Francisco, California, USA, February 2 – 7 (2013).

K. Verdecchia, M. Diop, T-Y. Lee, K. St. Lawrence, "Quantification of Cerebral Blood Flow and Oxygen Metabolism by Combining Time-Resolved Near-Infrared Spectroscopy and Diffuse Correlation Spectroscopy", Presented as an oral talk at Biomedical Optics and 3-D Imaging: OSA Optics and Photonics Congress, Miami, Florida, USA, April 29 – May 2 (2012).

Poster Presentations

K. Verdecchia, M. Diop, L.B. Morrison, T-Y. Lee, K. St. Lawrence, "Application of a Three-Layer Model to Multi-Distance Diffuse Correlation Spectroscopy: Validation Experiments in Pigs", Presented as a poster at Biomedical Optics, Hollywood, Florida, USA, April 25 – 28 (2016).

K. Verdecchia, A. Lee, M. Diop, L.B. Morrison, T-Y. Lee, K. St. Lawrence, "Assessing cerebral blood flow changes in adults by a multi-layered diffuse correlation spectroscopy technique", Presented as a poster at London Health Research Day, London, Canada, March 29 (2016).

K. St. Lawrence, A. Lee, **K. Verdecchia**, J. Elliott, M. Diop, "Assessing Cerebral Hemodynamics by Dynamic Contrast-Enhanced Near-Infrared Spectroscopy", Presented as a poster at fNIRS, Montreal, Quebec, Canada, October 10 – 12 (2014).

K. Verdecchia, M. Diop, T-Y. Lee, K. St. Lawrence, "Multi-Distance Depth-Resolved Diffuse Correlation Spectroscopy", Presented as a

poster at Biomedical Optics: OSA Optics and Photonics Congress, Miami, Florida, USA, April 26 – 30 (2014).

K. Verdecchia, M. Diop, T-Y. Lee, K. St. Lawrence, "Investigating Contamination from the Extracerebral Layer in Cerebral Blood Flow Measured by a Multi-Distance Optical Technique", Presented as a poster to London Health Research Day, Western University, London, Canada, March 18 (2014).

K. Verdecchia, M. Diop, T-Y. Lee, K. St. Lawrence, "Validating Near-Infrared and Diffuse Correlation Spectroscopy to Measure Oxygen Metabolism in Preterm Infants", Presented as a poster at London Health Research Day, University of Western Ontario, London, Canada, March 20 (2012).

K. Verdecchia, M. Diop, K. St. Lawrence, "Assessing the Accuracy of a Novel Optical Technique for Bedside Monitoring of Cerebral Blood Flow", Presented as a poster at Lawson Health Research Day, University of Western Ontario, London, Canada, March 22 (2011).

Professional Associations:

COMP (Canadian Organization of Medical Physics)
2015 – 2016

AAPM (American Association of Physicists in Medicine)
2015 – 2016

ACR (American College of Radiology)
2015 – 2016

SPIE (Society of Photo-Optical Instrumentation Engineers)
2010 – 2016

OSA (Optical Society of America)
2010 – 2016